5-2018

Discovering Key Unknowns for Tungsten-Hydrogen-Helium Plasma Material Interactions Using Molecular Dynamics

Mary Alice Cusentino
University of Tennessee, mcusenti@vols.utk.edu

To the Graduate Council:

I am submitting herewith a dissertation written by Mary Alice Cusentino entitled "Discovering Key Unknowns for Tungsten-Hydrogen-Helium Plasma Material Interactions Using Molecular Dynamics." I have examined the final electronic copy of this dissertation for form and content and recommend that it be accepted in partial fulfillment of the requirements for the degree of Doctor of Philosophy, with a major in Energy Science and Engineering.

Brian D. Wirth, Major Professor

We have read this dissertation and recommend its acceptance:

David C. Donovan, William J. Weber, Steven J. Zinkle

Accepted for the Council:

Dixie L. Thompson

Vice Provost and Dean of the Graduate School

(Original signatures are on file with official student records.)

Discovering Key Unknowns for Tungsten-Hydrogen-Helium Plasma Material Interactions Using Molecular Dynamics

A Dissertation Presented for the

Doctor of Philosopy

Degree

The University of Tennessee, Knoxville

Mary Alice Cusentino

May 2018

Acknowledgements

I would first like to thank my advisor, Brian Wirth, for all his support, encouragement, and advice throughout my graduate career. Without your guidance I would not have made it to where I am today. I have very much enojoyed working with you these past four and a half years. I would also like to thank the rest of my doctoral committee, Dr. David Donovan, Dr. William Weber, and Dr. Steven Zinkle, for their additional advice and support in my research.

I would also like to thank the research members that helped me throughout my graduate career, including Karl Hammond and Marie Backman. I appreciate the time you took to answer all the questions I had and for the very useful discussions throughout my time at UT. I enjoyed working with all the rest of the Wirth research group members and it was a pleasure to get to know you all.

Lastly I would like to thank my family and friends for all their support and for making my stay at in Knoxville more enjoyable. I want to especially thank my parents, Mariola and Michael Cusentino, for always encouraging me to pursue a career in the sciences and supporting me in everything I do. I would not be the person I am today without your influence. And finally I would like to thank my dog, Spock, for always being there after a long day of work.

Abstract

Molecular dynamics simulations have been used to study plasma material interactions to better understand the performance of a tungsten divertor. A tendril-like geometry was modeled to study the diffusion of helium in nanotendrils and its relation to fuzz growth. The tendrils remain stable throughout the simulation and a modified helium release mechanism is found that allows the helium retention to reach a steady state within the tendril. The helium retention within the tendril inversely depends on the surface to volume ratio. There is limited diffusion deep into the tendril and extrapolating the flux calculated to experimentally relevant time scales indicates that helium diffusion is not sufficient to drive fuzz growth. Helium implantation near a grain boundary, but not directly on the grain boudary itself, was performed. Helium behavior within the implantation zone is consistent with previous simulations of helium in defect-free tungsten. Some helium diffuses to the grain boundary where it forms small helium clusters but virtually no helium atoms diffuse over the grain boundary. The sink strength of the grain boundary and helium bubbles are calculated and the values are comparable, indicating that the grain boundary sink strength only matters at the beginning of the simulation before the helium bubbles form. Simulations of hydrogen and helium were performed to assess the interaction between the two gas atom species in tungsten. Simulations of small subsurface mixed hydrogen-helium bubbles indicate that hydrogen diffuses to the helium bubble periphery region and becomes trapped there. A binding energy of 2 eV is calculated. Modeling of hydrogen implantation in helium pre-implanted tungsten were performed and the presence of helium modifies the depth distribution and blocks the deeper diffusion of hydrogen when compared with hydrogen implantation in pure tungsten. This could potentially have a significant impact on tritium retention and material performance.

Table of Contents

List of Tables

List of Figures

Chapter 1

Introduction

The demand for energy is continually growing as nations across the globe expand their economies and unindustrialized countries enter the modern era. With this growth comes a realization that the current forms of energy powering the grid, namely fossil fuels, are unsustainable in the long run due to the limitation in supply as well as detrimental effects to the environment. Many countries have especially become concerned about the effects of carbon dioxide produced from burning fossil fuels to global climate change. Earth's current concentration of CO_2 in the atmosphere is now over 400 ppm, the highest it's been in centuries[1]. The increasing presence of carbon in Earth's atmosphere will increase global temperatures which can lead to environmental changes such as rising sea levels and melting ice caps. This awareness has led to a demand for cleaner, alternative sources of energy production to help reduce the amount of carbon dioxide entering the atmosphere. Energy production from cleaner alternatives like wind and solar is increasing and will be a part of the energy solution. However, wind and solar are intermittent sources and are not currently stable enough to meet energy demand 24/7. A cleaner option to base load coal energy will be necessary and nuclear energy could be the solution to continous, sustainable energy.

Fission energy is currently the largest source of carbon free energy in the United States. It has the advantage of having a high capacity factor, high energy density, and low carbon footprint comparable to renewables. Even with the potential of fission reactors to provide carbon free energy, utilities in the US have been dissuaded from building additional reactors because of the high capital cost due to the necessity of heat removal systems from the large decay heat associated with the high energy density of nuclear fission reactors, regulations, the political issues that arise from proliferation, and the public's perception of their risks of nuclear energy and problems with storing nuclear waste. On the other hand, fusion energy has the potential to meet this demand in a clean, safe, and sustainable manner. Fusion energy requires the

use of deuterium and tritium as fuel which are virtually limitless since deuterium can be found in water and tritium can be bred using lithium in the fusion reactor itself. This also eliminates the proliferation problem since there is no fissionable material used as fuel. Helium is the only by-product making fusion energy carbon free and there is no high-level radioactive material produced, eliminating the need for storage. The risks associated with fission power, such as a core meltdown, are elimiated in a fusion reactor because there is no nuclear chain reaction, maiking fusion reactors inherently safer. These benefits are driving the research and development needed to build a commericial level power plant, which has yet to be realized.

Much progress has been made in working towards a plant design and understanding the complex physics occurring within the reactor yet there are many crucial questions that still need to be addressed. The Joint European Torus (JET) and the Tokamak Fusion Test Reactor (TFTR) are examples of experimental reactors that have been successful in advancing the field and have produced 16 MW and 10.7 MW of power respectively[2]. Currently, a large international effort is being made to build the largest experimental reactor to date, the International Thermonuclear Experimental Reactor (ITER). The goal of this experimental is to output 10 times the power needed to sustain the fusion reaction as well as bridging the gap between the previously smaller tokamaks to a fully operational fusion power plan. This reactor is still mainly an experimental one meant to address many of the still unanswered questions that occur when scaling up the reactor size. The vital informtion that will be obtained from ITER will guide the design of the next iteration, Demonstration Power Station (DEMO), which will be hooked up to the power grid to display power plant capability.

One of the key issues identified for ITER and other future fusion reactors are Plasma Surface Interactions (PSI) [2][3][4]. PSIs encompasses the area of research that studies how the plasma interacts with the wall material of the vacuum vessel. There is a natural buffer zone, called the sheath, between the very hot core plasma and the internal structure of the vacuum vessel. What occurs between these two extremes drives both the core plasma and structural material performance and therefore it is crucial to understand the coupled behavior between these two regions. Material components within a fusion reactor will be subject to a slew of detrimental effects due to particle transport through the sheath layer including high ion fluxes, high temperatures, and high heat fluxes. This can lead to material damage such as erosion and blistering, the release of impurities back to the core plasma, and thermal fatrigue related damage that can limit the performance of the core plasma and material components. Hydrogen recycling at the material surface is also important for core plasma performance and fueling. Therefore, it is important to understand the processes of how the particles are transported to the material surface and how the particles can cause damage to these components in order to predict the material

behavior over the lifetime of a reactor and design materials that can counteract these effects.

1.1 Plasma Facing Materials in Fusion Reactors

The study of plasma facing materials has a long history going back to the early experimental reactors that tested various methods and materials to reduce the load on material components. Currently, the tokamak design that burns deuterium and tritium as fuel has gained the most success and will be the basis of future fusion reactor designs. The tokamak design consists of a torus shaped device that uses magnetic field lines to contain the plasma. Of course, containment of the core plasma is not perfect and some particles will drift out of the core and towards the wall materials, generating impurities which lead to core plasma contamination. To protect the internal walls of the vacuum vessel, a component called the limter was initially created as a focal point for the escaping particles, in order to have just one component bear the brunt of the damage instead of spreading it across the entire wall of the vacuum vessel. A limiter is placed around the inside of the vacuum vessel with the edge being a few centimeters from the edge of the wall to ensure that the plasma will hit the edge of the limiter as opposed to the wall itself. The limiter is typically made of stainless steel [2]. While the limiter reduced the area subject to plasma surface interactions, there were still impurities entering the core plasma leading to the need for a different design.

The next iteration in design included a component called a divertor to reduce the level of impurities reaching the core. The idea was to move the point of contact to a location far away from the core plasma where the impurities could be contained[2] as well as mitigate the damage to the plasma facing components. Particles generated in the core region will drift towards the edge plasma, which controls the transport towards both the core and reactor components. Moving from the core towards the edge plasma, the magnetic field lines are closed until the last closed flux surface near the edges plasma is reached. On this outermost flux surface, there is a zero in the polodial magnetic field where the core and edge plasma meet known as the X point. In a divertor configuration, the magentic field lines beyond the last closed flux surface, also called the separatrix, are open and terminate at the divertor surface. This region is known as the scrape off layer (SOL). For the divertor configuration, the SOL can funnel any impurities from the wall back to the divertor surface [2]. A cross section of the reactor showing how the magnetic lines intersect the divertor region is shown in Fig. 1.1. The particle transport along these open field lines is the main source of material damage the divertor will be subject to, which includes both plasma ions and impurities. This concentrates the damage at the divertor surface which both prevents

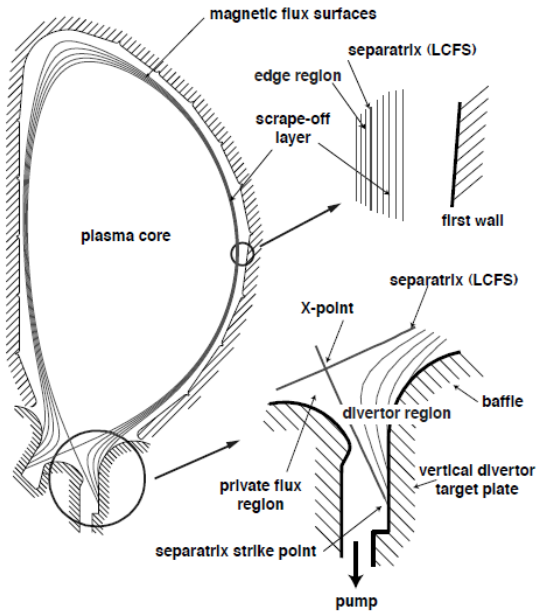

Figure 1.1: Cross section taken from [2] of a tokamak depicting the magnetic field lines and how the scrape off layer intersects the divertor region. The particle transport along these open field lines is the main source of material damage the divertor will be subject to.

damage from occuring all across the vessel wall and focuses the effort on designing protection for one component.

Various materials have been tested to be utilized in either a divertor or limiter. Early on, graphite was the material of choice because it is a low Z material that will reduce the effects of impurities in the core and does not melt under high heat loads but instead undergoes sublimation [2]. As experiments and modeling efforts continued to further investigate carbon as a limiter or divertor material, the realization that chemical interactions between carbon and hydrogen could prevent graphite from becoming a divertor material in later fusion reactors. High chemical erosion rates of roughly $0.1\frac{C}{D}$ as well as co-deposition with tritium leading to high levels of retention encouraged the exploration of other plasma facing materials. Another low Z material that has been investigated is beryllium. Beryllium has good thermoconductivity and is not reactive with hydrogen like carbon is. Jet has extensively studied beryllium components [5] after success was observed in smaller tokamaks. While plasma performance increased with beryllium, such as reducing the incidence of disruptions, beryllium can melt and sputter easily while also posing handling problems because of its toxicity.

As divertors became more prominant, low Z materials became less of an obvious choice because they are better suited to the high edge plasma temperature that is seen at the surface of a limiter[2]. Particle temperatures would be much lower in the divertor which is more suitable for high Z materials since it will typically be below the sputtering threshold. Therefore, alternate materials have been investigated for the divertor, such as molybdenum and tungsten. Experimental reactors that have used molybdenum, as in Alcator C-Mod[6], and tungsten, as in the ASDEX-Upgrade[7], have obsered very low erosion rates at the divertor surface. Both metals have good thermal properties and low sputtering yields making them appropriate choices for the being able to tolerate some of the conditions at the divertor surface.

Ultimately, tungsten has been chosen as the divertor material for ITER due to its high thermal conductivity, high melting temperature, and low sputtering yield [4]. Many complex physicals processes will occur at the plasma-material interface. Fig. 1.2 depicts a few of the interactions of concern to the fusion community, including sputtering, defect formation, gas atom clustering that can lead to bubble formation, etc. These events that happen on the atomic level will manifest into macroscopic radiation damage and in fact, experiments have shown tungsten surface deformation under both helium and hydrogen implantation. Tungsten exposure to helium from linear plasma devices have indicated that a layer of helium bubbles will form just below the surface [8] [9] [10]. At low temperatures, small pin holes on the surface are visible [8] while at temperatures above 2000 K larger micron sized holes are visible [11]. At intermediate temperatures, between roughly 1000 K and 2000 K, a layer of fuzz like nanostructures have been observed [8][12] [13][14]. Similarly, hydrogen irradiation also causes tungsten surface modification including micron sized blisters on the surface [15][16]. However, in the case of mixed helium-hydrogen plasma experiments, these blisters seem to be suppressed [17]. The exact physical processes that lead to fuzz growth or blistering (or lack thereof) are still currently unknown but the initial atomistic level damage is crucial to the eventually development of these structures and further experiments studying the radiation damage effects in tungsten are needed. [18].

1.2 Radiation Effects in Materials

The study of radiation damage in matter is a wide field that includes many different types of radiation effects and materials. One of the most interesting and studied radiation damage phenomena occurs within both fission and fusion nuclear power plants. Because these power plants need to operate for decades, atoms within the reactor components will be displaced many times over the reactor lifetime leading to macroscopic damage effects like radiation induced hardening, embrittlement, fuel swelling, etc. Current commericial light water reactors (LWRs) operate around 300

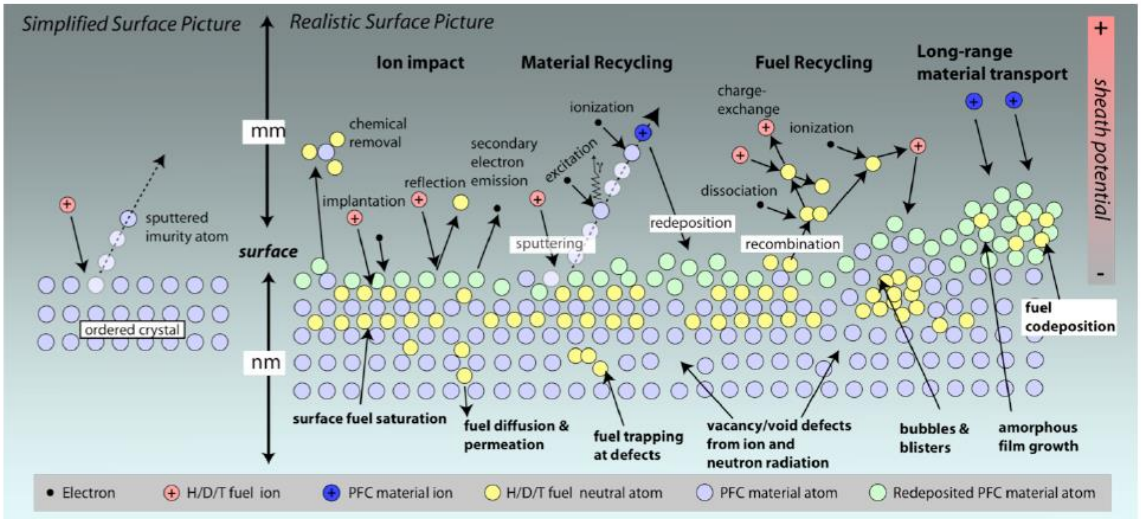

Figure 1.2: Illustration taken from [19] of the many complex processes that occur at the plasma-material interface due to large ion fluxes. This work focuses on some of the physical processes that are displayed here such as fuel retention and trapping as well as bubble formation.

°C and up to 50 displacements per atom (dpa) over the liftime of the reactor. A commercial fusion reactor, on the other hand, will need to operate at temperatures between 400 and 1000 °C and will be subject to radiation damage in the 50-200 dpa range. This introduces a whole new host of issues which need to be accounted for when designing materals for future fusion reactors. Some of the fundamental radiations damage mechanisms relevant to this MD study of plasma facing components in this work, namely radiation displacement events, diffusion, and clustering, will be discussed briefly here.

1.2.1 Radiation Displacement Events

The initial radiation-matter interaction that initiates the entire damage process is when an energetic particle collides with an atom in the reactor components. Depending on the type of particle, the nucleus or the electrons may be affected. Neutral particles, like neutrons, will interact with the nucleus of the atom through scattering events which depend on the scattering cross section, σ_s. Gamma particles interact with the electrons of an atom through the photoelectric effect, compton scattering, and pair-production depending on the energy of the photon. Charged particles interact with both the electrons and the nucleus, initially being slowed down through electronic stopping and then scattering off the nucleus once the energy is low enough. In the case of plasma-material interactions at the divertor surface, the initially incoming helium and hydrogen ions have been neutralized in the sheath

region before impacting at the divertor surface. Therefore, electronic stopping is not particularly important in this case because of this and the fact that the gas atom energies are typically less than 100 eV, which is below the electronic stopping threshold. In addition, MD does not explicitly model the atomic electrons but indirectly includes them through the interatomic potentials. Therefore, only nuclear collisions will be briefly discussed here.

Most reactors materials are arranged in a lattice structure and if the energetic particle imparts enough energy to one of the lattice atoms through a nuclear collision, it can knock the lattice atom off of it's site creating a vacancy and interstitial complex called a Frenkel pair. It is the creation of these defects that accumulate in the material and will later manifest as the various types of radiation damage and effects seen in nuclear materials. The initial atom that was displaced is denoted as the primary knock-on atom (PKA) and this atom can subsequently go on to displace other atoms from their lattice sites providing that the PKA can transfer enough energy to displace other atoms. One collision event can lead to a whole host of subsequent collisions and this event is known as a casacde. There is a threshold energy in order to knock a atom off its lattice site, denoted as the displacement energy E_{disp}, and is typically in the 10-50 eV range for most metals. In the case of tungsten, the average displacement energy is calculated by experiments is about 80 eV [20]. Atoms at the surface can be knocked off their lattice sites in a processes known as sputtering. The displacment of these surface atoms can lead to erosion at the plasma-material interface and transport of impurity atoms to the core plasma.

To create displacment damage, the incoming energetic particle needs to transfer enough energy to overcome the displacment threshold. The energy transfer for an elastic collision between an energetic particle and a stationary atom is:

$$E = \Lambda E_{disp}(1 - cos(\theta)) \quad where \quad \Lambda = \frac{4M_1M_2}{(M_1 + M_2)^2} \tag{1.1}$$

where M_1 and M_2 are the masses of the two particles and θ is the angle at which the particles collide. If the energy transferred to the lattice atom is enough to overcome the displacement threshold, the atom will be knocked off of its lattice site and can go on to knock additional atoms from their lattice sites. Eventually, this atom will come to rest within the lattice as an intersitial atom. A typical cascade event takes about 10^{11} seconds [21] which makes it ideal for modeling with MD. In addition to atom displacement in the bulk, atoms at the surface can also be displaced and leave the material completely in a process called sputerring. In order for an atom to be knocked off the surface, the surface binding energy of the atom must be overcome. This value is similar to the displacement energy, typically between 10-100 eV for most metals. In the case of sputtering, this can lead to damage on the material surface

such as erosion so it is important to know what the sputtering yield will be for the particular material being used.

In the case of plasma material interactions, the energy of the incoming helium and hydrogen atoms are typically too low ($< 100ev$) to create frenkel pairs. The sputtering yield is also quite low at these energies, only about $10^{-4} - 10^{-3}$ [22]. Instead, most of the gas atoms will either reflect off the surface or implant and diffuse within the tungsten until they become trapped or desorb from the surface and return back to the plasma. However, high energy neutrons will be present in the plasma and will be able to transfer enough energy to displace tungsten in the divertor region. This will create vacancies which can later become trap sites for both hydrogen and helium.

1.2.2 Diffusion

Interstitial atoms and vacancies, which are naturally present in a material, will migrate throughout a crystalline lattice, even in the absence of external forces, due to thermal vibrations. This will be especially true for the high temperatures expected in the divertor region. Diffusion of interstitials is the beginning stage for many of the types of material damage induced by radiation. Migrating interstials can eventually cluster and form bubbles which is exactly the case for helium and hydrogen in tungsten. In order to minimize the energy of the interstial within the lattice, they are located at sites of high symmetry denoted as octahderal or tetrahedral sites based on the structure made by the neighboring lattice atoms to the interstitial site. Single interstitial atoms typically diffuse through either of these interstitial sites within the lattice and can be driven by strain fields, temperature, etc. For tungsten, a bcc lattice, octahedral sites are located on the faces and on the sides of the unit cell while tetrahedral sites are located in the corners of each of the faces of the unit cell. This yields a total of 6 octahedral sites and 12 tetrahedral sites per unit cell and are the sites for which hydrogen and helium interstitials in tungsten will intially migrate through as long as the atoms have enough enegy to overcome the barrier between interstitial sites. In the case of helium, the migration energy is fairly small being only about 0.1 eV for most metals.

If there are a large quantity of defects in a localized area, a gradient will form and drive the atoms until such a gradient is no longer present. This type of diffusion can be described by two equations, first of which links the flux of defects to the concentration using the typical Fickian diffusive flux plus a drift flux term which has been previously shown to be crucial in defining helium diffusion in tungsten **??**:

$$\vec{J} = -D\nabla C + \vec{u}_{ds}^{n} C_n \quad where \quad \vec{u}_{ds}^{n} = \frac{D_n F_s^{(n)}}{k_b T}\vec{z} \tag{1.2}$$

where J is the flux of defects, D is the diffusion coefficient, C is the concentration, $\vec{u}$ is the drift velocity, $F_s^{(n)}$ is the elastic interaction force, k_b is the Boltzmann constant, and T is the temperature. Typical values of D are between $10^{-20}\frac{cm^2}{s}$ and $10^{-5}\frac{cm^2}{s}$ for most materials between 20 and 1500 °C **??**. Note the negative sign which indicates that the direction of diffusion is towards decreasing the concentration. The second equation that describes the diffusion of defects is Fick's law which links the gradient of the flux and the rate of change of the concentration:

$$\frac{\partial C}{\partial t} = -\nabla J = -\nabla D \nabla C \tag{1.3}$$

The average energy of an interstitial atom based on the temperature from the surrounding lattice is typically not enough to overcome the migration barrier. However, there is a probability that the atom will accumulate enough energy to make the jump to the next interstitial site. The probability of this jump is based on the Arrhenius equation:

$$D = D_0 exp(\frac{-Q_d}{k_b T}) \tag{1.4}$$

where D_0 is the diffusion coefficient, Q_d is the activation energy for diffusion, k_b is the Boltzmann constant, and T is the temperature. In the case of interstitials, Q_d is just the interstitial migration energy, E_m^i. The general diffusion coefficient is described by the Einstein formula:

$$D_0 = \frac{1}{6}\lambda^2 \Lambda \tag{1.5}$$

where λ is the jump distance and Λ is the number of jumps per second. For interstitials the Einstein formula becomes:

$$D_0^i = \alpha a^2 \omega \quad where \quad \alpha = \frac{1}{6} z A^2 \tag{1.6}$$

where a is the lattice constant, ω is the jump frequency, z is the number of neighbor sites, and A is a constant that is dependent on the diffusion mechanism and lattice type [21].

Helium is very mobile in tungsten, at least up until a critical cluster size, of about 4 helium atoms, when a small cluster is likely to trap mutate. The tetrahedral position is the lowest energy site for helium in the tungsten lattice and will typically migrate through the octahedral site to the adjacent tetrahedral site with an energy barrier of about 0.15 eV [23]. The diffusion coefficient of helium in tungsten was experimentally calculated to be $4.7x10^{-7} cm^2 s^{-1}$[21]. For hydrogen, which is also very mobile in tungsten, the tetrahedral site is also the preferable intersitial site and the pathway for diffusion is similar to that of helium but with a slightly higher migration energy of roughly 0.4 eV. The diffuusion coefficient is very similar to that of helium, being $4.1x10^{-7} m^2 s^{-1}$ for hydrogen [24]. Both helium and hydrogen will be trapped at

defects such as vacancies and grain boundaries and helium can also self-trap, which is a large driver for bubble growth in tungsten. The high mobility of these gas atoms will allow them to be trapped at these defect sites which is the beginning stages of bubble nucleation and growth.

1.2.3 Clustering and Bubble Formation

Experiments have shown that both helium and hydrogen will cluster and form bubbles in tungsten under plasma-like conditions. In the case of helium, small mobile cluster that trap mutate and further self-trap, can become a nucleation site for bubbles. As for hydrogen, defects like grain boundaries and other vacancy-like defects can trap hydrogen and allow for bubble nucleation. The formation of bubbles will depende on how mobile the gas atom speicies is, the minimum number of gas atoms that are needed to form a stable nucleus, and the rate at which vacancies can be created to sustain bubble nucleation and growth [21]. The occurance of bubbles from ion implantation in materials can alter the mechanical properties of said material, such as creating stress within the matrix.

Initially, there will be a nucleation stage where gas atoms will randomly diffuse and interact with other gas atoms to form small clusters. Once these atoms become stable, they can become a nucleation site for further bubble growth. Once a diffusing gas atom is more likely to interact with another stable nucleus instead of another diffusing gas atom, the nucleation stage transitions to a the bubble growth stage. A bubble will grow until the pressure inside reaches an equilibrium with the surface tension of the surrounding matrix. The pressure of an equilibrium bubble is described by the following equation:

$$P_{equilibrium} = \frac{2\gamma}{R} \tag{1.7}$$

where γ is the surface tension of the material and R is the radius of the bubble. Eventually the bubble will trap additional gas atoms and the pressure can become very high. In order for the bubble to continue growing, the pressure will need to be relieved. In the case of high gas pressure that can occur in plasma facing materials, one of the main ways that bubbles can reduce pressure is through dislocation loop punching, a process that transfers compressive energy stored in the bubble into strain energy in the form of a dislocation loop [25]. By pushing out a dislocation loop, the bubble will now have room to expand and can accommodate more gas atoms. The bubble will then continue to accumulate additional gas atoms until the pressure rises again to the point where loop punching will occur and the process begins again. The bubble pressure required for loop punching to occur is:

$$P_{loop} = \frac{2\gamma}{R} + \frac{\mu B}{R} \tag{1.8}$$

where γ is the surface tension of the material, R is the radius of the bubble, μ is the shear modulus of the material, and B is the magnitude of the burgers vector of the dislocation loop [25]. The high pressure bubbles that will occur in the tungsten matrix can lead to high stresses in the matrix and surface deformation and roughening can occur from dislocation loop punching. The process of loop punching in helium bubbles in tungsten has been observed in molecular dynamics studies [26][27][28].

1.3 Tungsten as a Plasma Facing Material

Plasma facing materials need to be able to withstand a variety of extreme conditions. High particle fluxes on the order of $10^{24} m^2 s^{-1}$ incident on the divertor surface can lead to surface damage and erosion while high thermal loads of about $10 \frac{MW}{m^2}$ will require active cooling [29] to protect material components. High energy disruptions may also occur which can lead to material ablation due to large amounts of deposited energy as well as material temperatures of up to 3000 K [12][30] [31]. On the other hand, neutrons from the plasma can modify the mechanical properties of material components and can lead to detrimental effects such as swelling. Any chosen plasma facing material will need to be able to handle this variety of conditions. Initially, low Z materials like carbon seemed like appropriate plasma facing materials due to lower radiation losses compared with high Z materials. However, long term lifetime of the materials was limited due to erosion and there was a concern of tritium retention, especially for carbon where high amounts of tritum co-deposited layers made it an unlikely choice for future plasm facing materials. Therefore, higher Z materials were again considered due to their higher resistance to sputtering and erosion as well as the higher magnetic field and higher density plasmas seen in more recent tokamak devices that lead to more favorable conditions for high Z materials [32].

So far, tungsten, a refractory metal, has been considered the leading candidate material for the divertor region due to its low sputtering yield (10^{-4}), high thermal conductivity ($150 \frac{W}{mK}$), and high melting temperature (3680 K) [4]. This will allow tungsten to better handle the high particle and heat loads that will occcur at the divertor surface. Tungsten also has a low hydrogen solubility which is important in regards to tritium retention [33]. In addition, the high rates of tritium co-deposition seen in carbon are reduced by a factor of 10^4 in tungsten due to overall lower sputtering yields and lower rates of tritium retention in co-deposited tungsten [32]. Various fusion devices have experience with tungsten operation, such as the full tungsten wall of ASDEX [34], as well as with other high Z materials like molybdenum at AlcatorC-mod [35].

One of the downsides to tungsten is that since it is a high Z material, tungsten impurities in the plasma can lower the overall plasma efficiency more so than

lower Z materials like carbon or beryllium. Tungsten contamination will mainly be determined by transport in the device which can be modified by careful control of the plasma near the divertor surface and reduction of high energy events like Edge Localized Modes (ELMs) [32]. Although the hydrogen solubility is low, defects initially in the material as well as defects produced through neutron damage can trap hydrogen leading to higher levels of retention. Tungsten is also a very brittle material at temperatures lower than about 600 K which might occur if active cooling is used [32]. The brittleness of tungsten can lead to cracking at high thermal loads. At higher temperatures creep starts to take effect as well as recrystallization which can reduce the hardness and strength of tungsten. Therefore, tungsten divertor components must be maintained between about 600 K and 1000 K which limits operating parameters [32]. Although the melting temperature is high, there is still a chance of surface melting if an ELM or other high energy event were to occur at the divertor leading to surface erosion and core plasma contamination.

In addition to these effects in tungsten, it is important to understand how the radiation damage from both helium and hydrogen will affect the performance of tungsten from a material performance standpoint. Experiments have shown surface modification from both hydrogen and helium irradiation under plasma-like conditions that will negatively impact tungsten as a plasma facing material. Here we will discuss both the experimental and modeling efforts that have been performed thus far to understand the material degradation that will occur in the divertor region.

1.4 Helium Behavior in Tungsten

Helium will compromise roughly 10% of the incoming ion fluxes. When the helium eventually reaches the divertor region, it will be of low enough energy, in the 100 eV range, that the sputtering yield of tungsten will be quite small. Although helium will not be able to produce displacement damage and Frenkel defects from impact energy alone, the ability of helium to self-cluster and form bubbles will produce enough material damage on its own to be of concern. There have been many experiments investigating the effects of helium on tungsten using both linear plasma devices as well as tokamaks and various forms of material deformation have been observed including bubbles, surface roughness, and a fuzz like layer that is unique to plasma conditions.

Helium is a noble gas and because of its filled closed electronic shell, it does not tend to interact with other atomic species but is instead chemically inert. In tungsten, helium will not dissolve within the material but will self-cluster. It is not that helium is particularly attracted to other helium atoms but that the helium-tungsten interaction is even more repulsive than the helium-helium interaction. Because of this self-clustering effect, helium does not migrate very far from its implantation depth

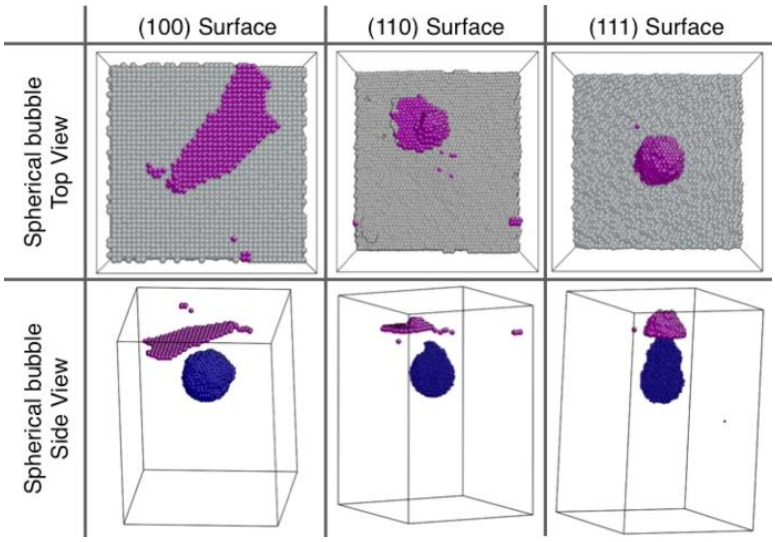

Figure 1.3: Atomistic snapshots depicting adatom island formations due to dislocation loop punching from over-pressurized subsurface helium bubbles from [28]. Different surface orientations will give rise to different adatom formations on the surface. The gray, magenta, and blue atoms represent tungsten atoms, surface adatoms, and helium atoms respectively.

but will self-trap near the surface and prevent incoming helium from diffusing deeper into the bulk. A majority of the helium will be implanted within a nm or two of the surface[36] and a large portion of the helium will remain within 10 nm of the surface [37] after implantation, which is indicates that helium remains in a very near-surface regime. These small helium clusters ($4 \leq n \leq 7$) are initially mobile but once they reach a critical size, can displace a tungsten atom to create an interstitial-vacancy pair [38]. The helium cluster will then sit on the vacancy site and will be effectively trapped. The now helium-vacancy complex will continue to trap additional helium atoms and become a site for bubble nucleation. This process is called trap mutation and is the main method of helium retention and bubble growth in the near surface region of tungsten.

Many of these small helium clusters will continue to grow. As these bubbles grow, they will evetually become overpressurized where they then must relieve this pressure before the bubble can grow further. In the case of helium in tungsten, bubbles will reduce their pressure through dislocation loop punching as discussed in section 1.2.3. The tungsten atoms that form the dislocation loop will reach the surface where they become adatom islands, which can be seen in the MD snapshots in Fig. 1.3. The formation of the adatoms greatly depends on the surface orientation as observed in various MD studies [28]. For example, the adatoms on the (110) surface tend to be shaped like platelets at an angle from the helium while the adatoms on the (111) surface tend to be shaped like a cap or dome directly over the helium bubble. In a

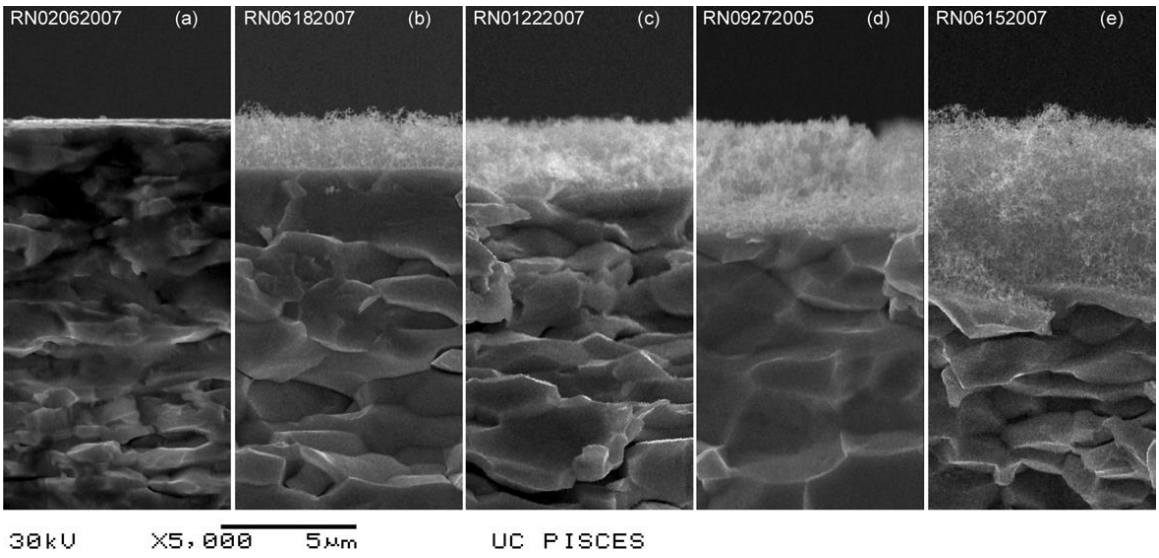

Figure 1.4: SEM images of helium fuzz growth on a tungsten surface at exposure times of (a) 300 seconds, (b) $2.0x10^3$ seconds, (c) $4.3x10^3$ seconds, (d) $9.0x10^3$ seconds, and (e) $2.2x10^4$ seconds at a temperature of 1120 K and a flux of $(4-6)x10^22m^{-2}s^{-1}$ taken from [11].

bcc metal like tungsten, the dislocation loops will prefer to glide along the $< 111 >$ direction. In the case of the (111) surface, this is directly from the top of the bubble to the surface while for the (110) surface, this is at angle from helium bubble and hence the difference in adatom formations on the surface.

As the helium fluence reaches higher values, an even more curious surface phenomenon has been observed. At low temperatures less than 1000 K, small pits form on the surface [8] while at 2000 K similar micron sized holes are observed on the surface [11]. The size of the holes tend to increase with increasing temperature and the helium energy needs to be higher than a threshold of 5 eV, consistent with the surface energy barrier of tungsten [10]. However at moderate temperatures between roughly 1000 K and 2000 K and ion energies greater than 20 eV [9], a fuzz-like layer has been observed in both linear plasma devices [8][12] [13] and tokamak experiments [14]. Fig. 1.4 depicts SEM images of fuzz growth on a tungsten sample after He irradiation. Initially, nanometer sized bubbles and small pinholes are observed near the surface at these temperatures and as the fluence increases, rod-like structures form and become finer at longer irradiation times as seen in the SEM images [9]. The fuzz layer can grow to a few m in thickness into the material but individual tendrils are only about 10-50 nm in diameter [12].

In Kajita and co-workers TEM analysis [39] helium bubbles were observed within the tendrils, displayed in Fig. 1.5, and it is believed that helium bubbles are involved in the nano-tendril formation process [40]. The tendrils do not grow above the original

surface but instead grow downwards into the material with a $t^{1/2}$ dependence observed by Baldwin and Doerner at a flux of $5x10^{22}m^{-2}s^{-1}$ [12]. The $t^{1/2}$ dependence has shown to be consistent with experimental work over fluxes from $10^{19}-10^{23}m^{-2}s^{-1}$ [41]; however an additional dependence on flux was observed, particularly at lower fluxes where there seems to be an incubation fluence needed before the fuzz will start to form [42] [43]. Since the tendrils are believed to form because of the sub-surface helium bubbles that appear, it will take longer to reach fluences where bubbles grow at lower fluxes and hence the incubation fluence needed before tendril formation [43]. In fact, it seems that the fuzz growth is dependent more on fluence than flux, needing a fluence of about $10^{24}m^{-2}$ to form but observed at fluxes varying from $10^{19} - 10^{23}m^{-2}s^{-1}$ [41]. Experiments have also shown dependencies on initial tungsten microstructure on surface deformation; for example, grains with different crystallographic orientations can lead to different surface formations [44]. However, the appearance of fuzz itself does not seem to depend on surface orientation.

Modeling has been a useful tool in attempting to understand some of the underlying physical mechanisms that may eventually lead to the fuzz formation observed in experiments. For example, helium bubbles seem to play a large role in the formation of fuzz and a lot of modeling work [26][27][45] has been done to understand how bubbles from and behave in the tungsten matrix. These studies have been able to quantify the pressure of helium bubbles and the resulting strain field in the matrix, to understand the dependence of surface deformation on surface orientation due to subsurface helium bubbles, and to observe the evolution of bubbles from growth and loop punching to bubble bursting. In addition, Ito et al. [26] and Sefta [27] have both quantified helium bubble bursting in terms of the He/V ratio and the bubble pressure respectively. Other studies have investigated the depth distribution for implanted helium and confirmed that helium does implant a few nanometers below the surface at low energy [36] and depends on crystallographic orientation [37]. MD has also provided information on the helium retention in tungsten as a function of both implantation flux and surface orientation [37]. There has been DFT [46] and MD [23][47] work that has investigated both helium atom and small helium cluster migration. These detailed studies into energy barriers and helium diffusion dependencies can help to understand the helium migration behavior in tungsten based on various initial conditions.

The presence of fuzzy structures is a large concern within the fusion community because it can degrade the material properties and performance of the tungsten divertor. Studies have shown that the nanostructures can negatively affect thermal conductivity and optical reflectivity [39]. In addition, the nanostructures can lead to increased amounts of erosion and dust formation [48] which, if it enters the core plasma, can greatly decrease the efficiency of the fusion reaction [49]. A lot of experimental work has been done to understand the fuzz growth process but no coherent theory that can completely describe how fuzz forms has been discovered.

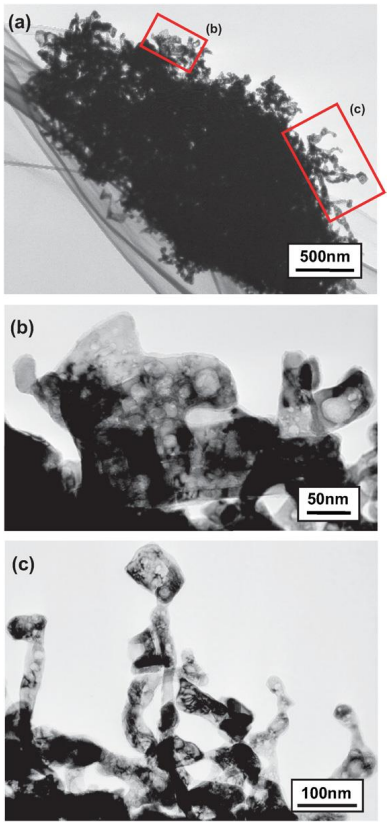

Figure 1.5: TEM images of fuzz growth on tungsten showing the (a) fine structure of the fuzz and (b-c) 10 nm bubbles that are identified within the 20-30 nm wide tendrils taken from [39]. The ion fluence for this ample was $4x10^{27}m^{-2}$ and the temperature was 1600 K.

However, there are a couple of hypotheses within the community. Kajita et al. theorized that the initial pinhole formations observed on the surface from subsurface helium bubbles eventually cause enough surface roughening and bubble coalescence to form tendrils [9]. Kransheninnikov described a viscoelastic model of fuzz growth where subsurface helium bubbles can create a skin of tungsten above the bubble that will experience a higher force than at the base of the bubble which will lead tungsten atoms to flow to the top of the nanostructure and therefore causing upward growth of the structure [50]. Another model by Martynenko and Nagel states that adatom formation from helium ion bombardment cause tendril growth because the adatoms will diffuse on the surface and can be trapped at steps and protrusions from open gas bubble sites as well as the thin shells from subsurface bubbles [51]. These sites can then be sources of adatom nucleation which can lead to fuzz growth. There have even been modeling efforts, such as Lasas OKMC work that modeled fuzz formation based on helium bubble growth and loop punching that eventually leads to surface roughening and fuzz growth [40].

1.5 Hydrogen Behavior in Tungsten

Hydrogen will make up about 90% of the incoming ions in the divertor region and presents a set of materials issues for the tungsten divertor. Hydrogen retention and recycling are two of the largest concerns [2]. Since deuterium and tritium will be the hydrogen isotopes used as fuel for the fusion reaction and tritium is a radioactive isotope, it is important to determine exactly how much tritium will be retained in the divertor. Tritium is considered a radiological hazard and the inventory limit for tritium is roughly 20 kg [52]. On the other hand, the amount of hydrogen recycling occurring in the plasma-material interface is also important to understand. Hydrogen recycling effects fueling efficiency, plasma density control, and the number density of neutral hydrogen near the material surface which then can affect global particle and energy confinement [2]. Therefore it is crucial to understand the effects of hydrogen in tungsten because it will affect not just the material performance but overall plasma performance as well.

The incoming hydrogen atoms will initially either reflect off the surface or implant within a few nanometers of the surface at the low energies seen in fusion plasmas. Hydrogen in the implantation zone can be trapped by defects such as vacancies, grain boundaries, and impurities [16]. The graphic in 1.6 shows the different physical processes that can occur when hydrogen ions impact the divertor surface. However, unlike helium, hydrogen does not self-cluster [53] but is in fact repulsive at short distances [54] [55]. Hydrogen is a very mobile species in tungsten and can migrate much further into the bulk compared to helium and therefore hydrogen bubbles form deeper within the material [53]. Hydrogen atoms that do diffuse back towards

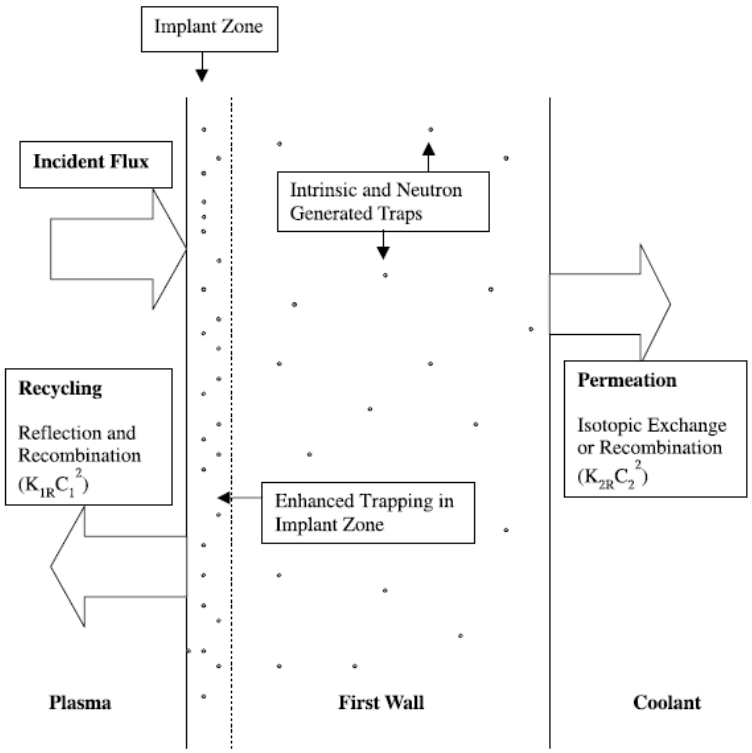

Figure 1.6: Schematic describing the physical processes that can ocur when an incident hydrogen flux hits a tungsten surface taken from [16].

the surface must first recombine to form H_2 then desorb as a molecule. Therefore, hydrogen desorption, unlike helium desorption, will be limited by the recombination rate [56].

Experiments have shown various forms of material damage due to hydrogen irradiation including bubbles and blisters and some examples are shown in Fig. 1.7. Although the expected hydrogen energy in the divertor region will be much less than the sputtering threshold, experiments have shown that blisters will still form on the surface under low-energy (10-500 eV) high flux ($10^{20} - 10^{22} m^{-2} s^{-1}$) hydrogen irradiation [15] [57] [58]. Blisters have been observed to be anywhere from 1-2 microns [59] in size all the way up to 100s of microns in size [57][60] and this seems to depend on the microstructure, such as the initial size of the grain boundaries [61]. Such blisters could increase hydrogen retention and become sites of large hydrogen inventory and release, if the blisters were to exfoliate.

Modeling has again helped to understand some of the physical processes that are observed in experiments. A lot of DFT work has been done investigating the behavior of hydrogen in tungsten and has brought to light some interesting conclusions that will be discussed here. Hydrogen that remains in the bulk will preferentially

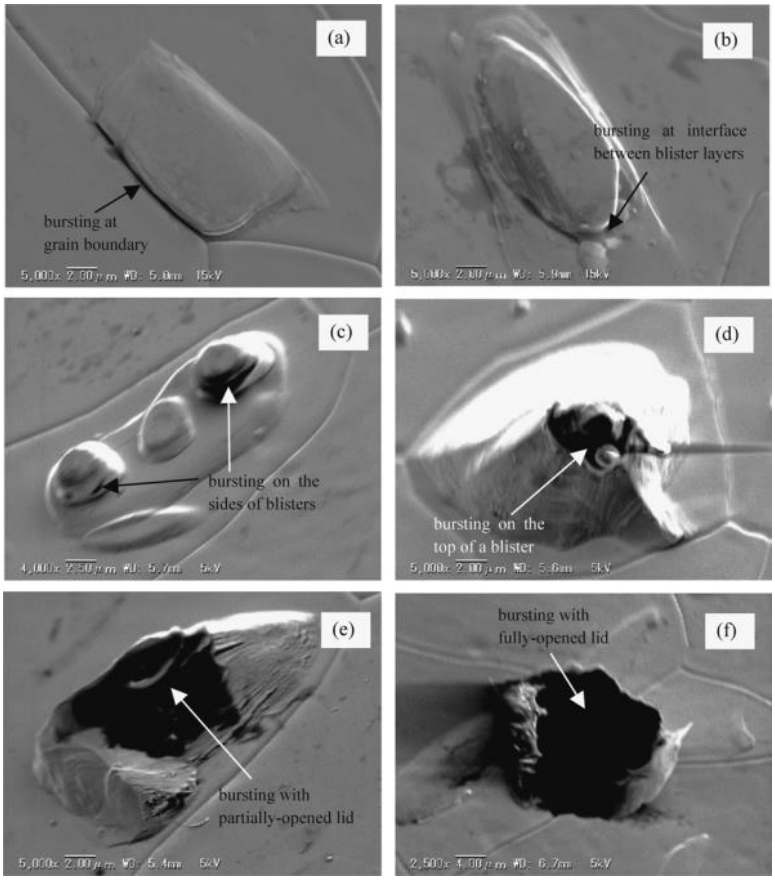

Figure 1.7: SEM images of blister bursting on a tungsten surface from hydrogen irradiation after a fluence of $10^{26} m^{-2}$ at 520 K [59].

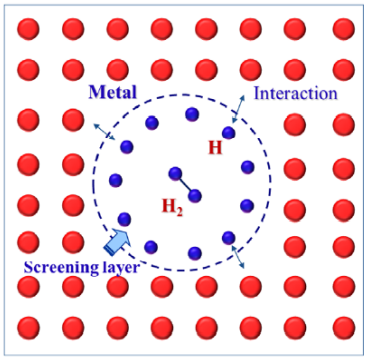

Figure 1.8: Graphic depicting a hydrogen bubble formation mechanism [64]. The hydrogen initially populates the tungsten-void interface due to the low electronic potential there. Eventually, this low potential shell is screened out and subsequent hydrogen atoms now enter the void as H_2. Voids can therefore become bubble nucleation sites which may lead to blistering as the bubbles grow in size.

sit at tetrahedral interstitial sites [54] [55] [62][63] and will typically diffuse from tetrahedral site to tetrahedral site with an energy barrier of about 0.2 eV [54]. However, hydrogen has a strong binding energy to vacancies and will be trapped at such sites if encountered in the bulk. The trapping site for hydrogen at a vacancy is offset from the vacancy but close to the octahedral site on an isosurface of charge that surrounds the vacancy [54]. The low electron density near the vacancy makes it an ideal trapping site for hydrogen. As additional hydrogen are trapped a single vacancy, the binding energy decreases due to the repulsive nature of the hydrogen-hydrogen interaction [54] [55] [63] [65]. A vacancy site can trap at least 6 [55] [63] and up to 14 [65] hydrogen which will saturate the isosurface surrounding the vacancy and effectively screen the isosurface, causing hydrogen to then reside in the vacancy itself as H_2 molecules [66]. This processes is illustrated in Fig. 1.8. and can then describe a scenario where hydrogen bubble nucleation is possible [66]. In addition, other defects such as grain boundaries and dislocations have similar vacancy-like surfaces that can trap hydrogen and nucleate bubbles in the same way as vacancies. This is supported by experiments which show preferential hydrogen bubble sites at vacancies [59], grain boundaries [16], and dislocations [67]. However, much of the computational work on hydrogen has been performed at the DFT scale and larger simulations will be needed to understand the observations at experimental scales.

1.6 Hydrogen-Helium Interactions in Tungsten

While much work has been done to understand the individual effects of both helium and hydrogen implantation in tungsten, the plasma will ultimately be a mixture of

approximately 90% hydrogen and 10% helium plasma and therefore it is important to understand how the presence of helium will affect hydrogen behavior and vice-versa. In many experiments, it has been shown that even very small amounts of helium in the plasma will affect the retention and surface deformation of tungsten due to hydrogen.

In addition to studying the individual effects of helium and hydrogen implantation in tungsten, the effects of combined hydrogen-helium plasmas have also been investigated. Experiments have been performed where a tungsten sample was pre-irradiated with helium and then subsequently irradiated with deuterium to assess the effects of a pre-damaged microstructure on deuterium implantation [31][68] . In the work by Iwakiri et al. [68], thermal desorption spectrometry (TDS) was performed and it was found that the pre-irradiated helium samples had a higher temperature deuterium desorption peak and a higher deuterium retention, although these experiments were performed with ion energies in the keV range. Nishijima et al. [31] performed similar experiments but with ions less than 100 eV and saw similar TDS spectra but only saw increased retention at higher temperatures. In addition, simultaneous helium-hydrogen experiments have been performed [69]. It was observed that the TDS spectra for helium [69] did not change significantly in the presence of deuterium but the deuterium TDS spectra did change in the presence of helium, as seen in the two previously mentioned experiments. Elastic recoil detection (ERD) was also performed [69] and the helium depth did not change significantly but the deuterium did not diffuse as far into the material in the presence of helium, which means that the helium may be somehow trapping the deuterium and preventing it from migrating further into the material.

Further experiments have been performed to assess the surface morphology changes due to mixed ion irradiation. Ueda et al. [17] performed simultaneous hydrogen-helium irradiation and subsequent TEM analysis, shown in Fig. 1.9. In the case where there was no helium present in the plasma, blisters formed on the tungsten surface which is consistent with previous results of pure deuterium experiments. However, with concentrations as low as 0.1% helium present in the plasma, blisters were almost completely suppressed for temperatures at 473 K, 653 K, and 723 K and the deuterium retention was lower [17]. Experiments performed by Miyamoto et al. [70] also showed blister suppression and lowered retention in mixed hydrogen-helium plasmas. It was speculated that the helium bubbles, which form just tens of nanometers below the surface, can effectively trap the deuterium atoms from diffusing further in the bulk [17]. Unlike helium, hydrogen will diffuse deeper into the material and can be trapped at defects like grain boundaries which will eventually lead to the blistering observed in experiments. If helium can prevent hydrogen from diffusing to these defects, the hydrogen will be unable to nucleate into bubbles that form the blisters seen on the surface and will instead diffuse out of the material. Fig. 1.10 depicts this hypothesis, showing the proposed difference in the hydrogen diffusion

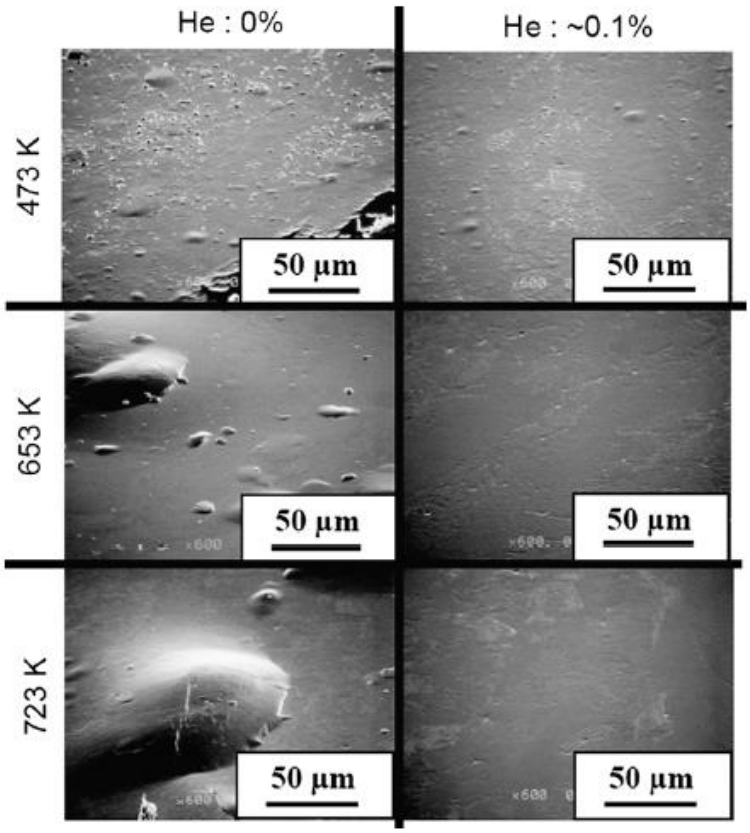

Figure 1.9: Images of the tungsten surface morphology deuterium irradiation as modified by temperature and helium ontent from [17]. Hydrogen blisters are almost completely suppressed with helium present in the plasma at concentrations as low as 0.1% and especially at higher temperatures.

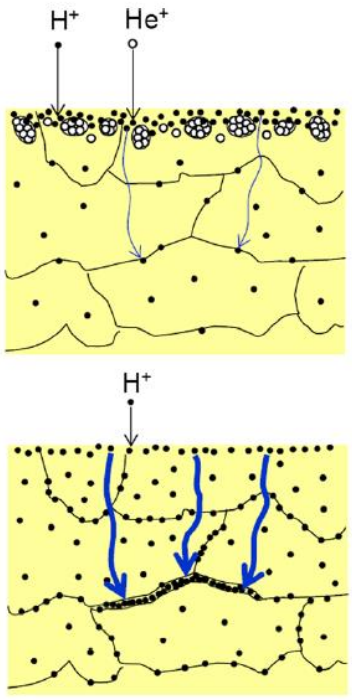

Figure 1.10: Schematic depicting the hypothesis that the presence of helium bubbles (top image) can block the diffusion of hydrogen deeper into the bulk (bottom image) where it can accumulate at grain boundaries to eventually form blisters [17].

depth with and without the subsurface helium bubble layer. The nuclear reaction analysis from Miyamoto's (NRA) analysis confirms that the hydrogen remains near the surface in the mixed plasma cases while it diffuses much deeper into the bulk (up to $3\mu m$) in the pure deuterium case [70]. This was further investigated by Ogorodnikova et al. using NRA and found that in the case of the helium seeded plasma, the deuterium remained mostly within $0.1\mu m$ of the surface while in the pure deuterium case, there was much less deuterium near the surface and the profile was more even and reached up to microns in depth [18]. However, this difference is most striking at lower fluences; once the fluence reaches $10^{25}\frac{D}{m^2}$ the deuterium will start to diffuse deeper into the bulk. This suggests that the helium bubbles might initially trap deuterium but will eventually saturate and hydrogen will again begin to diffuse deeper into the material.

Modeling work has again begun to further our understanding in what is observed in the experimental work. DFT has been used to investigate the synergistic effects of hydrogen and helium in tungsten in the hope of attempting to explain the suppression of hydrogen blistering under mixed plasma exposure. Simulations performed by Zhou et al. showed that when helium is place at an interstitial or vacancy site, it changes the volume of the lattice and therefore the charge density as well[62]. Since hydrogen

prefers to sit at the lowest possible isosurface of charge, the presence of helium affects the binding energy of hydrogen at these sites. In fact, the optimal charge density is lower than hydrogen at the TIS, about $0.11\frac{electrons}{\{AA}^{-3}$ for the case where helium occupies the vacancy site, which means that the binding energy is stronger for hydrogen at the helium-vacancy complex than at the TIS [62] and can therefore act as an additional trapping site for hydrogen. In fact, a helium occupying a vacancy can trap up to 12 hydrogen atoms with a lower energy than if the hydrogen were at a TIS [62]. This can provide a driving force for hydrogen segregation at helium-vacancy sites. In addition, helium has a higher binding energy to a vacancy, 4.59 eV as opposed to 1.18 eV for hydrogen, and the diffusion barrier for a helium atom to reach a vacancy is also lower, 0.06 eV compared to 0.14 eV for hydrogen [62]. Thus it is more likely that helium will occupy any given vacancy. If helium will preferentially occupy the vacancy site, it can then block the hydrogen bubble formation process described earlier. In addition, if the helium-vacancy complex strongly attract the hydrogen, this will also prevent hydrogen from diffusing deeper into the material. Both of these mechanisms combined can begin to explain the suppression of hydrogen blisters seen in experiments.

Further modeling using MD has also been performed to investigate the hydrogen-helium interaction in tungsten. Juslin et al. [71] used MD to study the segregation of hydrogen to helium bubbles. It was found that when hydrogen and helium were randomly distributed in a void in bulk tungsten, after 100 ps most of the hydrogen did not remain in the void but migrated to the periphery of the bubble. This occurred for temperatures between 300 K and 2100 K and concentration of 1 He/V to 2.5 He/V and 0.1 H/V to 0.5 H/V [71]. These results indicate that helium bubbles can be a sink for hydrogen and retain a large number of hydrogen atoms. We have also conducted our own work, similar to Juslins, of mixed hydrogen-helium bubbles but with the presence of a free surface. The same conclusion, that hydrogen segregates to the bubble periphery, was observed. Even when the hydrogen was placed not just in the bubble but throughout the tungsten matrix, and allowed to diffuse for 10 ns, a large portion of hydrogen, roughly 35%, still segregated to the helium bubble. This could have negative implications for tritium retention since there will be a large population of sub-surface helium bubbles in the tungsten divertor. Additional MD simulations were performed by Grigorev et al. [72] that studied the mobility of small hydrogen-helium clusters. They found that the migration barrier of hydrogen-helium cluster is higher than that of an interstitial helium atom or pure helium clusters of similar size by almost a factor of two [72]. Therefore, as helium clusters gain hydrogen atoms, there diffusivity is lowered significantly. Both of these MD studies have indicated that there is some interaction between hydrogen and helium in the tungsten matrix that needs to be studied further.

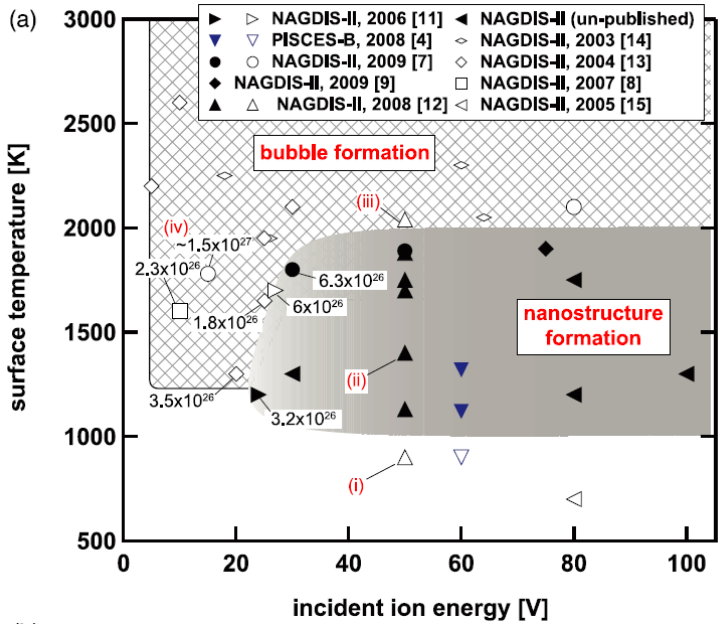

Figure 1.11: Plot of ion energy vs. surface temperature for various experiments performed at NAGDIS-II and PISCES-B [9]. The shaded region highlights the temperature and ion energies where tendrils have been observed while the hatched area depicts experiments where only bubbles have been seen. Fuzz seems to depend on both energy and temperature in that it has only been observed between 1000 K and 2000 K and at energies between 20 eV and 100 eV.

1.7 Outstanding Questions Addressed in this Dissertation and Motivation

Many experiments and subsequent modeling efforts have been made in attempt to understand the material damage a tungsten divertor would be subject to in a fusion reactor. The helium fuzz growth is a major concern and the growth of this surface structure seems to depend on many different variables, such as temperature, fluence, ion energy, etc. Fig. 1.11 displays just some of the parameters that tendril growth seem to depend on, indicating just how complex of a problem it is. Also of concern is the hydrogen retention, which seems to accumulate in the tungsten matrix and form blisters but also depends on the presence of helium in the matrix. Many of the mechanisms that lead to such experimental observations have yet to be defined, such as how exactly the nano-tendrils form, but MD can play a key role in understanding these observations, as seen in the modeling efforts that have investigate things like bubble rupturing [26][27] and surface deformation from helium irradiation to studying mobility of hydrogen-helium complexes and tabulating their migration energies [72].

However, there are still gaps between the experimental and modeling work, namely that some of the modeling paradigms do not match the experimental ones and therefore it is difficult to directly compare the results obtained. This is especially true for the length and time of MD simulations as well as the initial microstructure. Many of the MD simulations that have been performed are limited due to computational cost and therefore the size of the simulation and the amount of simulated time that can be reached is restricted. Most MD simulations are performed for about a few thousand to a few hundred thousand atoms and for simulation times on the order of nanoseconds to microseconds. This leads to ion fluxes of about $10^{27} m^{-2} s^{-1}$, a few orders of magnitude higher than used in experiments or expected in ITER. Although these small simulations can be useful in understand mechanisms that happen on short time and length scales, it is important to think about how the high ion fluxes, small simulation size, and short length of time can affect the results and make it difficult to directly compare with experiments.

Some work has been done that investigate the effects of these simulation parameters on the results obtained. Sandoval et al. [73] investigated the effects of varying the growth rate on helium bubble nucleation in tungsten using both MD and parallel replica dynamics. Plots of the dependence of growth rate on different parameters is shown in 1.12. They simulated growth rates over 6 orders of magnitude ($10^{12} 10^{6} \frac{He}{s}$) and found that two regimes formed based on the growth rate. For slow growth rates, helium bubble expansion is biased towards the surface and occurs at lower bubble pressures. At higher growth rates, the bubble expands isotropically and at higher bubble pressures. These regimes have been linked to the diffusion of tungsten interstitials around the bubble; in the slow growth regime, the tungsten interstitials have time to diffuse around the bubble and orient themselves in the [111] directions toward the surface while at the higher growth rates the interstitials form faster than they can diffuse and therefore dont have time to diffuse around the bubble surface [73]. These results indicate that ion implantation parameters, and therefore flux, can influence the MD simulation results by changing the final spatial distribution and number density of the helium [27]. In addition, the initial microstructure can influence the results, since MD simulations are typically single crystal and have no initial defects (like voids) while real materials will have grain boundaries and other such defects. For instance, the inclusion of a grain boundary can affect the retention and cluster size distribution of helium [74]. This can make it difficult to directly compare MD simulations to experiments. Lastly, small simulation cells with periodic boundaries can self-interact if the simulation cell is not large enough. If defects such as bubbles or dislocations are modeled and the simulation cell is too small, the defect can interact with itself through the periodic boundaries.

In this work, we attempt to ascertain some of the key questions in regards to helium and hydrogen radiation damage in tungsten under fusion relevant conditions

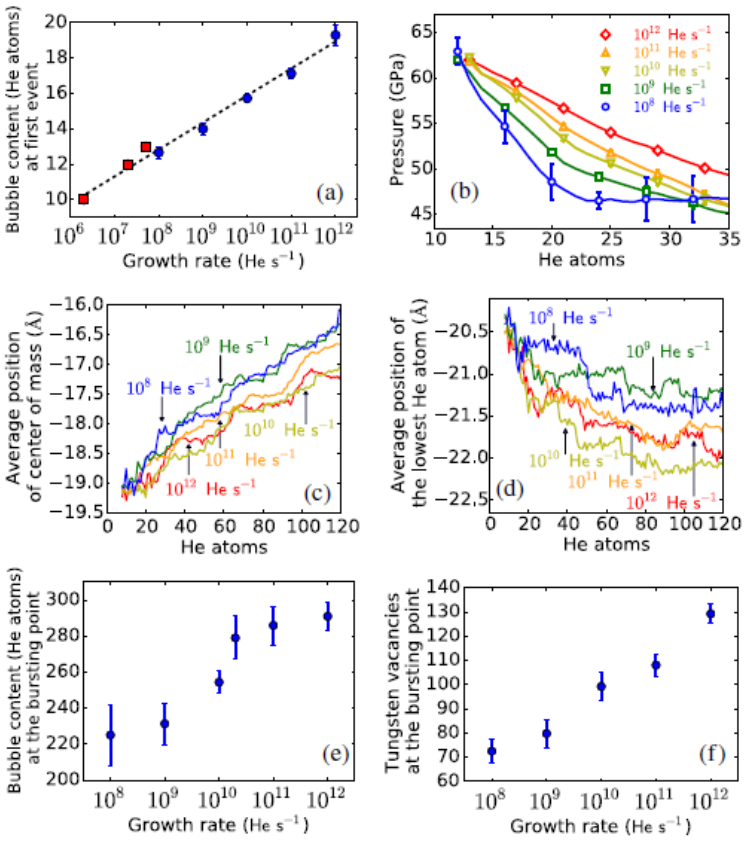

Figure 1.12: Plots showing the effects that the bubble growth rate has on various parameters including the (a) number of helium atoms at the first event, (b) pressure, (c) position of the center of mass, (d) position of the lowest helium atom, (e) number of helium atoms in the bubble when it bursts, and (f) number of vacancies when the bubble bursts [73].

using MD simulations with parameters and initial conditions that are more experimentally relevant. We also propose to perform more realistic simulations which can then be used to benchmark a continuum code that can model the physics to experimentally relevant conditions. The questions we hope to answer in this work are (1) how helium migrates to the bottom of the tendril to allow further tendril growth, (2) how three dimensional properties, such as grain boundaries and defects, effect subsurface response, and (3) what is the interaction between hydrogen and helium in tungsten. These simulation will attempt to bring the modeling closer to reality by including defects like bubbles and grain boundaries in the initial state of the simulation and expanding the box size to run large-scale MD simulations in order to bring down the flux to values more consistent with experiments.

The first part of this work foucses on the question of helium implantation and diffusion in defects inlcuding tendril-like geometry and grain boundaries. Helium will only implant within a few nanometers of the surface with the low ion energies seen at the divertor yet nanotendrils grow up to microns in depth into the material. It is still unkown how helium reaches the bottom of these tendrils in order to grow more fuzz when the implantation depth is so shallow. In this work, MD simulations will be performed for helium implantaion in tendril-like geometry. The time to grow tendrils from a clean tungsten surface is well outside the timescales attainable by MD so instead, an initial geometry that resembles a tendril is used. Helium will be implanted on a small version of a geometry resembling a tendril, which is about 8 nm high and 5 nm in diameter atop a 9 nm square block of tungsten, for varying temperatures, geometries, and initial helium bubble configurations. Bubble formation, tendril stability, and helium diffusion will be studied. Additional simulations will be done to further study the diffusion of helium in a much longer nanotendril by modeling a tungsten block of about 25 nm x 25 nm x 100 nm. Helium will be implanted from both sides of the tendril, with one end of the tendril having an intial distribution of helium bubbles. The helium diffusion will then be assesed with and withoug the presence of helium bubbles. To study helium diffusion around more intrinsic defects, a simulation involving a $\Sigma 3(111) < 121 >$ grain boundary will be performed. Helium will be implanted in a region not including the grain boundary itself to study the 2D diffusion of helium near defects to help benchmark the continum code, Xolotl.

Subsequently, the synergestic effects of hydrogen and helium observed in experiments, namely the lack of blister formation seen in mixed plasmas and the hypothesis that helium bubbles will modify hydrogen diffusion, will be modeled. This will involve modeling of small sub-surface mixed hydrogen-helium bubbles will be done in order to study the retention and diffusion of hydrogen near helium bubbles at a smaller scale. Then, a slightly larger simulation of a 90% Hydrogen/10% Helium plasma will be modeled and compared with pure hydrogen and helium simulations. Lastly, large-scale simulations will be performed for hydrogen implantation in pure tungsten and helium pre-exposed tungsten. A previous large-scale MD simulation of purely helium

irradiation will be used as the initial conditions for the large-scale simulations in order to understand the difference in hydrogen behavior in tungsten in a microstructure that includes helium bubbles and will be closer to what will occur under real plasma exposure.

Chapter 2

Multiscale Modeling of Materials

Radiation damage phenomena occur on a variety of different time and length scales and therefore it is necessary to develop a variety of modeling techniques to cover the physics occuring at these different scales. Because the initial radiation damage and subsequent effects occur over many orders of magnitude, no one modeling scheme is sufficient to capture the entire process. There are many different types of material modeling codes, ranging from the Density Functional Theory (DFT) codes that can only model a few hundred atoms for a few picoseconds up to the continuum codes that can model microns of material up to experimentally relevant timescales. Because of the complex behavior of the physical processes involved in PMIs (fuzz, blistering, etc.) no one simulation type will be able to explain the entire picture from atomistic defects and interstitial diffusion to tungsten fuzz growth. Atomistic modeling can describe the physical mechanisms of clustering and bubble formation but will never be able to observe the growth of fuzz itself because of computational constraints. On the other hand, reaction-diffusion codes can begin to describe the fuzz formation process but cannot model the atomistics and therefore depend on those codes as input for the various reaction rates needed. Many of these simulation types actually work hand in hand, DFT calculations can be used to fit interatomic potentials for MD and physical processes viewed in MD can be used to determine rates for Kinetic Monte Carlo (KMC) simulations. Therefore, both a "bottom-up" and "top-down" approach is used where both atomistic and continuum modeling is utilzed simultaneously in order to attack the problem with multiple tools instead of just focusing on one method and potentially missing an entire modeling regime. Fig. 2.1, depicts a schematic of the various simulation types that are used in modeling PSIs and their respecitive time and length scales.

This work will focus on molcular dynamics modeling of tungsten-helium-hydrogen for the purpose of studying plasma material interactions. MD is an atomistic style simulation tool that uses Newtonian mechanics to study the physical motion of

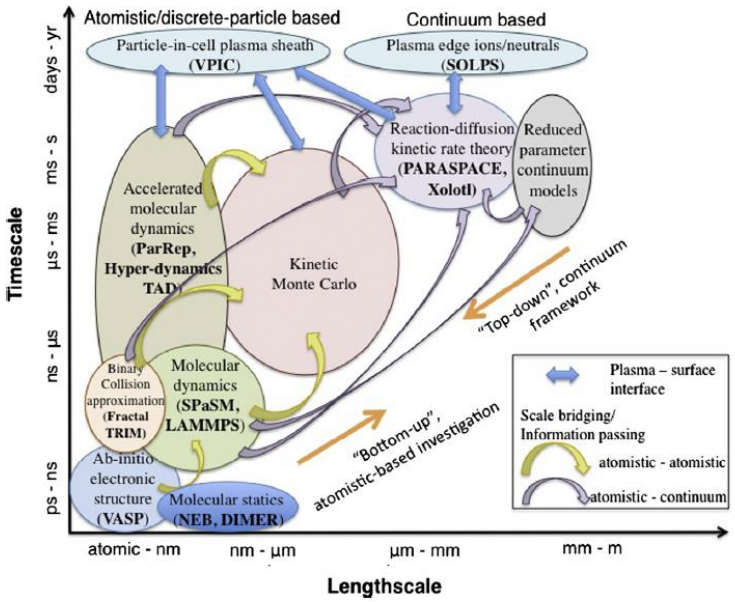

Figure 2.1: Diagram of the various types of multiscale modeling as a function of both lengthscale and timescale taken from [75]. Each modeling type works in tandem with eacth other and both small scale atomistic based and large scale continuum codes will be necessary for modeling the complex nature of PMIs that occur on various time and length scales.

atoms and dynamics of the system being modeled. Fast processes such as bubble growth, dislocation loop punching, sputtering, gas atom implantation and diffusion, and surface deformation can be studied for W-He-H using MD. These dynamics are occuring on timescales not observable by experiments and thus MD can provide insight into the physical mechanisms that contribute to experimentally observed effects like fuzz growth, surface deformation, and bubble formation that can, on the other hand, be difficult to model using kinetic monte carlo or cluster dynamics. MD can also be used to benchmark and form databases for continuum codes, such as tabulating energy barriers for various reactions.

2.1 Molecular Dynamics Methods

Molecular dynamics (MD) is an atomistic simulation method that tracks a system of particles over a given period of time using Newtonian mechanics. Simulation cells are typically on the order of nanometers and can be simulated up to about a microsecond. Many physical processes that occur in materials cannot be observed directly by experiments and because MD can model small, fast processes, it can be

a useful tool in understanding some of the underlying mechanisms that lead to the phenomena observed in experiments.

The MD algorithm begins by setting an initial position and velocity for each atom, defining interatomic potentials for each combination of atom type, and defining a timestep. The timestep needs to be small enough to conserve energy yet not so small that relevant time scales cannot be reached. Typical MD timesteps are on the order of femtoseconds. For every atom in the system, the Newtonian force:

$$\vec{F_i} = m_i \vec{a_i} \tag{2.1}$$

must be calculated. However, the force of each atoms is directly related to the interatomic potential for that interaction:

$$m_i \vec{a_i} = \sum -\frac{dV_{ij}}{dr_{ij}} \tag{2.2}$$

where V_{ij} is the potential energy between particle i and j given by the interatomic potential and r_{ij} is the distance between the two particles. Therefore, interatomic potentials need to be developed for the atomic system being modeled.

From the initial conditions set by the user, including positions, velocities, and interatomic potentials, the force can then be calculated from the potentials. Using the specified timestep, the Newton equations of motion can be numerically solved to determine the new atomic positions. The basic MD algorithm first begins with calculating the force on each atom based on equation 2.1 and the interatomic potentials using the initial conditions specified. Then, the equations of motion are solved over the timestep provided. Both positions and velocities are updated for every atom in the simulation. Next, the time is advanced and if the total time has not reached the desired simulation time, the alogrithm is repeated. A simplified diagram of the MD algorithm is shown in Fig. 2.3.

To solve the coupled partial differential equations used in MD, a Verlet style algorithm is typically used. A Verlet alogrithm is both simple and accurate while also being able to conserves energy, making it a popular choice for MD. The basic verlet alorithm involves two third order Taylor expansion of the position, one for both forward and backward steps in time. The Taylor expansions are described as:

$$\vec{x}(t + \Delta t) = \vec{x}(t) + \vec{v}(t)\Delta t + \frac{1}{2}\vec{a}(t)\Delta t^2 + \frac{1}{6}\dddot{\vec{x}}(t)\Delta t^3 + O(\Delta t^4) \tag{2.3}$$

and

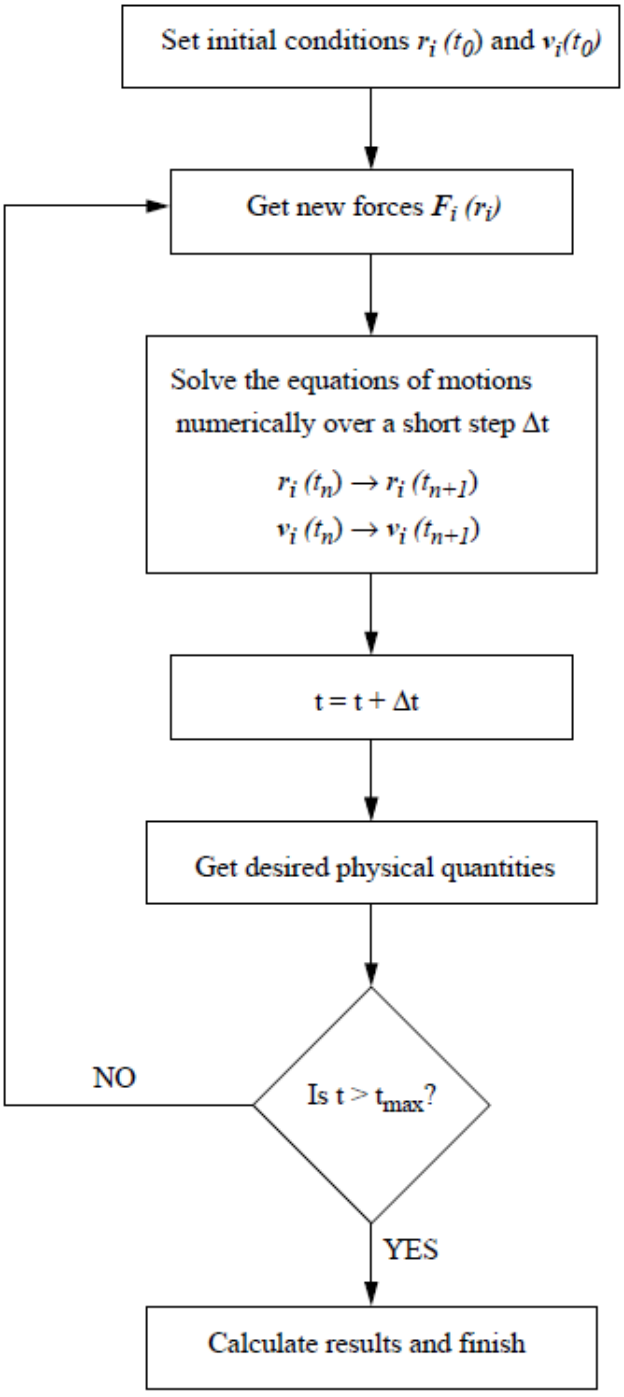

Figure 2.2: Diagram of the MD algorithm taken from [76].

$$\vec{x}(t-\Delta t) = \vec{x}(t) - \vec{v}(t)\Delta t + \frac{1}{2}\vec{a}(t)\Delta t^2 - \frac{1}{6}\dddot{\vec{x}}(t)\Delta t^3 + O(\Delta t^4) \tag{2.4}$$

where $x(t)$ is the position, $v(t)$ is the velocity, $a(t)$ is the acceleration, $\dddot{\vec{x}}(t)$ is the third derivative of the position, $O(\Delta t^4)$ is the fourth order term, and Δt is the time step.

Adding the two equations gives:

$$\vec{x}(t+\Delta t) = 2\vec{x}(t) - \vec{x}(t-\Delta t) + \vec{a}(t)\Delta t^2 + O(\Delta t^4) \tag{2.5}$$

These sets of equations can be used to solve for the new particle positions. However, one of the problems with the basic Verlet algorithm is that the velocities are never explicitly solved for and this is one of the quantities usually desired in MD output. A subset of the Verlet class, denoted as the Velocity Verlet alogrithm, does solve for the velocity itself and it is therefore the preferred Verlet algorithm used in MD.

The Velocity Verlet algoritm first uses the initial conditions to solve for the updated position as follows:

$$\vec{x}(t+\Delta t) = x(\vec{t}) + \vec{v}(t)\Delta t + \frac{1}{2}\vec{a}(t)\Delta t^2 \tag{2.6}$$

Then, from the new atomic positions and interatomic potentials the new acceleration is solved for:

$$\vec{a}(t+\Delta t) \quad using \quad \vec{x}(t+\Delta t) \quad and \quad equation \quad 2.1 \quad and \quad 2.2 \tag{2.7}$$

And finally, using $\vec{a}(t+\Delta t)$ the new velocities can be calculated:

$$\vec{v}(t+\Delta t) = \vec{v}(t) + \frac{1}{2}(\vec{a}(t) + \vec{a}(t+\Delta t))\Delta t \tag{2.8}$$

Now, the velocities at each time step can be calculated for each atom.

The MD code used in this work is the Large-scale Atomic/Molecular Massively Parallel Simulator (LAMMPS) [77] developed by Sandia National Lab. LAMMPS is optimized for running in parallel, including on GPUs, and can model systems of up to a billion atoms. When used in a parallel computing environment LAMMPS partitions the simulation into 3D subdomains that are then assigned to each processor using spatial-decomposition techniques. Processers can communicate with each other if atoms are on the borders between processors. LAMMPS has many different potential types that can be used to model various materials including solids, liquids, and gases

as well as different types of atoms including metals, polymers, and proteins. Various ensembles can be used, such as NVE or NVT, and different thermostats are available. Many different types of output can be calculated in LAMMPS to tailor simulations to accumulate the information needed in post-processing. Since LAMMPS is an open source code, users are able to modify the code to suit their needs.

The simulations in this work first begin by defining the geometry for a simulation cell that will be filled with bcc tungsten. Most simulations will include a free surface in the z direction and periodic boundaries in the x and y directions. Both smaller boxes, usually about 10 nm or less per side, as well as larger boxes, about 25 nm to 100 nm per side, are used in this work. If a free surface is used, it is necessary to create empty space, typically about 3 nm, both above and below the two surfaces, creating a tungsten slab, in order to preserve the free surface boundary condition. In order to prevent the slab from sliding within the simulation cell, the center of mass of the bottom layer of atoms is fixed. After creating the cell, the tungsten needs to be equilibrated to the appropriate temperature. This is done by first giving the tungsten atoms velocities based on a Maxwell-Boltzman distribution. Velocity rescaling is then performed every 100 timesteps for 5 ps and then turned off for 15 ps using a time step of 1 fs. For the rest of the simulation, the temperature is keep constant using an NVT thermostat.

After the equilibration process, the implantation and gas diffusion/evolution dynamics can begin. Gas atoms are implanted every 10 ps based on the 60 eV depth distribution from SRIM. Atoms in these simulations are not brought down with velocity but instead are implanted with zero kinetic energy by sampling a depth profile. This is advantageous in that bringing down atoms with velocity takes a much longer time because the timestep needs to be small due to the high energy of the gas atom. In addition, when an atom bombards the tungsten surface, there is a high probability that it will just reflect off the surface without implanting which again uses up a lot of simulation time. The diffusion process after the atom has implanted is where the interesting physics occurs so it makes sense to avoid wasting a lot of computer time since these resources are limited. To implant the atoms, a depth profile from SRIM[78] is first calculated and then this distribution is sampled in order to obtain the proper depth coordinate for each gas atom. The implantation process begins by first freezing all the atoms already in the system by setting their force equal to zero and then implanting the gas atom. The system is then minimized, the atoms are unfrozen, and then dynamics are run for 10 ps. This minimization process is done in order to prevent gas atoms from being placed too close to the lattice tungsten atoms and introducing large, unrealistic forces into the simulation. The timestep used in these simulations is either 0.5 fs or 0.1 fs depending on whether helium or hydrogen is beig simulated. This process is repeated until the desired simulation time is reached. Various information is extracted from the simulation including visulizations, depth profiles, and bubble size distributions.

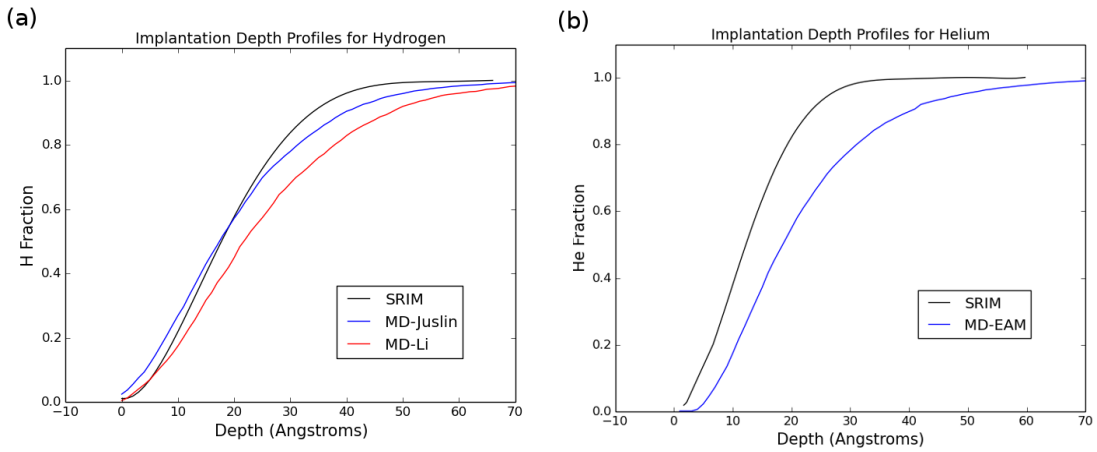

Figure 2.3: Plots of the depth distribution for 60 eV (a) helium and (b) hydrogen used to implant gas atoms. Both SRIM and MD data are plotted for comparison.

2.2 Interatomic Potentials

Interatomic potentials are a crucial component of MD simulations. They describe the forces between two atom types as a function of distance and are used in the integration algoritm. An MD simulation is only as good as the potentials used in the calculation. It is important to find accurate potentials that have been fit to parameters that are relevant to the physical processes being simulated. Interatomic potentials are typically fit to data, such as formation energies, from experiments or DFT. For the simulations in this work, potentials for each interactions in the W-He-H system need to be defined.

For the simulations involving just He, the W-W interactions were modeled using a Finnis-Sinclair potential [79] as modified by Ackland and Thetford [80] and further modified by Juslin and Wirth [71] with a Ziegler-Biersack-Littmark (ZBL) potential [81] at short distance. The Finnis-Sinclair potential is an N-body bound order potential that includes both a pairwise term as well as an embedding term that accounts for the local electron desntiy. The general equation for an N-body potential is:

$$V_i = F_i(\rho_i) + \frac{1}{2}\sum_{j \neq i} \phi_{ij}(r_{ij}) \quad where \quad \rho_i = \sum_{j \neq i} f_j(r_{ij}) \tag{2.9}$$

where V_i is the potential energy for particle i, F_i is the embedding energy, ρ is the local electron density, f_j is the embedding function, and ϕ_{ij} is the pair potential. The ZBL modification to the potential allows the forces to be more repulsive at short distances which is more approriate for high energy events like cascade simulations. It

is based on coulombic repulsion and takes the form of:

$$V(r) = \frac{1}{4\pi\epsilon_0}\frac{Z_1 Z_2 e^2}{r}\phi(\frac{r}{a}) \tag{2.10}$$

where ϵ_0 is the permittivity constant, Z_1 and Z_2 are the atomic numbers for the two atom types, e is the charge of an electron, r is the distance between the two atoms, and $\phi(r)$ is the screening function. As shown in figure 2.4, the ZBL modification to the potential has made the potential much more repulsive at short distances whereas the original potential was much too soft in this region. This potential has improved the interstitial properties and threshold displacement energy. It captures the trend in vacancy binding energies with size but has on offset in energy that is in contradiction with DFT calculations.

For W-He, a pair potential developed by Juslin and Wirth [82] was used. This potential is fit to DFT data of helium formation energies and well reproduces the DFT data for helium binding to small helium vacancy clusters. There are differences in the vacancy binding energy for small He-V complexes but in general, the trend is consistent with DFT. As for the He-He interaction, a pair potential by Beck [83] and modified by Morishita et al. [84] at short range was used. Again, a ZBL fit was added to the Beck pair potential in order to better replicate the repulsive nature of the interaction at short distances. Both the short and long range behavior of this potential is consistant with experimental data. The last helium potential used is for the He-H interacton when hydrogen is present in the simulation. For this interaction, a simple Lennard-Jones potential[85] was used. This potential takes the following form:

$$\phi(r) = 4\epsilon[\frac{\sigma}{r}^{12} - \frac{\sigma}{r}^{6}] \tag{2.11}$$

with both ϵ and σ being fitted parameters which are $5.9225x10^{-4}$ and 1.333 $\mathring{A}$ [86] for this pair interaction. All three helium potentials are shown in figure 2.5.

For simulations involving hydrogen, a seperate W-H potential that includes 3-body terms is needed in order to better describe the directional bonding in this particular interaction. A Tersoff[87] potential is often used which is a bond order potential which can account for the local bonding state. The general equaion for this potentials is:

$$V_{ij}(r_{ij}) = V_r(r_{ij}) + b_{ijk}V_a(r_{ij}) \tag{2.12}$$

where V_r is the repulsive part of the potential, V_a is the attractive part of the potential, and b_{ijk} is a term that adjusts the bonding state based on the local environment. The first Tersoff potential for the W-H system was developed by Juslin et al [88]. This potential uses data from both DFT and experiments to fit the various parameters in the Tersoff formulation. It well reproduces tungsten structural properties and cohesive energies as well as surface properties and point defect parameters, making it fairly

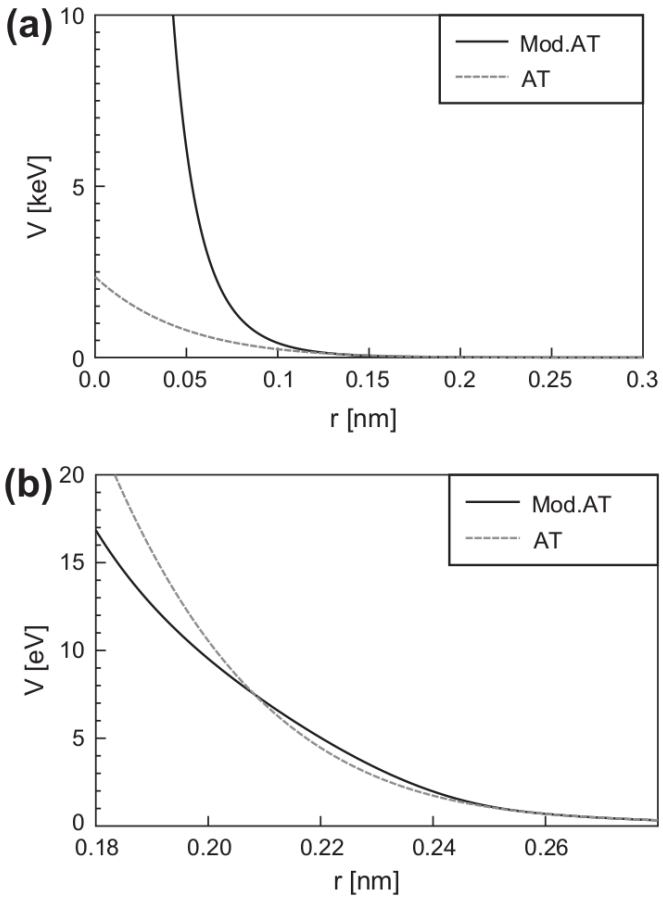

Figure 2.4: Plot of the W-H Finnis-Sinclair potential taken from [71] showing the (a) correction to the softness of the original potential at short distance and (b) depicting the range relevant to interstial properties. The original Ackland-Thetford formualation is shown in additon to the version further modified by Juslin. At short ranges, the Ackland-Thetford potential is much too soft and was made more repulsive by adding the ZBL component in the Juslin modification.

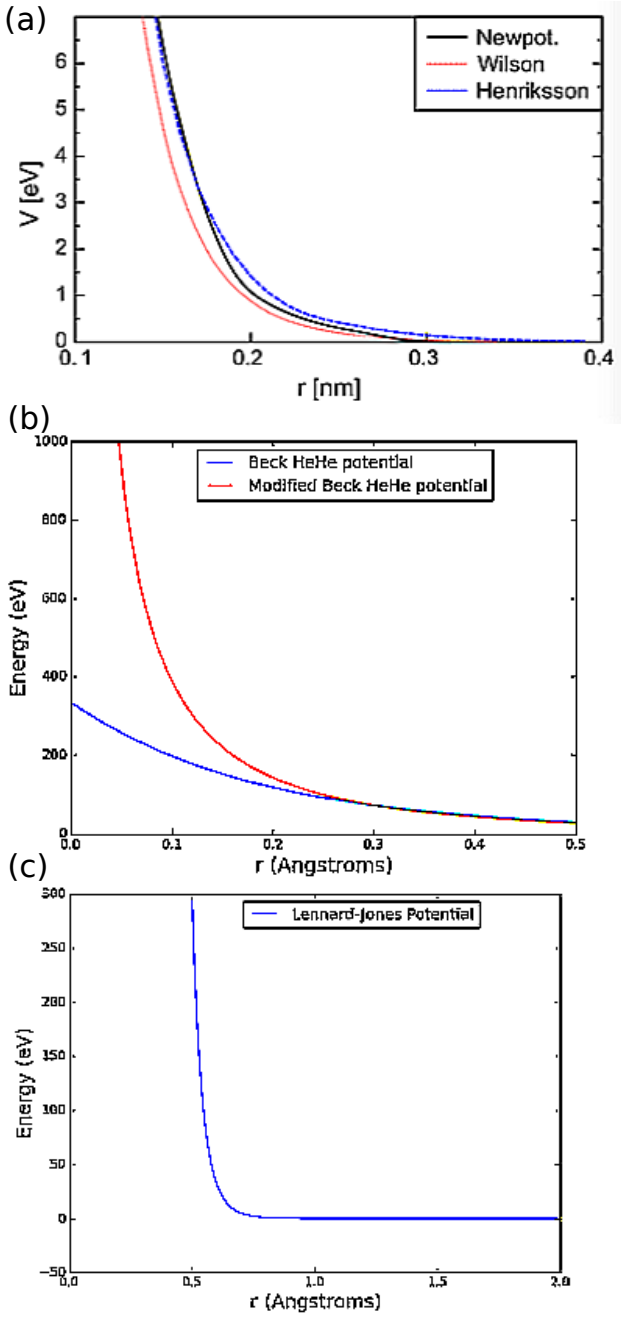

Figure 2.5: Plot of the potentials used for helium interactions including (a) W-He taken from [71], (b) He-He taken from [84], and (c) He-H.

comparable to the W-W Finnis-Sinclair potential. As for the W-H interactions, the solubility and diffusion of hydrogen as well as the formation energies and structures of both individual and small WH_n structures are well described. The H-H part of the potential is based on the Brenner[89] potential and is modified to be integrated with the Terosff style potential.

There is a second W-H Tersoff potential developed by Li et al [90] developed with the goal to improve upon the original potential by Juslin. One of the issues with the Juslin potential is the low tungsten vacancy energy, 1.68 eV as compared to 3.7 eV calculated by experiments. In addition the short cutoff distance for the W-H interaction, about 2.58 $\mathring{A}$, is too short since it doesn't even include the first nearst neighbor. Therefore, Li and coworkers refit the potential focusing the fitting parameters on defect properties that would be important for studying PMIs as well as increasing the cutoff distance for the W-H interaction. The structural and defect properties for this potential are comparable with both the Juslin potential and DFT parameters. However, because of the longer cutoff distance the Li potential is about 3 time slower than the Juslin potential, which is already about 30 times slower than the Finnis-Sinclair W-W potential due to the additional complexity from the 3-body terms. All W-H interactions from both potentials are shown in figure 2.6

From the potential plots, there are a few slight differences between the two potentials. For the W-W potential, the well is a bit deeper in for the Juslin potential, being about 5 eV as opposed to 3 eV. The potential also more quickly goes to zero for the Juslin potential, the energy is essentialy zero by about 1.2 Åbut has a longer taper for the Li potential where it does not reach zero until about 1.5 Å. In addition, the W-W potential is a bit smoother for the Li case. For the W-H part, the potentials are fairly similar with the Li potential having a slightly larger cutoff around 1 Å. This makes the well a bit wider compared to the Juslin potential. The H-H potential is the same between the two potentials and has the same general shape as the W-W and W-H parts.

Since potentials are so important in acquiring accurate and useful MD results, comparing the two different Tersoff potentials was the first task done in this work. This work was previously published in [91] and will be briefly discussed here. The goal of these simulations is to compare the Juslin and Li potentials looking at both hydrogen implantation and clustering in tungsten for two cases, a bulk simulation cell and a free surface simulation cell to get the hydrogen behavior both with and without the presence of a surface.

The setup for the two different cases is as follows. For the bulk case, a tungsten cell of 6 nm x 6 nm x 6 nm was created with periodic boundary conditions in all three directions. For the free surface case, the cell was 6 nm x 6 nm x 12 nm with periodic boundaries in the x and y directions and a free surface in the z direction.

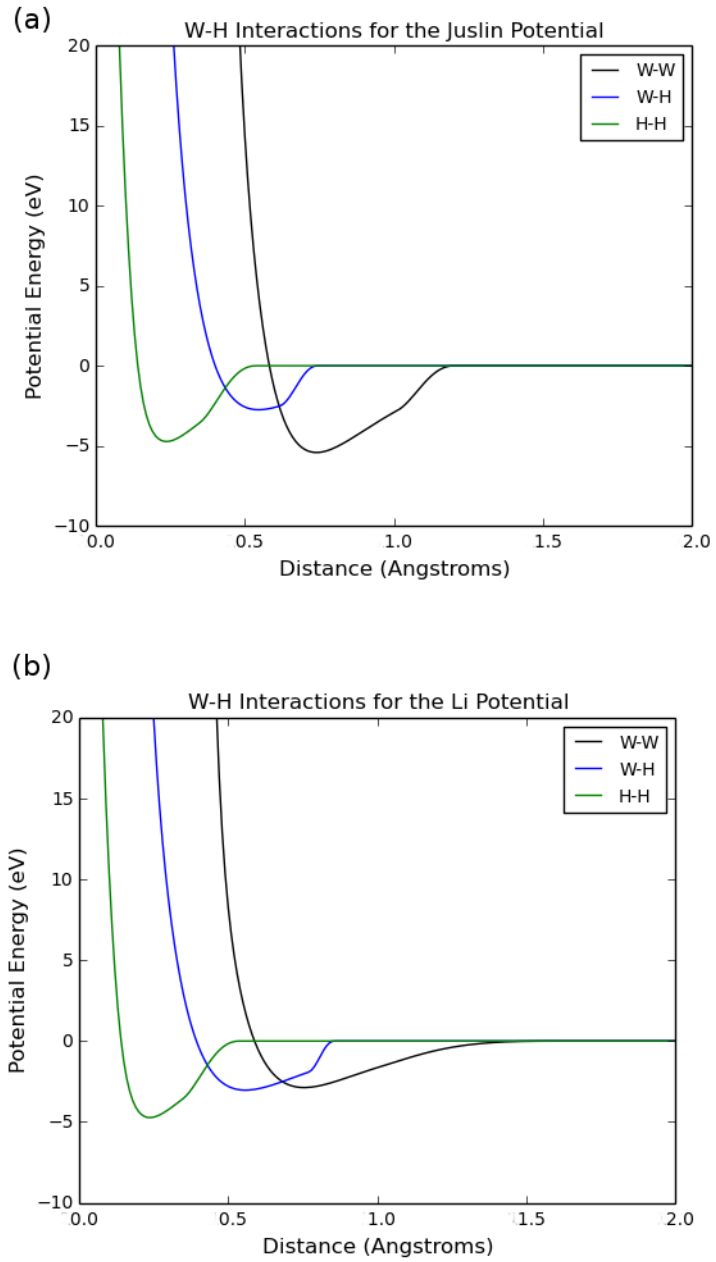

Figure 2.6: Plots for the WH interactions for the (a) Juslin and (b) Li potentials.

The tungsten block was then thermalized to 1200 K. This was done by first selecting velocities from a Maxwell-Boltzmann distribution. Velocity rescaling was performed every 100 timesteps for 5 ps and then turned off for 15 ps using a time step of 1 fs. After the equilibration process, gas atoms were inserted into the simulation box. For the bulk case, only hydrogen atoms were randomly inserted into the box while for the free surface case, both hydrogen and helium atoms were inserted in a 9:1 ratio based on the 60 eV depth distribution from SRIM. Atoms are inserted in the box every 6-8 ps and then run for 30,000 timesteps without a thermostat and then 5,000 time steps with velocity rescaling. An NVE thermostat was used throughout the entire simulation. A variable timestep was used so that no atom would move more than 0.001 nm per timestep and therefore the time between insertions is not a constant. This amounts to a flux of about $4x10^{27}m^{-2}s^{-1}$ for the free surface case. The simulations were run until 1000 atoms were inserted, which amounts to about 10 ns of simulation time. Simulations were run for both potentials and hydrogen behavior was observed.

The results for the bulk simulations will be discussed first. A visualization for the two potentials can be seen in figure 2.7. There is a clear distinction between the hydrogen clustering predicting by the two potentials; for the Juslin potential there are much larger clusters that seem to be oriented in the $< 111 >$ direction while for the Li potential, there is virtually no clustering and the hydrogen mainly exist as monomers in the material. The clustering was quantified by counting the number of atoms in a cluster using a cutoff of 0.32 nm and the distribution for both potentials can be seen in figure 2.8. The cluster distribution plots corroborate the visual information from the atomistic snapshots. With the Juslin potential, there is a large distribution of different sized cluster that can grow over 50 atoms in size. On the other hand, the cluster distribution for the Li potential is almost completely made up of monomers, which aren't shown in the graph for visualization purposes but consist of about 834 monomers as opposed to just 53 with the Juslin potential, making the total number of monomers much larger than with the Juslin potential. The largest clusters with the Li potential are of size three.

It is difficult to ascertain the cause of the different clustering behavior because both the W-W and W-H interactions are different between the two potentials. One reason for this difference may be explained by Frenkel pair formation energy. It is easier to form a Frenkel pair with the Juslin potential and hydrogen tends to cluster around the vacancy type defects. Therefore, as Frenkel pairs are formed, tungsten will be punched out in the $< 111 >$ direction and hydrogen will continue to migrate to these defects which will cause more Frenkel pairs to be created. Hydrogen will continue along these $< 111 >$ oriented defects to created the clusters seen in figure 2.7. This will not be as easy to do with the Li potential since the formation energy is higher. The vacancy formation energy is about twice as high so it is more energetically favorable

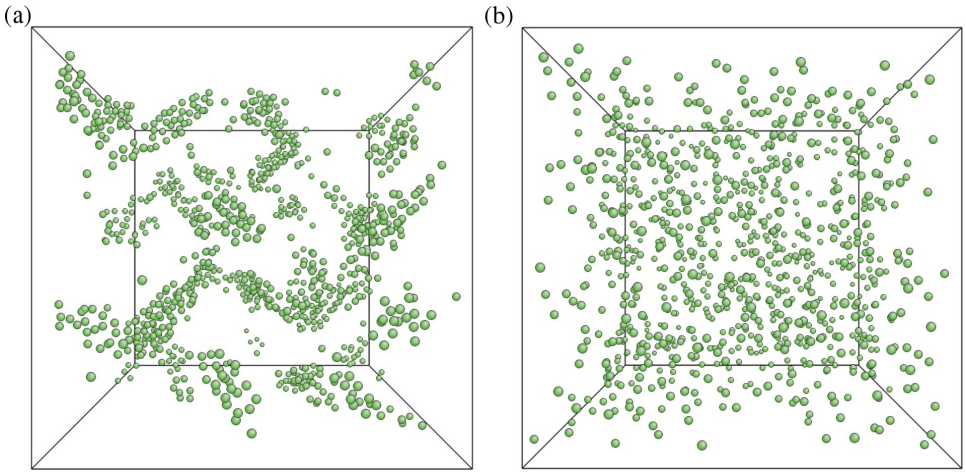

Figure 2.7: Atomistic snapshot of simulations of hydrogen implantation in a periodic box at 5.9atom% for the (a) Juslin potential and (b) Li potential. Hydrogen atoms were randomly inserted every 10 ps into a 6 nm x 6 nm x 6 nm sized box with periodic boundary conditions in all three directions. The Juslin potential generates $< 111 >$ oriented hydrogen clustered compared to the diffuse, non-clustered hydrogen of the Li potential

for the hydrogen to remain as monomers rather than undergoing trap mutation and initiating cluster growth.

The results for the free surface simulations are shown in figure 2.9. Again, there is a distinct difference between the two different potentials. For the Juslin potential, the clustering behavior seen in the bulk simulations is observed here with large $< 111 >$ oriented hydrogen clusters appearing just below the tungsten surface. There are very few hydrogen atoms at the surface itself but there is some surface roughening denoted by the magenta adatoms in figure 2.9. For the Li potential, there is again very little clustering in the bulk combined with very different behavior near the surface compared to the Juslin potenial. In this case, the hydrogen is almost entirely at the tungsten surface and located at hollow sites forming an almost grid-like pattern. Another difference is in the total hydrogen retention, the Li potential has a much lower retention compared to the Juslin potential at 60% versus 87%, respectively. It is difficult to detmine which surface behavior is correct due to the lack of DFT data for hydrogen near tungsten surfaces. However, experiments have shown that on a (100) surface, the hydrogen prefers to occupy the bridge site, which is observed in the Juslin potential and inconsistent with the Li potential. Additional DFT data is needed in order to better fit the W-H behavior which is currently fit with mainly bulk W-H properties.

Another study was done to asses hydrogen absorption on tungsten surfaces using both the Juslin and Li potential by Guterl et al [92]. In the potential comparison

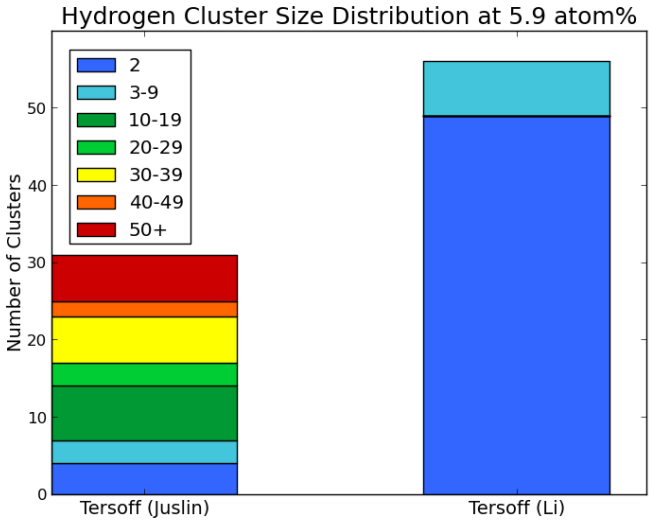

Figure 2.8: Hydrogen cluster size distribution for the bulk simulation. Two atoms are considered to be in the same cluster if they are within 3.2 Åof each other. Sincle hydrgoen atoms are not shown here; there were 53 with the Juslin potential and 834 with the Li potential.

discussed above, it was observed that hydrogen was desorbing as monomers as opposed to the molecular hydrogen desorption expected from theory. The work by Guterl further investigated this discreption in the Juslin potential and it was found that the barrier for hydrogen recombination at the surface was about 7 eV, much higher than experimental values. This high energy barrier was preventing hydrogen from recombining at the suface so it could desorb as H_2. The reason for the steep barrier was linked to the γ_{H-W-H} term in the Tersoff potential formulation. The original value was 12.33 and this was adjusted to 0.5 which yielded a new surface recombination energy of 1.5 eV, much more consistent with experimental observations. This potential has been tested and does allow for molecular desorption of hydrogen from the surface.

After evaluating the various W-H potentials, it was decided that for this work the Juslin potential modified for molecular hydrogen desorption by Guterl would be used for any simulations involving hydrogen. Although the Li potential better replicates bulk values, this potential is about 3 times slower than the Juslin potential which is already roughly 30 times slower than the W-W Finnis Sinclair potential. In addition, the modeling for this work will involve free surfaces and the modified Juslin potential better represent surface properties.

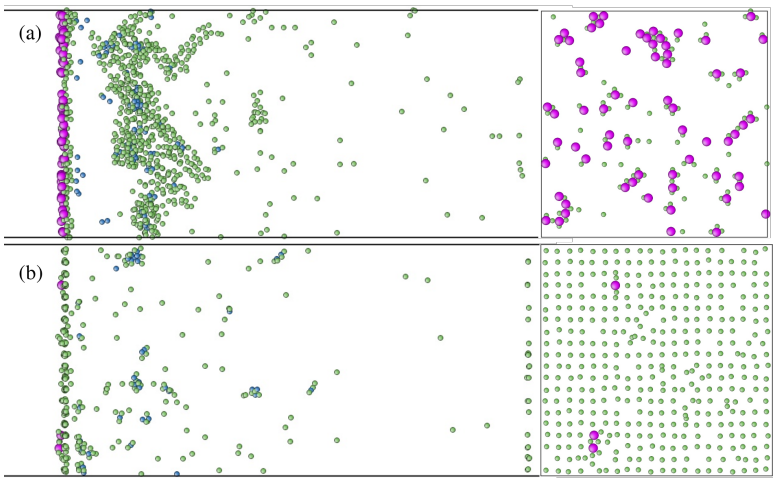

Figure 2.9: Snapshots of hydrogen implantation simulations with a free surface at a flux of $3.6x10^{27}m^{-2}s^{-1}$ for the (a) Juslin potential and (b) Li potential. Gas atoms are inserted into a 6 nm x 6 nm x 12 nm box every 10 ps based on the 60 eV depth distribution from SRIM. There are periodic boundary conditions in the x and y directions and a free surface in the z direction. Green, blue, and magenta atoms represent hydrogen, helium, and tungsten adatoms respectively. There is clearly a different behavior near the surface depending which potenial is used.

2.3 Visualization

One of the benefits of MD is that not only are quantitative values calculated but visual output is available which can aid in discovering processes and mechanisms that might not be easily unveiled with typical output data. During an MD simulation, particle positions are tracked and can be output in order to visual the positions of atoms as the simulation progresses, being a key component in obtaining early results of a given simulation. Visualization can also aid in assuring that the simulation is evolving properly and can be used to easily fix any issues that may have been occuring. With a bit of post-processing, various quanitities can be highlighted such as suface adatoms or bubble sizes. There are various visualization tools that can read in output from LAMMPS and the ones used in this work are Atomeye [93] and Ovito [94]. LAMMPS ouput is generated in a dumpfile that can then be read in with the visualization software. Data can be ouput for a specified interval of time into the dumpfile which can contain a variety of atomic information such as atom IDs, atom types, and coordinates or MD calculated values such as the stress per atom or cluster sizes. All of this visual data can then be analyzed to obtain new and interesting results to corroborate the quantitaive results.

2.4 Role of Supercomputing

The large-scale simulations for this work contain roughly 4 million tungsten atoms and therefore it will be necessary to use high performance computing to achieve results. This is especially true for the W-H modeling with the Tersoff potential, which is about 30 times slower than the Finnis-Sinclair potential used in the purely W-He simulations. In the case of W-H, the use of GPUs to speed up the run time is very appealing. LAMMPS is designed to be run as an efficient parallel code and with the optional user packages, namely the USER-CUDA and GPU packages, the LAMMPS code can be modified to run calculations on the GPU, which saves considerable time and allows large simulations of the W-H system to be attempted.

Resources from three different computing facilites are used in this work: Edison at the National Energy Research Scientific Computing Center (NERSC), Mira at the Argonne Leadership Computing Facility (ALCF), and Titan at the Oak Ridge Leadership Computing Facility (OLCF). The W-He simulations are run mainly run at NERSC while the W-H simulations are run at OLCF to make use of Titans GPU capability. With the W-H-He simulations, there is no GPU capability for every potential type implemented in LAMMPS necessary for this system. Therefore, these simulations are run on Mira at ALCF instead of Titan. Computing hours at ALCF and OLCF are awarded through a DOE Advanced Scientific Computing Research Leadership Computing Challenge award.

Chapter 3

Modeling of Helium Diffusion Near Defects

3.1 Motivation

This chapter discusses the results from a series of molecular dynamics simulations to study helium clustering and diffusion near defects in tungsten including the nanotendrils present under plasma irradiation as well as grain boundaries. It is still not well understood exactly how helium implantation under plasma-like conditions creates fuzz in the first place. There are a few theories in the literature but no definitive answer to explain fuzz growth at all stages. Helium bubbles have been observed inside the fuzzy tendrils and have been determined to play an important role in the early surface deformation leading to fuzz formation. One of the key unknowns in this process is how the fuzz continues to grow deep into the material. At the low helium energies that will be implanted at the divertor surface, typically 100 eV or less, the implantation depth is only a few nanometers into the material[36][37]. However, the fuzz grows to depths on the order of microns into the tungsten[12] despite the shallow implantation depth. It is still unknown exactly how the helium reaches the bottom of the nanotendrils to continue growing the fuzz to such depths. It will be important to understand this process in full in order to devise divertor materials to mitigate the potential damage from nanotendril growth. If the mechanism for continual fuzz growth deep into the material can be established, there may be ways to even prevent the helium ions from creating a thick fuzz layer in the first place.

The simulation time achievable with MD is not anywhere near long enough to generate fuzz structures from a clean tungsten surface. Microsecond long simulations are achievable but fuzz growth does not occur until after a few hundred to thousands

of seconds of low energy helium implantation. With current computational power it is virtually impossible for MD to achieve this much simulated time, however it is possible to create an initial geometry that resembles a nanotendril and then study the helium behavior within this structure. A typical tendril is approximately 10-50 nm in width and can grow up to microns in depth. Again, this is very much outside the simulation size that MD can handle. Instead, a scaled down version of this tendril geometry is modeled with MD to study the early stages of tendril growth. In this section, simulations of helium implantation in smaller tendril sizes will be detailed.

In addition, helium is found to become trapped at grain boundaries in previous MD simulations [95]. It was observed that once the helium reached the grain boundary, it becomes trapped there with significantly reduced mobility. It will be important to understand the 2D diffusion towards the grain boundary to provide a computational dataset to benchmark continuum reaction-diffusion cluster dynamics models. To better understand this diffusion, a large-scale simulation where the helium is implanted in an area between the grain boundaries, but not on the grain boudary itself, has been performed to evaluate the helium diffusion transport and spatial evolution of helium clusters in the vicinity of this defect.

3.2 Small Tendril Modeling

The first section of this chapter describes the results from small simulations of helium implantation in a tendril-like geometry. Helium implantation has been performed strictly within the tendril itself in order to study tendril stability, helium clustering, helium diffusion and retention in addition to analyzing the impact of of varying temperature and geometry.

3.2.1 Methods

Molecular dynamics simulations were performed to study helium implantation in a tendril-like geometry. A 9 nm x 9 nm x 9 nm tungsten block was first created with periodic boundary conditions in the x and y directions and a free surface in the z direction. A cylinder is placed on the center of the surface that is 6 nm in height and 5 nm in diameter and is topped with a half sphere that is 5 nm in diameter. The cylinder-half sphere combination provides a tendril structure where helium atoms will be placed. Experiments have indicated that tendrils are about 10-50 nm in diameter[39]. The structure here is on the lower end of this size, but has been chosen to approximate a tendril in the early stage of growth. Figure 3.1 depicts the tendril geometry. After creating the initial structure, the tungsten was equilibrated to the

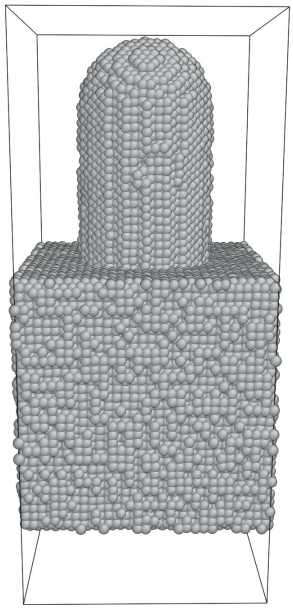

Figure 3.1: The initial geometry for the tendril-like geometry simulations which is comprised of a 6 nm x 6 nm x 6 nm box topped with a 6 nm tall cylinder and a half sphere that is 5 nm in diameter.

appropriate temperature. This was done by first selecting velocities from a Maxwell-Boltzmann distribution and then performing velocity rescaling every 100 timesteps for 5 ps with an NVE thermostat followed by 15 ps with no velocity rescaling using a time step of 1 fs.

Helium was then implanted strictly in the tendril region based on the 60 eV depth distribution from SRIM. The depths did take into account the curvature of the top of the tendril in calculating the appropriate z coordinate to place the helium. Helium atoms are implanted every 10 ps, leading to a flux of $1.2x10^{27}m^{-2}s^{-1}$. The timestep depended on the temperature of the simulation, for temperatures between 1200 K and 1700 K the timestep was 0.5 fs while for temperatures from 1800 K to 2000 K the timestep was 0.1 fs. The difference in timestep was due to the higher mobility of helium at the higher temperatures and it was necessary to use a smaller time step in order to conserve energy. For each simulation, up to 20,000 helium atoms were inserted which yielded a fluence of $2.4x10^{20}m^{-2}$. The potentials used for this set of simulations are as follows. For the W-W interactions, a Finnis-Sinclair potential [79] as modified by Ackland and Thetford [80] and further modified at short distance by

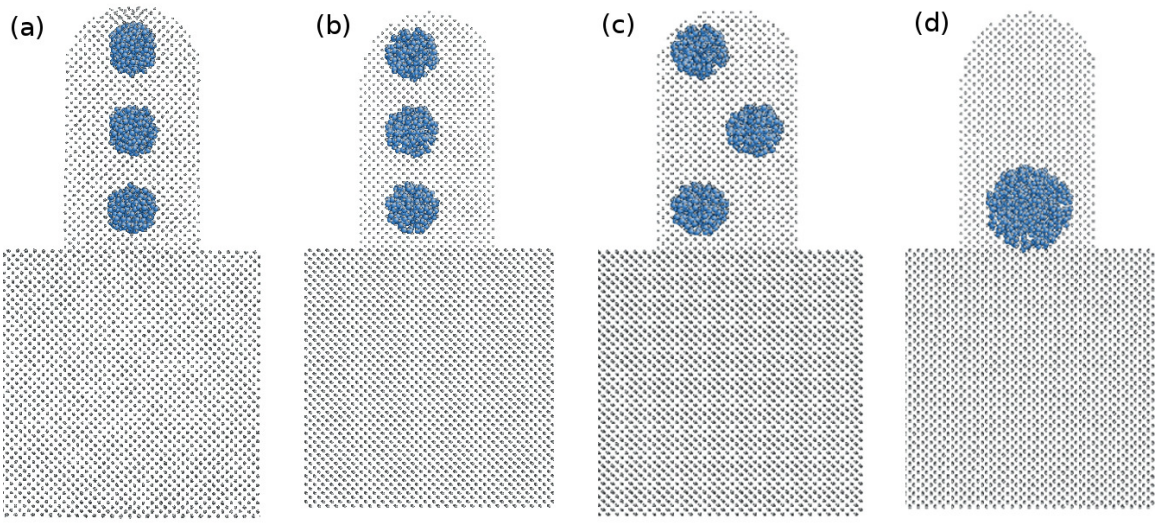

Figure 3.2: Tendril geometry for simulations involving intial helium bubble distributions for (a) centered bubbles, (b) side bubbles, (c) offset bubbles, and (d) single bubbles at the base of the tendril. Gray and blue atoms denote tungsten and helium atoms respectively. For (a), (b), and (c) the bubble is 1 n in radius with a 1.2 He/V ratio. For (d) the bubble has a 1.5 nm radius and a 0.5 He/V raio.

Juslin and Wirth[71] was used. For the W-He interactions, a pair potential developed by Juslin and Wirth [71] was used. The by Beck potential [83] modified by Morishita et al. [84] at short range was used for the He-He interactions.

A few parameters were varied within this set of simulations including temperature, geometry, and initial helium bubble distribution. Temperatures included 500K, 1200 K, 1500 K, 1700 K, 1800 K, 1900 K and 2000 K. 1200 K was used as a base case for simulations that varied other parameters. Tendrils have been shown to only form between temperatures of about 1000 K to 2000 K and thus temperatures were chosen within this range of stabilty. Variations in both height and radius were also simulated. Tendril heights of 4.8 nm and 8 nm were compared to the base case of 6 nm and radii of 1.3 nm and 3.8 nm were compared to the base case of 2.5 nm. Finally, varying distributions of bubbles were placed within the tendril. Experimental transmission electron microscopy observations indicate the presence of cavities, which are persumed to be helium filled, within nanotendrils [39], and thus we expect the bubbles will influence their evolution and the diffusion of helium within the tendril. Initially, a set of three bubbles with a radius of 1 nm and 300 helium atons were placed within the tendril. Three different cases that varied the bubble placement were simulated. For each, the center of mass of the helium atoms within the initial bubbles were centered at depths of 0.5, 1.0 and 1.5 nm from the top of the tendril, respectively. The three different cases are based on different lateral positions of the

bubble including one where all the bubbles are centered in the tendril, one where all the bubbles are placed to one side of the tendril, and one with offset bubbles where two bubbles are on one side of the tendril and one on the opposite side of the tendril. In addition to the three bubble structure, one other bubble variation was studied. For this case, one large bubble was placed at the bottom of the tendril centered at a depth of 5.6 nm to see if helium would be attracted towards this bubble. The initial bubble placement is shown in figure 3.2.

3.2.2 Results

As helium is inserted into the tendril, the helium is observed to cluster into bubbles comparable to previous MD simulations[27][37] of helium implantation on planar tungsten surfaces. Figure 3.3 depicts atomistic snapshots at the end of the simulations at a fluence of $2.4x10^{20}m^{-2}$ for three different temperatures. In all three cases, a distribution of different bubble sizes can be seen within the tendril. Most of the bubbles are located in the dome portion of the tendril where the helium has been implanted and remains due to self-trapping, which is possibly enhanced due to the surface-mediated trap mutation first observed by Hu and co-workers [38]. In the cases with higher temperatures, at 1500 K and 2000 K shown here, only one single helium atom has diffused to the bottom of the tendril. But most of the helium is located near the top of the tendril and usually within a larger bubble. While there are large bubbles located within the tendril, there seems to be very little deformation of the tendril itself, mostly just some roughness around the upper half of the tendril which is due to the dislocation loop punching that occurs when the helium bubbles begin to expand. In fact, throughout the simulation, the tendril remains structurally stable even at 2000 K which is near the threshold of tendril stability observed in experiments[9]. However, at 2000 K, a visual inspection of the atomistic snapshots concludes that there is both less helium retention within the tendril and smaller helium bubbles that form although this could be partially dependent at the point in time these snapshots were taken at.

In regards to the helium retention, the percent retention as a function of fluence is plotted in figure 3.4 for all temperatures. Each line is the result obtained from a single simulation over the entire 20 ns but is representative of each temperature respectively. One striking phenomena that can be inferred from this plot is the trajectory of the helium retention. At first, the retention is very high but then quickly begins to decrease towards values under 20%. As the fluence increases, the retention eventually flattens out and reaches an approximate steady state value around 10% or lower. This is in contrast to previous MD simulations which show higher retention, typically above 60%, for simulations with a similar flux of $10^{27}m^{-2}s^{-1}$ and lower retention, typically less than 40%, for fluxes of $10^{25}m^{-2}s^{-1}$ [75]. Therefore, with the expected

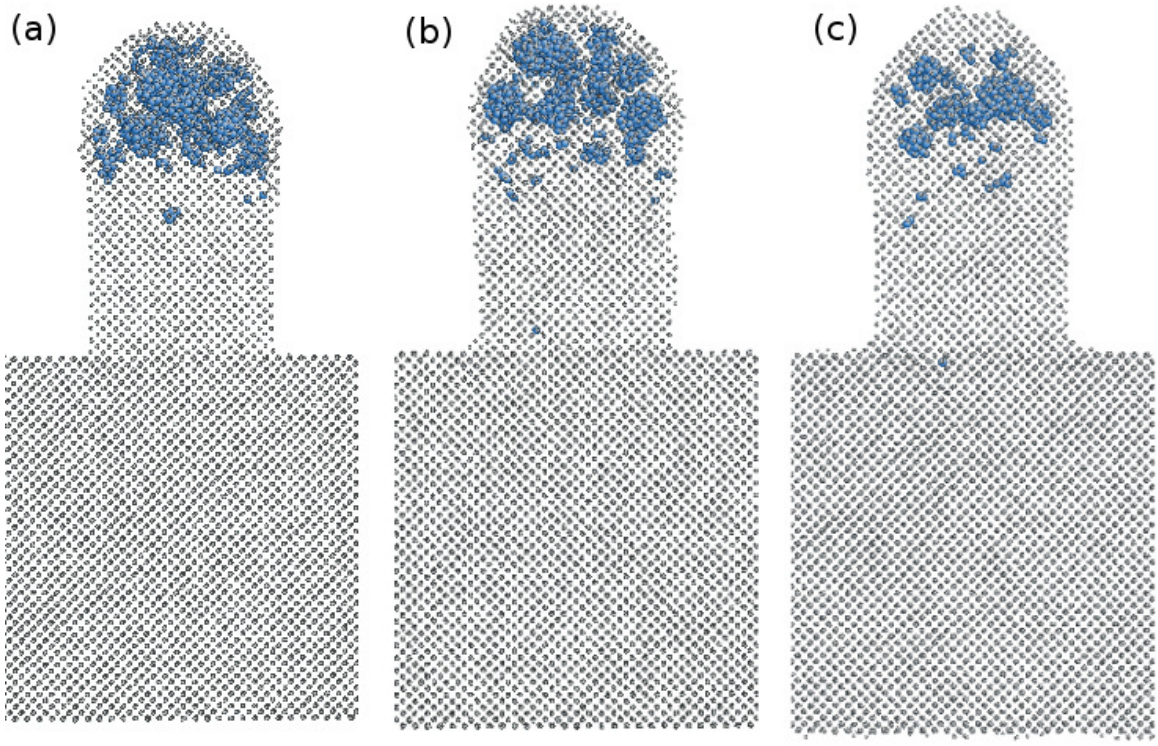

Figure 3.3: Atomistic snapshots of tendrils after 20,000 helium insertions for temperatures of (a) 1200 K, (b) 1500 K, and (c) 2000 K. Gray and blue atoms denote tungsten and helium atoms respectively. An array of different sized helium bubbles populate the inside of the tendril which is similar to the bubbles seen in previous MD simulations[27][37] on clean tungsten surfaces. The helium retention is clearly lower at the higher temperature case of 2000 K. Note that in the case of 1500 K and 2000 K, there are helium atoms that have diffused to the base of the tendril.

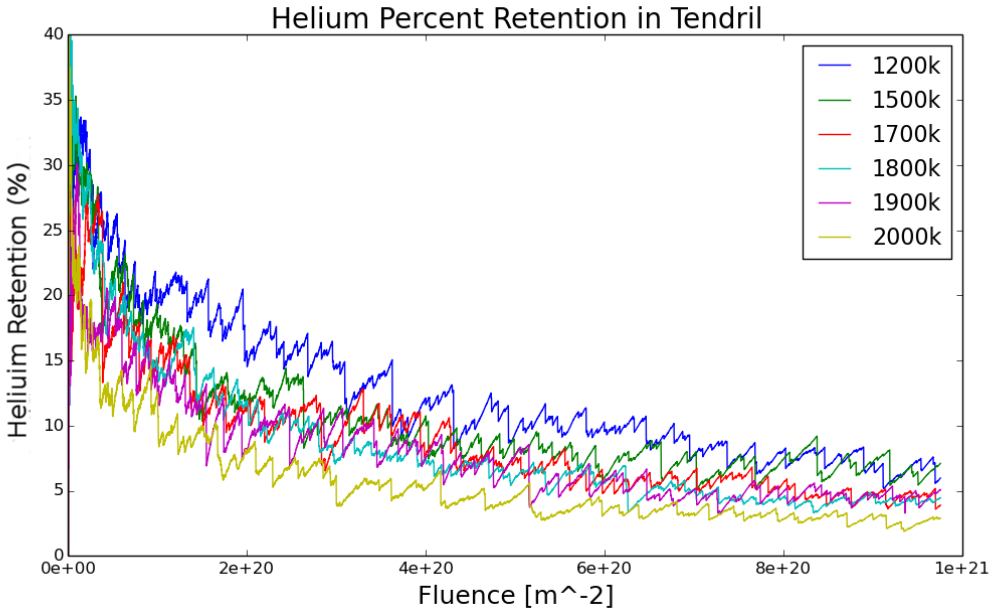

Figure 3.4: Helium percent retention as a function of fluence for a variety of temperatures. The final retention is typically around 2-10% with lower precentages observed for higher temperatures. For all cases, the retention initially decreases until it reaches an approximate steady state near the end of the simulation.

high flux in these simulations, a higher retention is expected. Curiously, the retention is very jagged even once it reaches this "steady state". This indicates that as helium is added into the tendril, the retention increases until the bubbles get too big, the increased bubble pressure causes helium to be released, and subsequently the helium retention falls. This occurs over and over again until the retention reaches a point that as helium is added to the tendril, roughly the same amount will be released leading to the steady nature of the retention at higher fluences.

This is very different than simulations where helium is implanted in a typical geometry without a tendril. In this case, when helium builds up in bubbles just below the tungsten surface, the increasing bubble pressure eventually leads to loop punching, which will deform the surface with the creation of tungsten adatoms, or if the pressure is high enough, the bubble will burst leading to a large drop in helium retention as well as cratering and other destructive surface deformation[27][37]. In the case of the implantation within a tendril, the helium will similarly accumulate in bubbles with rising pressure. However, in this case the tendril has a much larger surface to volume ratio. This allows the bubbles to more easily release helium because of the larger surface area. In addition, the volume of tungsten available for bubble growth is much smaller which restricts the ultimate size of the bubble. These two processes are apparently responsible for the continual bubble growth and helium

release without destroying the tendril surface in the process leading to the tendril stability observed throughout the simulations for temperatures up to 2000 K and times of up to 200 ns.

As well, a modified bubble bursting mechanisms was observed during the simulations. Helium leaves the simulation in two different ways. First, single helium atoms are able to easily diffuse to the surface and desorb due to the large surface area available in the tendril-like geometry. The second method applies to bubbles that reach a sufficinetly high pressure where helium release is necessary. In this case, the helium bubble will typically expand and create a small pinhole rupture that allows the helium atoms in the bubble to easily escape. The helium release from the pinhole rupture causes the drops in retention shown in figure 3.4. After most of the helium leaves the bubble, the pinhole self-heals and the remaining cavity can accumulate helium once again.

Figure 3.5 shows additional data of the average helium retention at a fluence of $1x10^{21}m^{-2}$ as a function of temperature and more explicitly shows the reduced helium retention with increasing temperature. The data plotted in 3.5 is an average calculated over five simulations with accompying error bars. At 1200 K, the average helium percent retention is roughly 6.8% with little uncertainty across multiple simulations. At 1500 K, the temperature is about 6% and between 1700 K and 1900 K the retention is closer to 4%. The lowest retention observed was about 3.3% at 2000 K. Although at intermediate temperatures the retention is similar, there is a clear trend in reduced helium retention at higher temperatures even with the calculated error bars.

Most of the helium retained within the tendril-like geometry resides in bubbles that form within the tendril as depicted in figure 3.3. A quick glance at the atomistic snapshots indicates that at lower temperatures, the helium bubbles appear larger and more numerous than for the simulations at higher temperatures. The size of the largest bubbles and the total number of bubbles within the tendril were quantified for each temperature. This analysis was performed for the total inventory of helium within the simulation. Two helium atoms were considered to be within the same cluster if they were within 0.3 nm of one another. However, due to the continual increase in helium retention followed by sharp drops in retention, it was necessary to accumulate data over the last 10%, or 20 ns, of the simulation. If, for example, just the data at the end of the simulation were analyzed, it might not be entirely accurate for the simulation as a whole if the selected analysis time involved sequences when the bubbles just released a large amount of helium or if the bubbles were still in the process of growing. Therefore, for the largest bubble calculation, the cluster with the largest quantity of helium was tracked and the largest inventory of helium before release was recorded. After a bubble would decrease in size, the next bubble that became the largest was then tracked and all the values were then averaged for

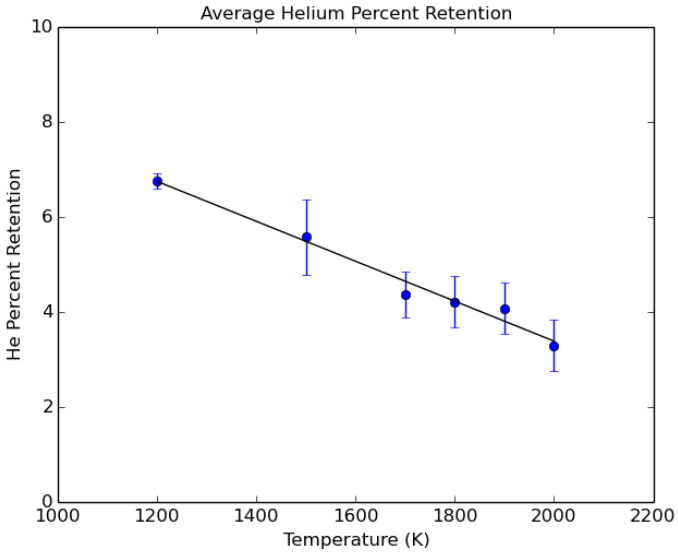

Figure 3.5: The average helium retention as a function of temperature. There is a clear trend of reduced retention as the temperature increases.

each temperature. For the total number of clusters, the average value over the last 20 ns was calculated and then averaged. Data was collected following each helium atom insertion, or every 10 ps.

The results are presented in figure 3.6. For the largest bubble size, the average seems to remain between 100 and 250 helium atoms. The average size at the lowest temperature of 1200 K is slightly larger, about 225 helium atoms, while at moderate temperatures between 1500 K and 1800 K, the values are fairly consistent with one another, around 175 helium atoms. At 2000 K, the average helium bubble is the lowest, containing only 110 helium atoms compared with 225 at 1200 K. However, the error bars are quite large within this analysis, indicating the range of bubble size before releasing helium. Again it is important to indicate that this size distribution analysis has been performed during the last 20 nanoseconds of the MD simulation when the helium retention is approximately at a steady state value, but for which there is still variation associated with both helium release events as well as bubble growth. Nevertheless, it does seem that the bubble sizes are smaller at 2000 K, which would be consistent with visual observations. Regardless of the temperature, these bubbles are much smaller in regards to helium content then some of the larger bubbles seen beneath planar surfaces, which can eventually grow large enough to contain over 800 helium atoms [96].

For the total number of helium bubbles within the tendril, a much clearer trend is observed as a function of temperature. At lower temperatures, the average number of bubbles within the tendril is higher, with about 65 helium bubbles at 1200 K. On the

other hand, this value is much lower at higher temperatures, with about 30 helium bubbles at 2000 K, which is less than half the value at 1200 K. The bubble density quantity also tends to be much more consistent across the simulations compared to the largest bubble size, as indicated by the much smaller error bars in Figure 3.6. These two results are consistent with the observations from the atomistic snapshots as well as the helium retention, namely that the helium retention is higher at the lower temperatures. At lower temperatures, there are typically more bubbles and on average, the bubbles are larger, which corresponds to a higher value of retained helium within the tendril while the reverse is true at higher temperatures.

With all the helium bubbles growing within the tendril, the shape of the tungsten itself has slightly modified throughout the simulation in order to accomodate for the excess volume produced by the helium being implanted. Namely, the tungsten tendril tends to bulge near the area of implantation and subsequent helium clustering. The total displacement of the tungsten between the beginning and end of the simulation was quantified by calculating the displacement vector and color coding the tungsten atoms respectively. The atomistic images of this are displayed in figure 3.7, in which the blue indicates the atoms that have not been displaced and red indicates the atoms that have been displaced at least 3.0 nm. Temperatures of 1200 K versus 2000 K are shown. As seen in Fig. 3.7, the tungsten near the top of the tendril are displaced the most, which is consistent with where the helium bubbles are located. In addition, there tends to be more tungsten atoms displaced along with larger displacement magnitudes at 2000 K. This may indicate that there is more roughening at 2000 K or that the atoms may be more mobile at the higher temperatures.

The tungsten atoms are displaced through helium bubble expansion and dislocation loop punching. In previous MD simulations, the typical concentration of helium atoms in large-scale simulations are typically around 3-4 He/V with pressures above equilibrium [96] for bubbles a few nanometers below the surface. For helium densities well above equilibrium gas pressure, the bubble pressure can grow sufficiently large that the pessure must be relieved either through vacancy absorption or self-intersitial atom/dislocation loop emission. Therefore, the helium concentration for the clusters within the tendril were calculated. This was done by using a Wigner-Seitz analysis, which breaks down the simulation into small volumes and keeps track of the number of atoms in each volume. The final geometry is compared with the initial geometry and any volume that has additional atoms is determined to contain an interstitial and any volume with less than the initial number of atoms is determined to contain a vacancy. This analysis is performed for each temperature and the values are tabulated in table 3.1. On average, the He/V ratio is between 1 He/V and 2 He/V, which is comparable for bubbles below planar surfaces for the same ligament thickness as the bubbles in the tendril simulations[96] while bubbles further below the surface, greater than 4 nm, have a He/V value of 3-4. However, the error bars at each temperature are fairly large. For example, at 1200 K the He/V ranged from 0.5 to 8. For the largest

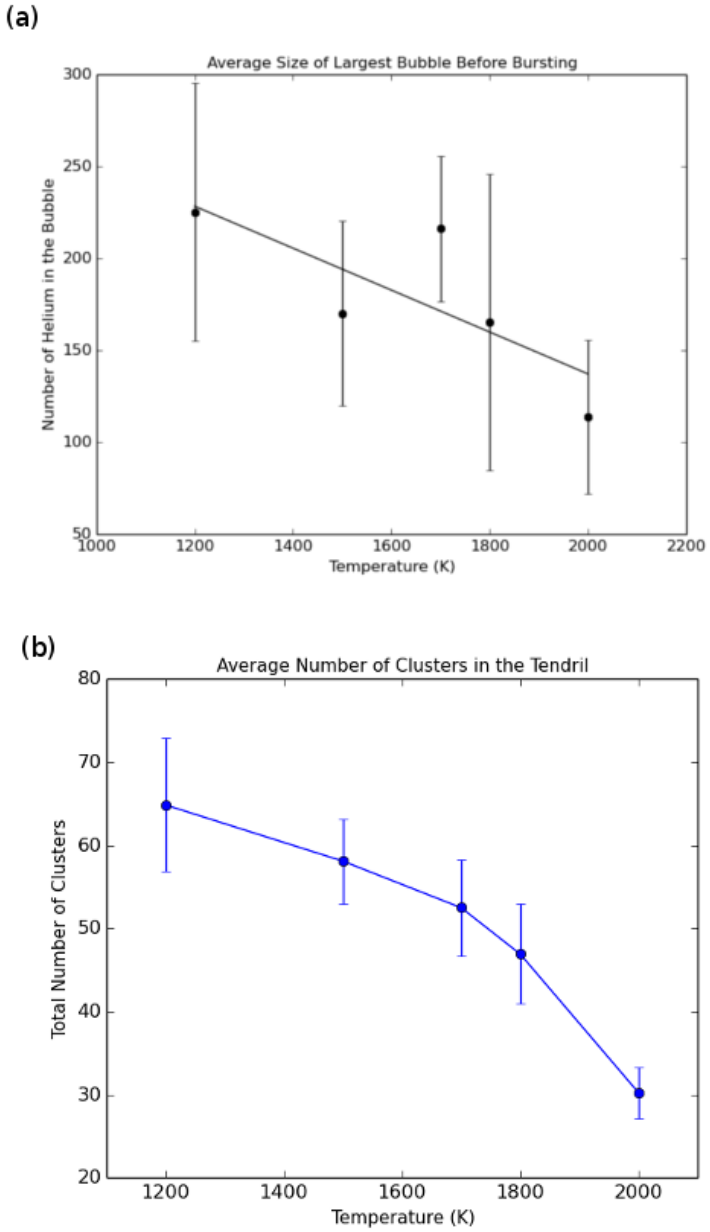

Figure 3.6: Plot of the (a) average largest helium bubble size within the tendril before bursting and (b) the average number of clusters within the tendril. Data was collected every atom insertion, or every 10 ps, and averaged over the last 20 ns of simulation time.

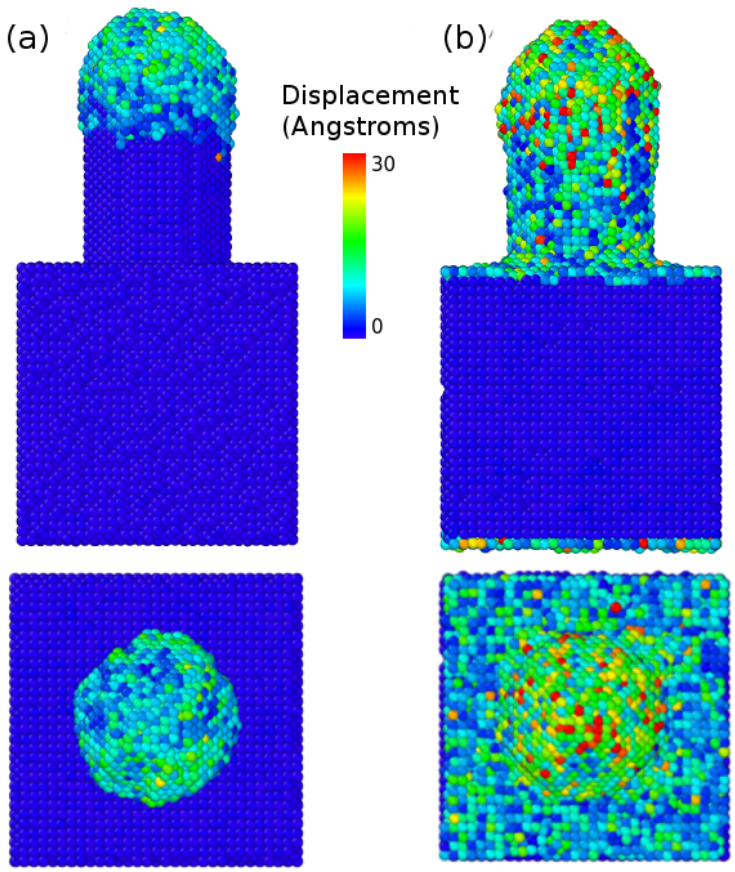

Figure 3.7: Atomistic snapshots of the tendril deformation, in which the color associated with the tungsten displacement at (a) 1200 K and (b) 2000 K the bottom image presents a top-down persepective. Blue atoms have not been displaced while red atoms have been displaced the most, at least 3.0 nm.

Table 3.1: Table of He/V values for helium bubbles within the tendril

Helium Concentrations		
Temperature (K)	Average He/V	He/V of Largest Bubble
1200	1.8±1.5	2.1
1500	1.5±1.0	2.0
1700	1.3±0.7	1.9
1800	1.2±0.9	1.5
1900	1.6±1.3	1.6
2000	1.1±0.6	1.3

helium clusters, the concentration tended to be closer to 2 He/V for temperatures less than 1800 K and about 1.5 He/V for 1800 K and above. This indicates that the bubble pressures are lower within a tendril compared to below initially atomistically flat surfaces. This may also be explained through the difference in surface to volume ratio. Because there is more surface area in the tendril volume, it is easier for helium to be released through the bubbles and therefore the resulting concentrations within the bubble are lower which can prevent the more damaging surface effects from subsurface bubbles.

Evaluating the Influence of Tendril Geometry

In addition to studying the effects of temperature, MD simulations were performed that varied both the tendril heights and radii. In each case, the different geometries are compared to the nominal height and radius used in the temperature comparison. In these simulations, the temperature was set at 1200 K. Results from the different heights will be discussed first. Heights of 4.8 nm and 8.0 nm were compared to the nominal height of 6.4 nm used in the initial simulations. Figure 3.8 (a) and (b) depicts the atomistic visualization for the 4.8 nm and 8.0 nm runs, respectively, while Fig 3.8c presents the plot of helium retention as a function of fluence. Results for the varying height are similar to the results for the 1200 K nominal case. As depicted earlier, fairly large helium bubbles have formed within the tendrils without any major deformation to the tendril surface. Most of the helium remains near the surface even in the case with the 8 nm tall tendril although two helium atoms have migrated to the base of the tendril. Both simulations actually look pretty similar despite the difference in tendril height. In fact, the helium retention data shown in Figure 3.8c indicates very similar behavior with the value for the helium retention of approximately 7% in each case. This indicates that the retention is independent of height in these small tendril simulations.

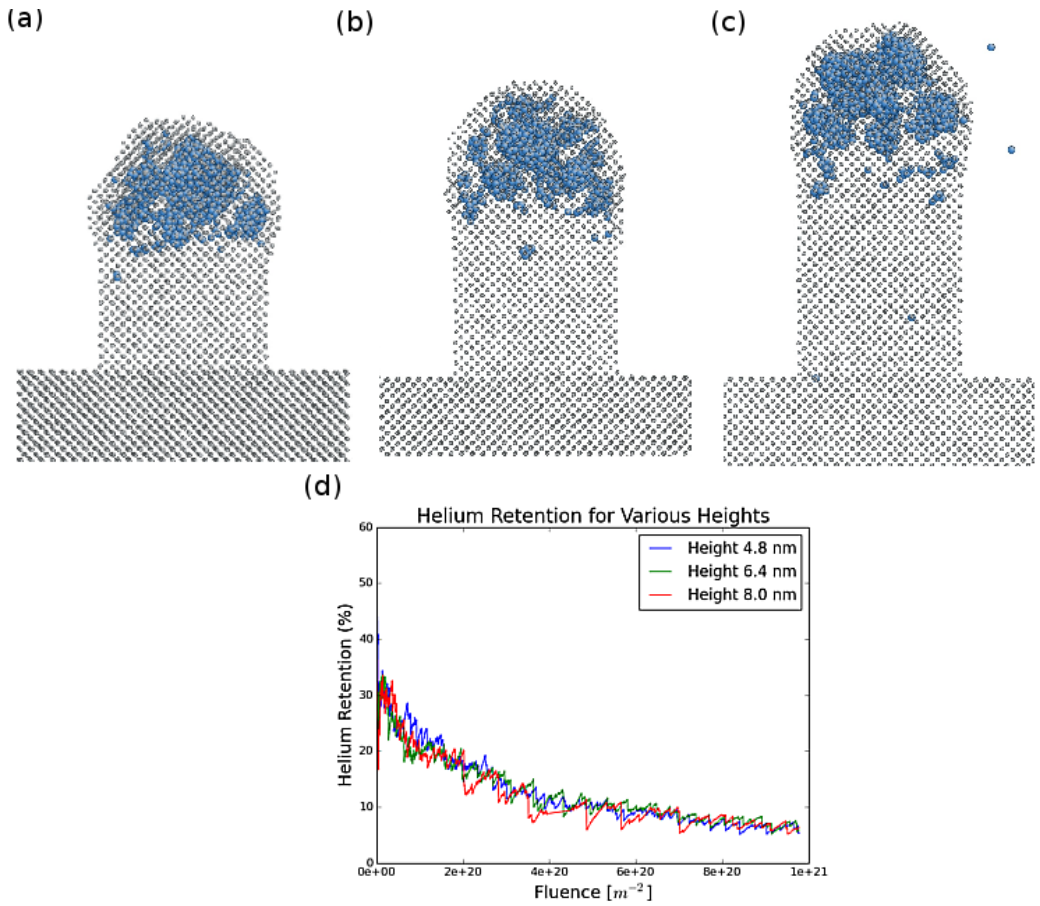

Figure 3.8: Atomistic snapshots of tendrils with varying heights of (a) 4.8 nm and (b) 8.0 nm. A plot of the helium retention in the tendril is show in (c). Gray and blue atoms depict tungsten and helium atoms respectively.

Results for the varying radii are discussed next. Two different radii of 1.3 nm and 3.8 nm were compared to the nominal case of 2.5 nm. The temperature was 1200 K. The visualization for the small and large tendril are shown in (a) and (b) of figure 3.9. For the radius of 1.3 nm, there is very little helium within the tendril, with only one large bubble observed at an implanted helium fluence of $10^{21}m^{-2}$. In contrast, the 3.8 nm radius tendril has a much larger inventory of helium and much wider distribution of varying bubble sizes residing within the tendril. This is further confirmed by the helium retention shown in figure 3.9(c). For 1.3 nm, the retenion is much lower, about 4% compared to the nominal case which is about 9%. The larger radii exhibits an even higher retention at the end of the simulation but this is not depicted in the graph because the retention is shown 3.9c as a function of fluence and not time. The maximum fluence shown here is $5x10^{20}m^{-2}$ because this is the highest fluence attained for the small 1.3 nm tendril after 20,000 helium insertions, or 20 ns of simulation time. The larger 3.8 radius tendril has not accumulated as much helium nor simulated as much time by a fluence of $5x10^{20}m^{-2}$ because of the larger surface area. If the retention were plotted as a function of helium insertions or simulated time, the 3.8 nm radius tendril would in fact have a higher retention, which is about 10%, as opposed to the nominal case which is the roughly 6% shown in the height comparison plot in figure 3.8(c). Therefore, the retention does depend on the radius of the tendril.

This difference in dependence between height and radius can also be explained by the surface to volume ratio of the tendril. With the different radii modeled, the volume of the tendril increases proportionally with r^3 while the surface area only increases as r^2. Therefore, the volume increases more than the surface area which allows for more ability within the tendril to store helium. Thus, the small 1.3 nm radius tendril has much less volume than the 3.8 nm radius tendril, leading to the varying retention based on radius. However, when the tendril height changes, the surface to volume ratio remains the same. Even though the taller tendril contains more volume in the z direction to contain helium, because the helium self-traps near the incident surface, the helium effectively does not diffuse within the larger volume and remains near the top of the tendril regardless. Therefore, the 8.0 nm tall tendril has a similar retention to the 4.8 nm tall tendril.

For most simulations, the helium remained near its implantation depth at the top of the tendril, as expected, due to self-trapping. Due to the high flux in these simulations, helium bubbles will form much more quickly than at lower fluxes, which does not allow enough time for the helium to diffuse deeper in the tendril. However, in a few cases, a helium atom or two has diffused down to the bottom of the tendril. This is an interesting note since these helium atoms are an outlier in the cumulative depth distribution. One of the questions this work seeks to address is the mechanism by which helium reaches the bottom of the nanotendrils. For the cases discussed in relation to Figures 3.3, simulations with higher temperatures are most likely to have

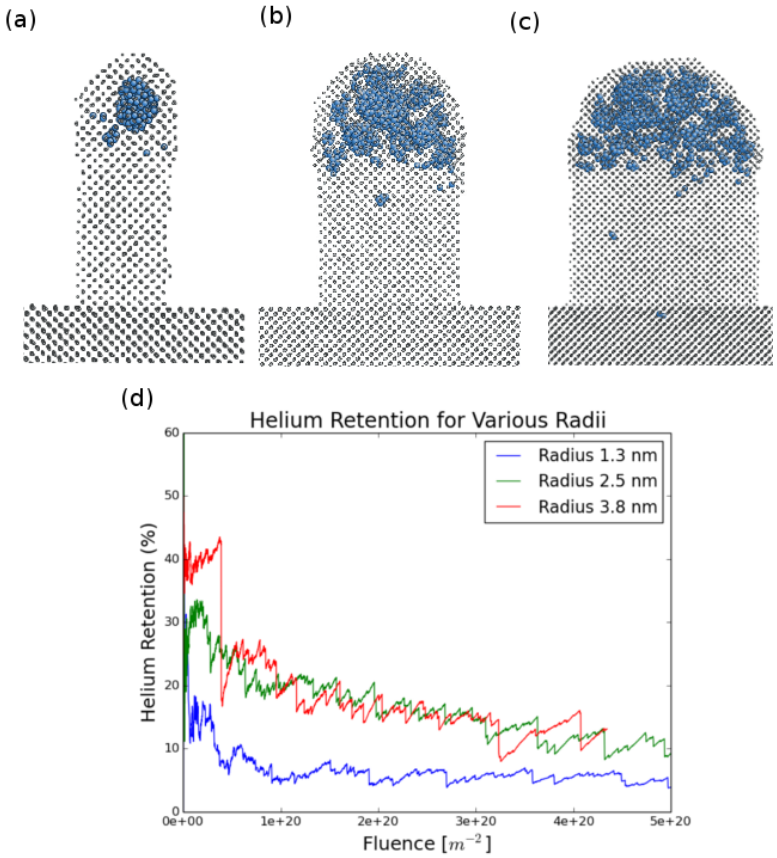

Figure 3.9: Atomistic snapshots of tendrils with varying radii of (a) 1.3 nm and (b) 3.8 nm. A plot of the helium retention in the tendril is show in (c). Gray and blue atoms depict tungsten and helium atoms respectively.

helium that migrates to the base of the tendril. In addition, the simulation with the largest tendril height also has helium that has diffused further into the tendril. However, these are limited observations with insufficient statistics and the helium atoms may or may not diffuse to the base of the tendril between simulations even at the same temperature. Another way to perturb the system to see the impact on helium diffusion would be to include an intial distribution of helium bubbles within the tendril to if the helium bubbles will limit diffusion to the bulk. It is possible that the stress in the matrix from pre-existing helium bubbles could bias diffusion towards the pre-existing bubbles and therefore modify the final helium depth distribution. Therefore, a serious of simulations were performed with initial bubble distributions, as described in figure 3.2, and the results are subsequently discussed.

Influence of Pre-existing Helium Bubbles

The first set of simulations with a pre-existing bubble distribution within the tendril include three different simulations with three small helium bubbles with a radius of 1.0 nm and a helium concentration of 1.2 He/V. These values were chosen in order for the bubbles to fit within the tendril itself with sufficient volume for helium to diffuse in the tendril and so that the bubble pressure was not so large that the bubble would greatly expand and distort the tendril at the beginning of the simulation, or immediately burst. For each of the three cases, a bubble was placed at depths of 1.5, 4.5, and 7.5 nm below the top of the tendril. The bubbles were either centred within the tendril, offset, or positioned to one side as shown in figure 3.2. Figure 3.10 presents atomistic snapshots of these simulations at 20 ns (helium fluence of $10^{21} m^{-2}$) where the images in (a), (b), and (c) depict the centered, offset, and co-linear off-center simulations respectively. For each of the cases, the helium atoms initially in the bubbles are not shown in order to better display the positions of the atoms that were subsequently implanted into the tendil. As seen in the atomistic snapshots, most of the helium atoms remain in the upper half of the tendril as previously discussed, except with a portion of the atoms segregating to the initial helium bubbles. One exception to this is the case where the helium atoms were placed co-linear off-center. For this simulation, there were a few atoms that did reach the bottom of the tendril despite the 1200 K temperature in these simulations. This is further quantified by the depth distribution plot in figure 3.10 (d), where the red line, which depicts the simulation with the bubbles co-linear off-center, exhibits the largest relative quantity of helium that has diffused past 3 nm. This could be due to the placement of the helium bubbles. When the bubbles are placed co-linear off-center, there is a large cross-sectional area for the helium atoms to reach deeper depths than for the two other cases. Another possible explanation is that since the bubbles are near one side of the tendril, the bubbles might be able to trap more helium atoms that are trying

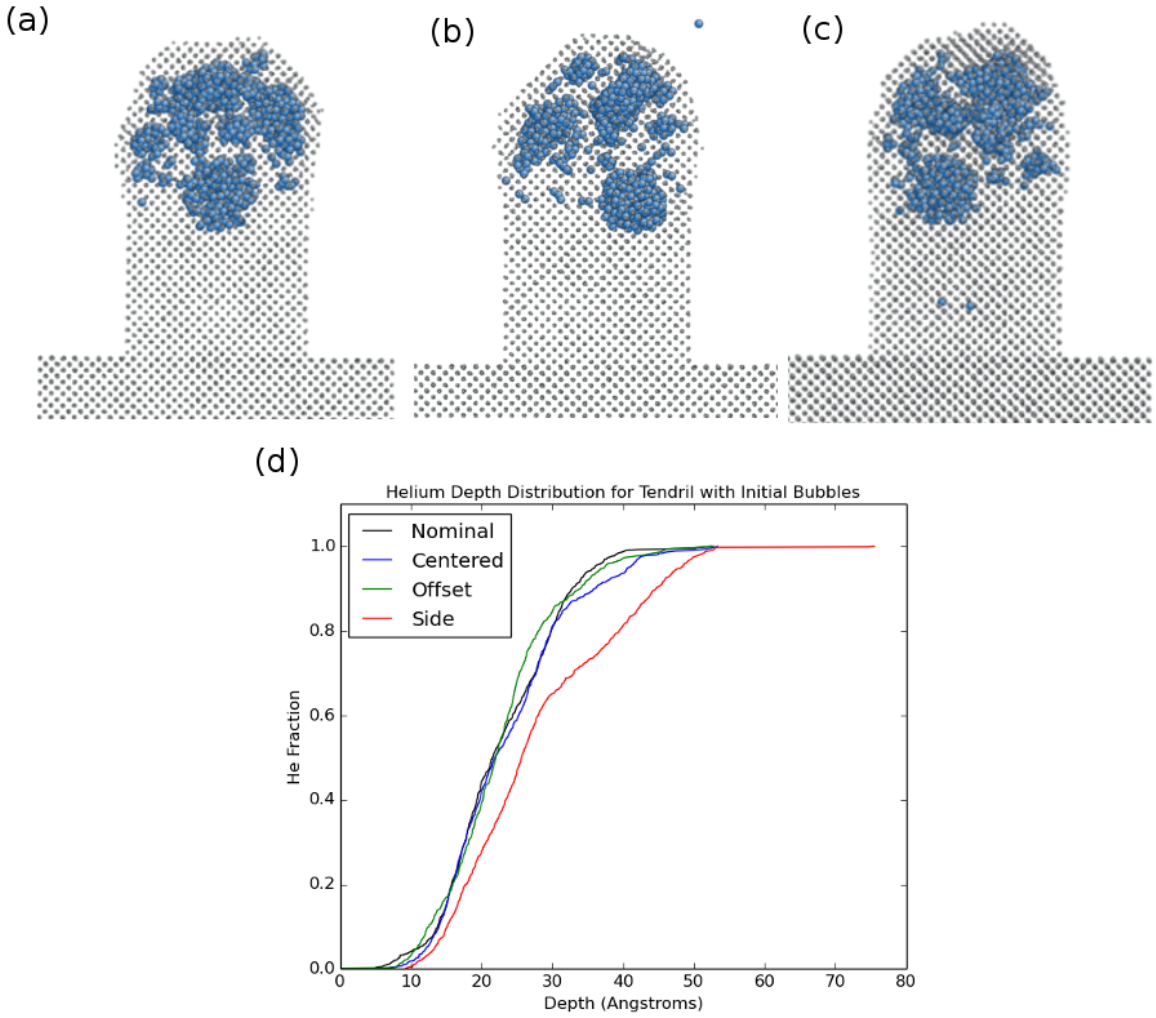

Figure 3.10: Atomistic snapshots of tendrils at 200 ns for initial bubble distributions that are (a) centered, (b) offset and (c) co-linear off-center based on the initial geometries in figure 3.2. Atoms initially in the bubbles are not shown here in order to depict strictly implanted helium atoms. A plot of the helium depth distributions for these cases and the nominal case at 1200 K are shown in (d).

Table 3.2: Helium Fluxes Down the Tendril and to Pre-existing Bubbles

Parameter	Centered	Offset	Co-linear Off-center
Flux past 4.5 nm ($m^{-2}s^{-}1$)	$2.2x10^{25}$	$3.0x10^{25}$	$2.1x10^{25}$
Flux past 6.7 nm ($m^{-2}s^{-1}$)	0	0	0
Flux to bubble at 1.5 nm ($m^{-2}s^{-1}$)	$3.8x10^{26}$	$1.8x10^{26}$	$2.4x10^{26}$
Bubble Δr	0.35	0.32	0.30
Flux to bubble at 4.0 nm ($m^{-2}s^{-1}$)	$2.1x10^{26}$	$2.6x10^{26}$	$2.0x10^{26}$
Bubble Δr	0.29	0.28	0.26
Flux to bubble at 7.5 nm ($m^{-2}s^{-1}$)	0	0	$2.2x10^{24}$
Bubble Δr	0	0	0

to escape the tendril, which might attract more of the helium atoms to diffuse deeper into the matrix.

From figure 3.10, it is clear to see that there is significant diffusion of helium to the pre-existing bubbles. To better quantify the amount of helium traveling down the tendril as well as to the pre-existing bubbles, the flux to each of these location was determined and listed in table 3.2. The fluxes past 4.5 nm (or 50% of the tendril) is fairly consistent for all three cases, being about $2-3x10^{25}m^{-2}s^{-1}$. However, the flux past 6.5 nm (or 75% of the tendril) is zero for all cases except the one with the bubbles positioned co-linear off-center, which has a lower flux of about $2.2x10^{24}m^{-2}s^{-1}$. This is an order of magnitude lower than the flux past 4.5 nm. As expected, the flux to the bubbles are much higher, typically about $1-3x10^{26}m^{-2}s^{-1}$ for the top two bubbles centered at 1.5 and 4.0 nm. For these bubbles, the additional helium atoms cause the bubbles to expand about 0.3 nm. Both of these values are consistent across the three different simulations. However, only the case with the bubbles to one side had a flux to the bottom bubble at 7.5 nm, with a value of that flux of $2.2x10^{24}m^{-2}s^{-1}$. In addition, the bottom bubbles did not expand due to the lack of or low helium helium flux to the base of the tendril.

Although most of the implanted helium remained in the top half of the tendril there was some limited diffusion to a bubble at a deeper depth. Therefore, the next step was to place one large bubble at the base of the tendril without any pre-existing bubbles near the surface that might easily trap implanted helium atoms. The bubble radius was increased to 1.5 nm and the bubble center was positioned at a depth of 7.5 nm. The helium concentration in the bubble for this set of simulations was only 0.5 He/V to ensure that the bubble would not significantly distort the lattice since it was placed near the base of the tendril. Simulations were performed at temperatures of both 1200 K and 2000 K. Figure 3.11 depicts the 1200 K simulation in (a) and the 2000 K simulation in (b) at a fluence of $10^{21}m^{-2}s^{-1}$. Again, the helium atoms initially in the bubble are not visualized here but the bubble sits at the base of the tendril. The inclusion of a larger, deeper bubble increased the amount of helium that migrated

down the tendril. This is especially true at 2000 K for which the helium has a higher diffusivity, the image in (b) shows a significantly larger number of helium atoms that have diffused this deep than previous perturbations. The depth distribution was again quantified and plotted in (c). The black line depicts the nominal case at 1200 K for comparison while the blue and green lines represent the 1200 K and 2000 K cases shown in (a) and (b). The green line representing the 2000 K case again confirms that there are less atoms at depths of about 3.0 nm and more atoms at depths greater than this.

The fluxes down the tendril are quantified for the two cases of one bubble at 1200 K and 2000 K. The flux past 4.5 nm was $3.2x10^{24}m^{-2}s^{-1}$ and $1.2x10^{25}m^{-2}s^{-1}$ for the 1200 K and 2000 K cases and the flux past 6.7 nm was $1.2x10^{24}m^{-2}s^{-1}$ and $9.4x10^{24}m^{-2}s^{-1}$ for the 1200 K and 2000 K cases respectively. Both of these cases display higher fluxes past depths of 6.7 nm than the previous simulations containing multiple bubbles, with the 2000 K case having the highest flux of any of the simulations. Both of the cases with one bubble had a lower concentration of helium in the bubble, only 0.5 He/V. Therefore, the bubble is initially underpressurized, causing the surrounding lattice to be in tension which could potentially drive helium atoms toward the bubble itself.

The flux as a function of time is tabulated for the cases with three bubbles that were either centered, offset, or co-linear off-center and for the cases with one bubble at the base of the tendril at both 1200 K and 2000 K. Figure 3.12 plots of flux past depths of 4.5 nm and 6.7 nm as a function of time, up to 200 ns, for all five cases. For all the cases, excepted the centered bubbles case, the flux initially increases then steadily begins to decrease at higher fluences. At depths past 6.7 nm, both of the one bubble cases show similar trends where the flux initially increases then slowly decreases indicating that the helium atoms diffused to this depth early in the simulation before helium bubbles that form near the top of the tendril could block further diffusion. For both depths, a line of best fit was drawn for all the data points. In both cases, a power law fit fairly well to the data and indicates a flux that is initially high and then slowly decays. While the MD simulation data available for this analysis is limited, if the line of best fit is extrapolated to 1 ms, the flux past 4.5 nm and 6.7 nm would be $1.0x10^{24}m^{-2}s^{-1}$ and $1.9x10^{19}m^{-2}s^{-1}$. These are both fairly low fluxes and the five orders of magnitude difference from just 4.5 to 6.7 nm indicates that at depths of 100-1000s of nm, the flux will be very low and most likely not large enough to form bubbles that could drive tendril growth.

Although it is hard to draw any concrete conclusions from the limited simulations described here, there is a clear trend of more helium atoms diffusing deeper into the bulk in the presence of initially placed helium bubbles, especially when there is a large bubble placed near the bottom of the tendril. The cases with initial bubbles that were not placed as deep did not have as great of an impact on the helium diffusion since

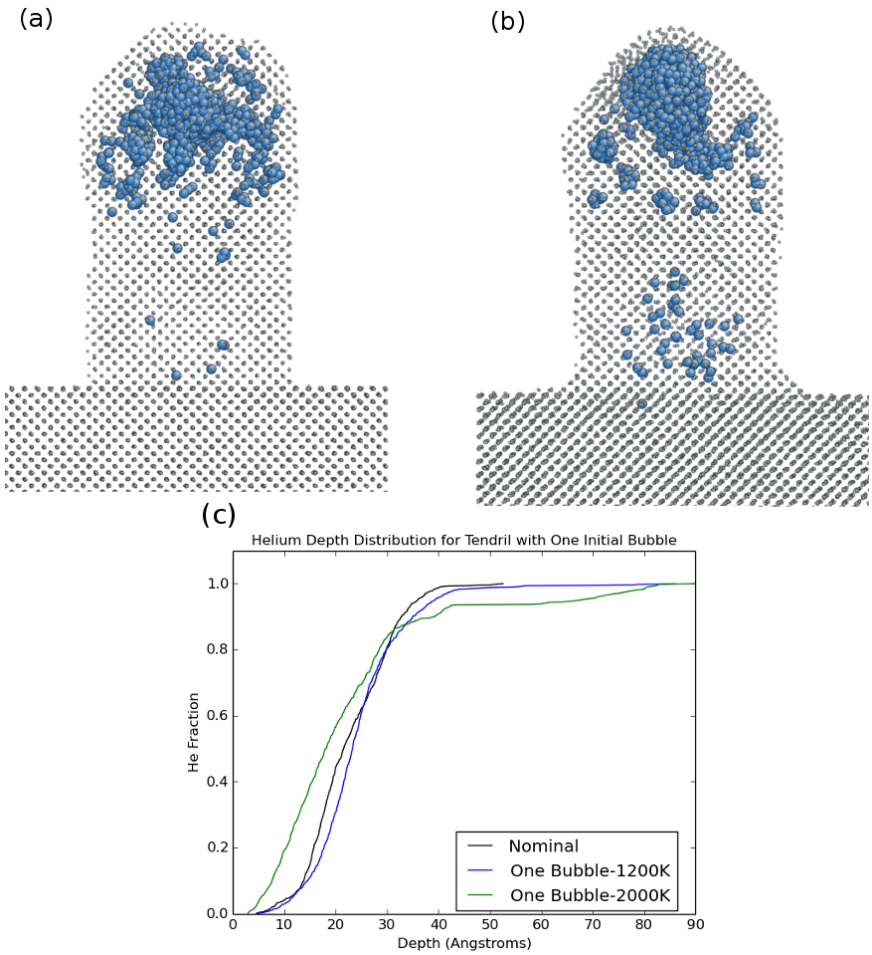

Figure 3.11: Atomistic snapshots of simulations with one initial helium bubble at the base of the tendril for temperatures of (a) 1200 K and (b) 2000 K at 200 ns. A plot of the helium depth distribution for these two simulations compared to the nominal case at 1200 K is shown in (c). Gray and blue atoms represent tungsten and helium atoms respectively. Helium atoms initially in the bubble are not shown here in order to better visualize the atoms that have migrated further into the tendril.

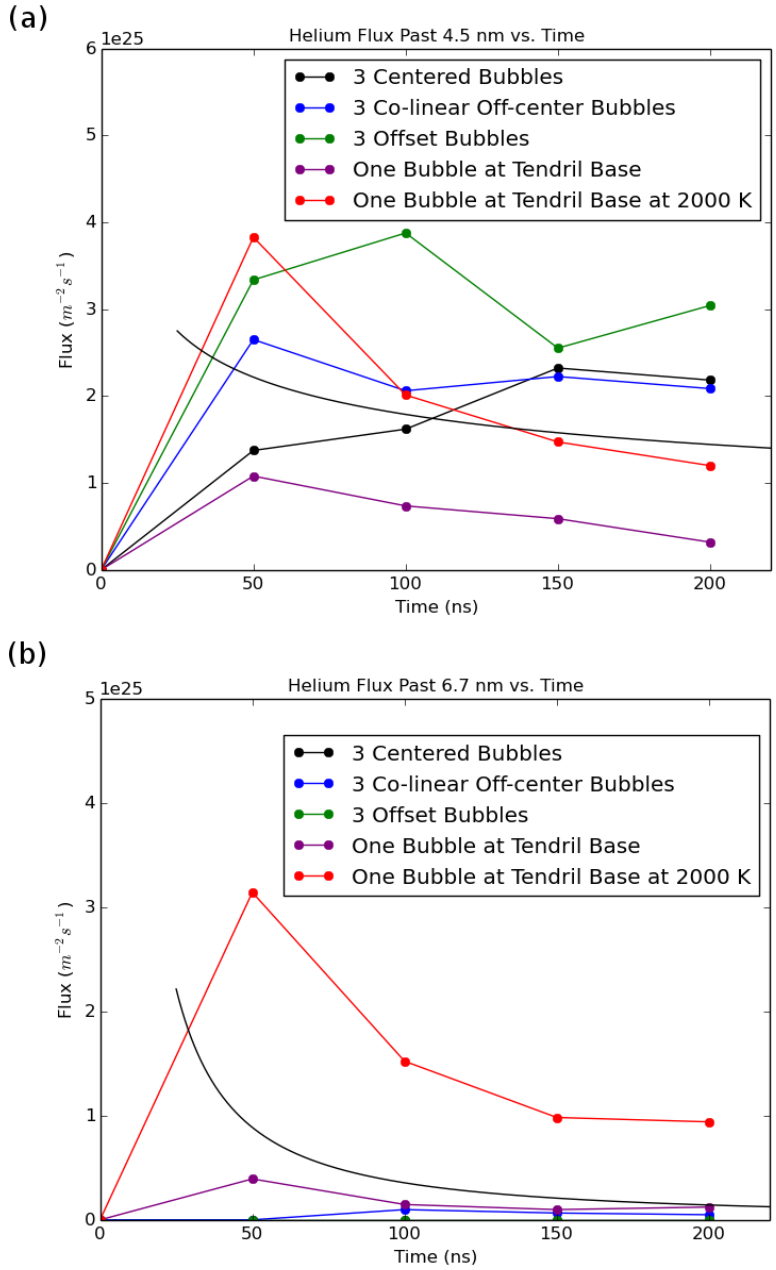

Figure 3.12: Fluxes of helium past (a) 4.5 nm and (b) 6.7 nm as a function of time up to 200 ns. Black, blue, green, purple, and red depict simulations with pre-existing helium bubbles including three centred bubbles, three co-linear off-center bubbles, three offset bubbles, one bubble at the tendril base, and one bubble at the tendril base at 2000K. A line of best fit is drawn in black for each case.

the bubbles near the surface will act as a sink for the implanted helium. The most diffusion past the mid-depth of the tendril was at 2000 K, but this is due to the higher mobility of the atoms at this temperature compared to 1200 K. Otherwise, for most cases, a flux on the order of $10^{25} m^{-2} s^{-1}$ diffused past 4.5 nm and a flux of $10^{24} m^{-2} s^{-1}$ diffused past 6.7 nm.

3.2.3 Summary

In this section, the results of simulations of helium implantation in a tendril-like geometry were described. The tendrils remain stable throughout the duration of the simlation regardless of the initial parameters. Large helium bubbles containing over 200 helium atoms form within the tendril, and are typically located near the top of the tendril close to where the helium was initial implanted. Evaluation of the helium retention indicates that at higher fluences, the continual accumulation of helium in bubbles and subsequent release leads to a steady-state of helium within the tendril. However, the larger surface to volume of the tendril allows the helium to escape without greatly deforming the tendril itself, allowing the tendril to remain a stable structure at these fluences. A modified bubble bursting process is observed where the bubble will create a pinhole rupture that releases a substantial amount of helium and later self-heals. The retention values at the end of the simulation are typically between 2 and 10%, with the retention decreasing at higher temperatures. While the bubble formation process is comparable with helium implantation in planar surfaces, the retention is not. At the high fluences of 10^{27} used here, the equivalent flux on planar surfaces results in much higher retention, typically around 60%[75]. The large amount of surface area around the tendril allows for helium to diffuse out of the tendril much more easily leading to lower retention. In addition, the helium bubbles, in general, have a He/V of 1-2 which is comparable to bubbles less than 1 nm below a planar surface but at depth of 3-4 nm or more below a planar surface, the He/V ratio is closer to 3-4. This implies that the helium bubble pressure is not quite as high for bubbles in the tendril which again is linked to the non-destructive release of helium due to the higher surface to volume ratio.

A variety of temperatures and geometries were modeled here. The retention has a weak dependence on temperature with a trend of lower retention at higher temperatures. As well, the size of the largest bubbles as well as the number of bubbles within the tendril are lower at higher temperatures. Tendrils with modified height and radii were also modeled. The tendril height did not have much of an effect on simulations results and visualizations of the resulting atomistic configurations were similar to the nominal case, as was the data on the helium retention. However, the radius did have an effect on the helium retention. Tendrils with larger radii have a

larger volume within the tendrils, compared to those with smaller radii, subequently leading to higher helium retention within the tendril at the end of the simulation.

Limited diffusion is initially observed at higher temperatures for the nominal case which prompted simulations that included pre-existing bubbles to study the influence of helium bubbles on diffusion. Bubbles placed near the surface act as a sink for implanted helium, with a helium flux of about $10^{26} m^{-2} s^{-1}$ and can block deeper diffusion of helium. However, there was more diffusion deeper into the tendril past 6.7 nm when the bubble was placed at the base of the tendril, with fluxes of $10^{24} m^{-2} s^{-1}$. Extrapolating the fluxes to depths past 6.7 nm to 1 ms yields a flux of $1.8x10^{19} m^{-2} s^{-1}$. This is a very low flux and this value will be even lower for tendril lengths on the order of 100-1000 nm indicating that it is unlikely that helium diffusion is driving tendril growth.

One of the limitations of this study is the high implantation flux of that the helium atoms. A higher flux means that the helium does not have enough time to diffuse deeper into the material before near surface helium bubbles begin to form, which then serves to block deeper helium diffusion. It will be important to study the effects that flux has on the retention and diffusion of helium in tendril-like geometries. Being able to extrapolate the results obtained here to fluxes on the order of $10^{22} m^{-2} s^{-1}$ will be crucial in being able to predict material performance. In addition, further investigation into the relationship between helium retention and surface to volume ratio will be needed in order to be able to predict the helium retention in tendril that are 100s of nanometers long.

3.3 Large Tendril-like Parallelepiped Geometry Modeling

Based on the observations of helium diffusion down the tendril-like geometry, this phenomena was investigated with a second set of simulations designed to focus more on diffusion. The initial small tendril geometry was modified to include a much longer tendril with a parallelepiped geometry to allow for an increased depth for helium to diffuse in the z direction. In addition, helium bubbles were added to one end of the tendril to complement the previous models that had initial helium bubbles present. Helium diffusion was studied in this modified geometry and is discussed in the following sections.

3.3.1 Methods

The geometry for the larger sized tendrils was modified by first removing the bulk region that was included in the small tendrils. This signigicantly reduces the computational time since diffusion in the tendril part of the simulation cell is of utmost interest. In addition, the tendril shape used was a parallelepiped as opposed to the cylindrical shape in the previous simulations. With the bulk removed, the tendril was extended to be 25 nm x 25 nm x 100 nm. At one end of the tendril, a series of 12 bubbles with a 1 nm radius and helium concentration of $3\frac{He}{V}$ were placed around the edge of the tendril at a depth of 2 nm. The initial geometry is shown in figure 3.13. Implantation of helium was performed on both ends of the tendril in order to study the effects of pre-existing helium bubbles on the diffusion of implanted helium atoms. Because of this, free surfaces were used in all three directions. To prevent the tungsten box from shifting during the simulation, it was necessary to fix the faces of the cell by prohibiting the center of mass of the face from moving. This ultimately prevents any unphysical motion during the simulation run.

Like previous simulations, the initial tungsten and helium bubbles were first initialized to 1200 K. Velocities from a Maxwell-Boltzmann distribution were used followed by velocity rescaling every 100 time steps and an NVE thermostat for 5 ps and then 15 ps without the velocity rescaling. Helium atoms were then implanted every 10 ps based on the SRIM depth distribution for 60 eV ions. The x and y coordinates were randomly chosen. In this case, helium was implanted from both ends of the tendril so that one atom was implanted on the end with bubbles, then 10 ps of simulation time was run, and then an atom was implanted on the end with no bubbles followed by 10 ps of simulation time. This was repeated until the desired simulation time was reached. Helium was implanted from both ends of the tendril in order to see the difference in helium diffusion based on the pre-existing helium bubble population. This amounted to a flux of $1.6x10^{26}m^{-2}s^{-1}$ A Nose-Hoover style NVT thermostat was used to maintain the temperature at 1200 K. Both (100) and (111) surface orientations were modeled and a temperature of 1200 K was used. A timestep of 0.5 fs was used throughout the simulation. The potentials used for this set of simulations were the same as those listed in section 3.2.1.

3.3.2 Results

The parallelepiped geometry simulations were simulated up to a fluence of $8x10^{18}m^{-2}s^{-1}$. Figure 3.14 shows an atomistic snapshot of the implanted helium for both the (100) and (111) surface and the ends of the parallelepiped with and without pre-existing helium bubbles. The purple, blue, and red atoms represent helium implanted on the side without bubbles, helium implanted at the side with bubbles, and helium

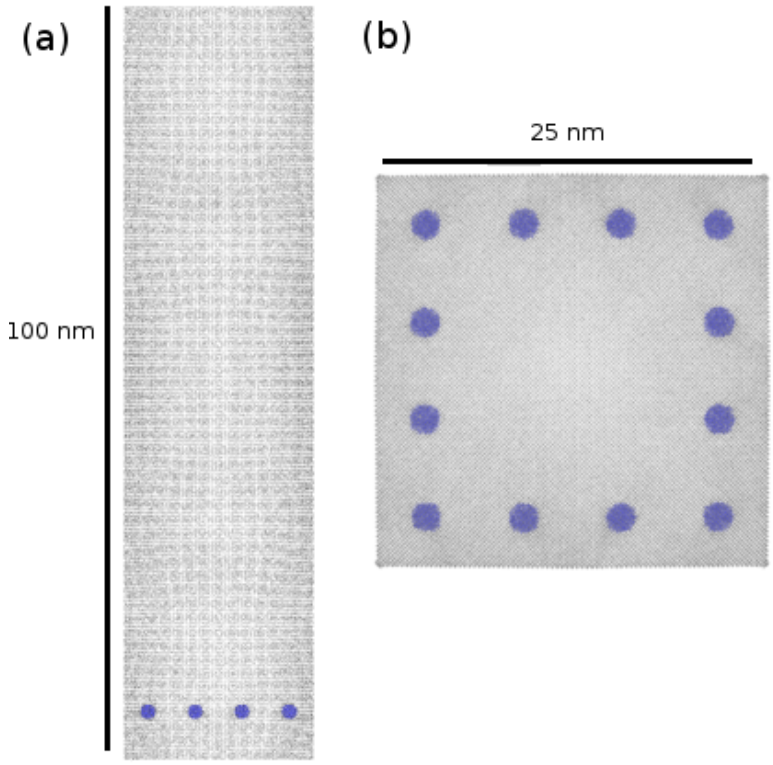

Figure 3.13: Initial geometry for the large parallelepiped simulations where (a) is a side view of the tendril and (b) is a top down view of the tendril.

initially in the pre-existing bubbles, respectively. The helium distributions at the end of the simulation are comparable between the two different cases for both ends of the parallelepiped. There is a thicker layer of helium between the surface and a depth of about 2 nm with some limited diffusion past this layer. A handful of single helium atoms are shown deeper into the material and some have even diffused down to the bubble layer. Compared to the small tendrils, there is not a lot of bubble growth since the fluence simulated is not large enough to start nucleating bubbles.

Figure 3.15 quantifies the helium depth distribution and there is some indication of limited diffusion into the material. About 5% or less of the helium has diffused passed 50 nm, which is a significantly larger depth than for the small tendril case, where the deepest helium only traveled about 7 nm. This is likely due to the lower flux which is approximately $10^{26} m^{-2} s^{-1}$ in this case, one order of magnitude lower than for the small tendril, as well as the reduced surface area for diffusion due to the cross-section with a length of 25 nm, as well as the longer geometry of 100 nm instead of 9 nm. However, there is no instance where the helium has diffused to the other end of the parallelepiped or even past the parallelepiped midpoint. The depth distribution does not greatly depend on either the surface orientation or the presence of bubbles since the distributions are all comparable with one another with slight differences. The cases for the (100) surface exhibit a slightly higher fraction of helium at shorter depths while the (111) surface case with pre-existing bubbles has helium that diffused past 10 nm, the deepest of all cases.

The flux of the helium past 3.5 nm, which is deeper than the layer of helium atoms at the surface, was quantified and is plotted in figure 3.16. For all cases, the fluxes are on the order of $10^{24} m^{-2} s^{-1}$ which is actually comparable with the fluxes past a depth of 6.7 nm, or 75% of the length of the small tendril presented previously in Table 3.2. For the (100) surface, the flux initially rapidly increases, but then seems to slowly increase, with the case without bubbles increasing at a faster rate then the case with pre-existing bubbles. For the (111) surface, the flux initially increases but then drops down and appears to remain steady. Three of the cases have a value of diffusional flux of about $1x10^{24} m^{-2} s^{-1}$ while the (100) case with no bubbles is about 3 times higher at $3x10^{24} m^{-2} s^{-1}$.

For the parallelepiped geometry, the helium retention increases significantly compared to the small tendrils. While the small tendrils exhibited helium retention between 3 and 10%, the helium retention for this parallelepiped geometry are 77%, 74%, 74%, and 75% for the (100) case with bubbles, the (100) case without bubbles, the (111) case with bubbles, and the (111) case without bubbles, respectively. There does not appear to be much of a dependence on either surface orientation or bubbles. Even with such a large surface area, the retention remains quite high. However, if the surface area to volume ratio is quantified, this result makes much more sense when compared with the small tendrils. A plot of the retention as a function of surface

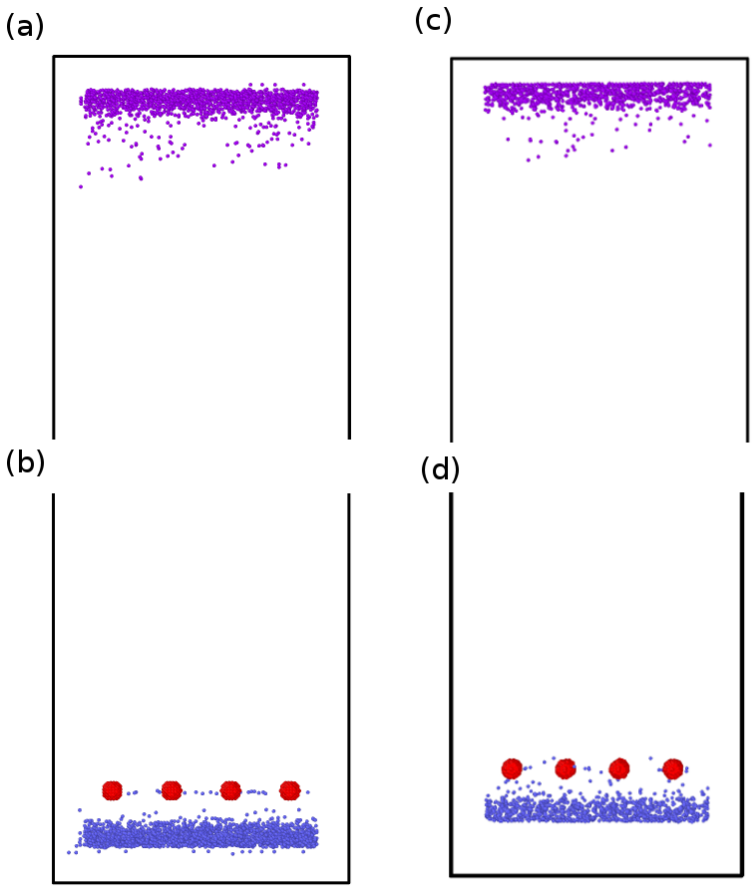

Figure 3.14: Atomistic snapshots for the parallelepiped simulations at a fluence of $8x10^{18}m^{-2}s^{-1}$ for the (100) surface (a) without and (b) with pre-existing bubbles and for the (111) surface (c) without and (d) with pre-existing bubbles. The purple, blue, and red atoms represent helium atoms that were implanted at the end without bubbles, at the end with bubbles, and initially in the pre-existing bubbles respectively.

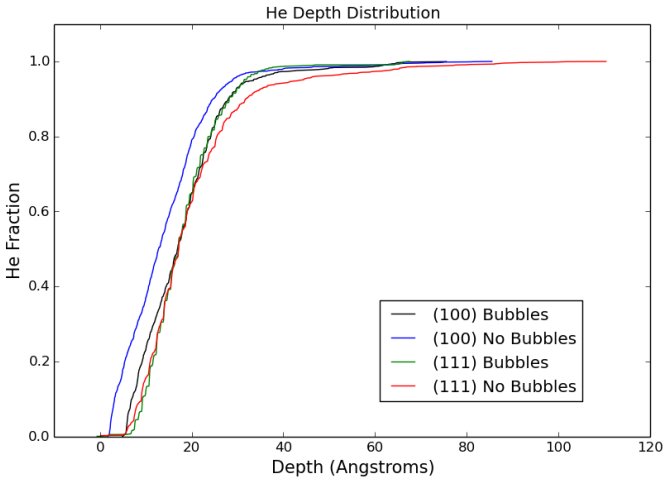

Figure 3.15: Depth distribution for the implanted helium atoms for the parallelepiped simulations. Black, blue, green, and red lines represent the (100) surface bubbles, (100) surface without bubbles, (111) surface with bubbles, and (111) surface without bubbles.

area to volume ratio is plotted in figure 3.17. The values for a (100) and a (111) planar surface are also plotted for reference and are represented by the red and blue stars respectively. While the surface area to volume ratio is quite high for the small tendrils, ranging from 2 to 9 depending on geometry, the ratio for the parallelepiped geometry is only 0.2. There is a clear dependence of the retention on the surface to volume ratio and power law fit appears to represent the data quite well. While the planar cases have an even smaller surface to volume ratio of 0.01, the retention is still slightly lower than for the parallelepiped geometry cases. However, the fluence of the planar cases is much higher than for the parallelepiped geometry, about an order of magnitude higher, and the retention for this case may start to decrease at a higher fluence as well.

3.3.3 Conclusions

Helium was implanted in a large tendril-like parallelepiped geometry with a length of 100 nm to a fluence of $8x10^{18}m^{-2}s^{-1}$. A layer of helium atoms is observed near the surface but there are no bubbles present since the fluence is not large enough for significant bubble nucleation and growth to larger (¿ 15-20 helium atom) sizes. There is some limited diffusion down the parallelepiped but no helium atoms have diffused past the halfway point of the parallelepiped, much less to the opposite end. However, the helium has diffused much deeper than for the small tendril cases, up to 10 nm deep, due to the lower flux for these simulations. The flux past a depth of 3.5 nm was

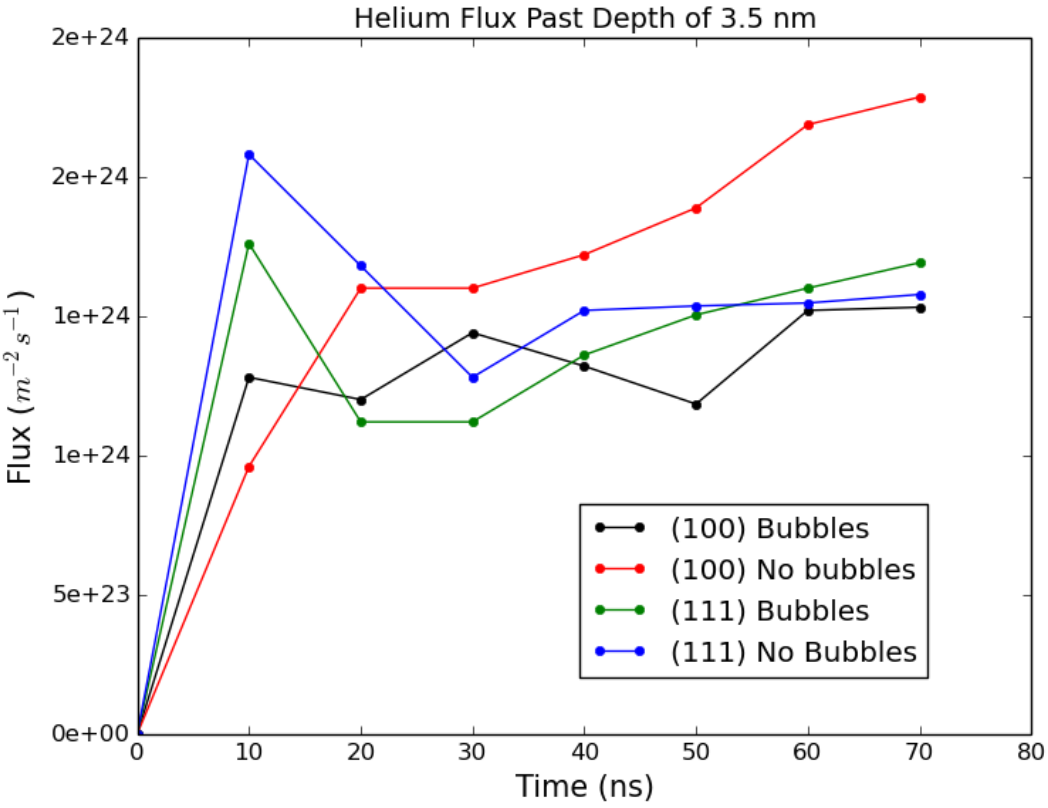

Figure 3.16: Flux of helium atoms past 3.5 nm for the parallelepiped simulations up to 70 ns. Black, red, green, and blue lines represent the (100) case with bubbles, the (100) case without bubbles, (111) case with bubbles and (111) case without bubbles.

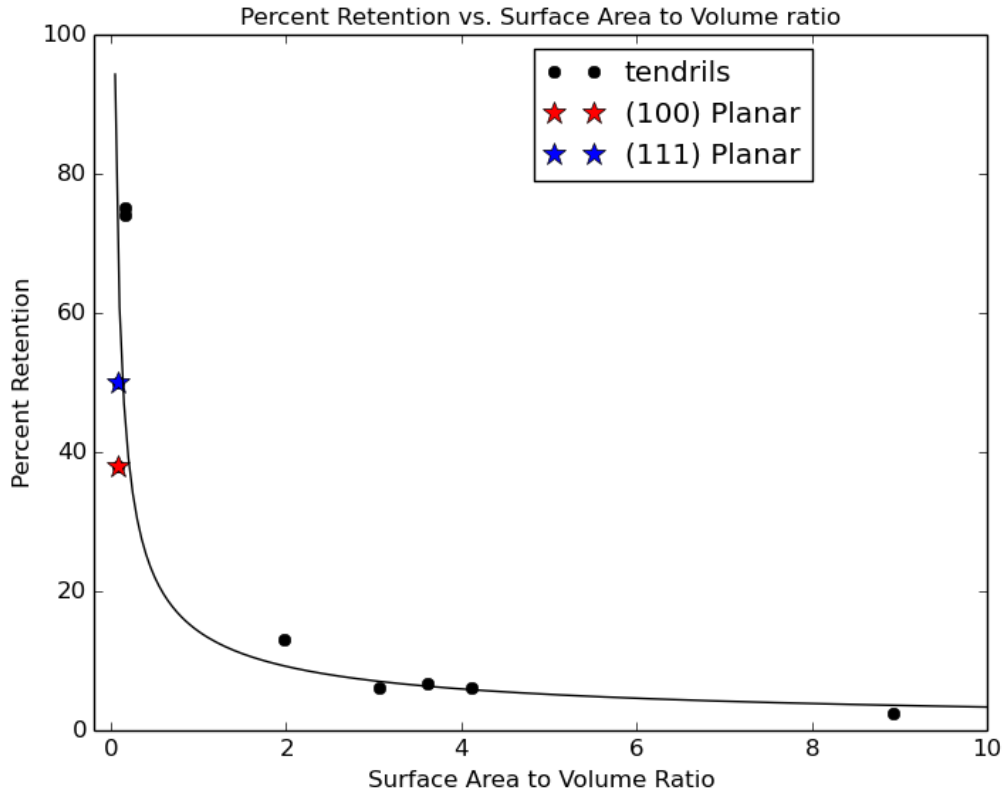

Figure 3.17: Helium retention as a surface to volume ratio for a variety of tendril geometries. The red and blue star represent retentions for planar cases with (100) and (111) surfaces respectively. A line of best fit is plotted, which is represented by a power law.

tabulated and the results are consistent across the different cases and have a similar flux with the small tendrils of $10^{24} m^{-2} s^{-1}$.

The retention as a function of surface to volume ratio was analyzed for all cases, including the different geometries for the small tendrils as well as a few planar surface cases. The retention drops with increasing surface to volume ratio and follows a power law trend. This explains the much higher retention of 75% for the parallelepiped geometry compared to the lower 3-10% for the small tendrils since the surface to volume ratio for the parallelepiped cases is about an order of magnitude lower than the small tendril cases.

The fluence for the parallelepiped cases is very low and these simulations would benefit with increasing simulation time. However, in the 70 ns that has been modeled, there is very limited diffusion here even at a lower flux and increasing the fluence will most likely limit the diffusion further since bubbles will start to form near the surface and block further helium diffusion. However, performing a similar simulation with an even lower flux would help in assessing the difference in absolute depth achieveable by the helium as a function of flux. This could help to predict and extrapolate the results to experimentally relevant scales.

3.4 Helium Implantation near a Grain Boundary

Pre-existing defects will affect the trapping and microstructural evolution in tungsten. Therefore, it is important to understand how underlying defects can influence the surface response. Grain boundaries have been shown to be strong trapping sites for helium[95]. To provide a benchmark for testing the continuum reaction-diffusion cluster dynamics code Xolotl, helium implantation near a $\Sigma 3$ grain boundary was performed. In these simulations, the helium was implanted strictly in an area that is not directly over the grain boundary in order to better study the accuracy of 2D diffusion of helium near defects in Xolotl.

3.4.1 Methods

For the W-He simulations, the goal is to model helium implantation in the presence of a grain boundary while only implanting helium in an area that does not include the grain boundary itself. These results will be available for future comparison to Xolotol in order to help benchmark the code. The same W-He potentials described in section 3.2.1 are used here. The simulation cell is 50 nm x 50 nm x 25 nm with periodic boundary conditions in the x and y directions and a free surface with a (111)

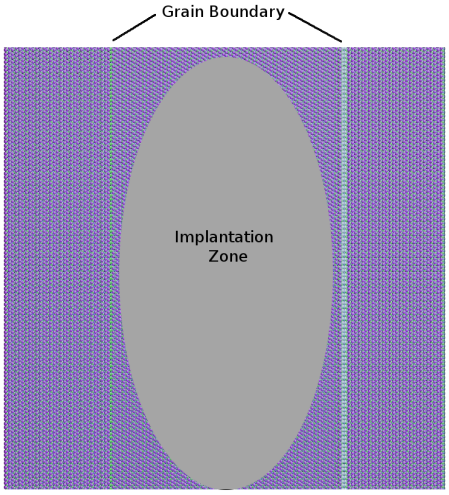

Figure 3.18: Initial geometry for simulation where helium is implanted near a grain boundary.

orientation in the z direction. Two $\sigma 3 < 111 > 121$ grain boundaries, where $< 111 >$ is the direction the grain is rotated around and 121 is the surface that the two grains meet at, were created at about 12.5 nm and 37.5 nm along the x direction. This divides the tungsten cell into three regions, where the middle part is kept stationary and the two outer parts are rotated around the $< 111 >$ direction until the planes facing the middle section meet at a (121) plane. The initial geometry can be seen in figure 3.18.

The tungsten is initialized to 933 K by giving the atoms a velocity based on the Maxwell Boltzmann distribution. Velocity rescaling was then performed every 100 timesteps for 5 ps and then turned off for 15 ps using a time step of 1 fs. After equilibrating the tungsten, helium atoms are inserted into an ellipetical section of the lattice that is strictly located between the two grain boundaries but not on the grain boundary itself, and amounts to about 40% of the total surface area. This implantation region is shown in figure 3.18. The helium implantation coordinates are randomly chosen in the x and y directions within the ellipse and sampled from the SRIM depth distribution for 60 eV atoms in the z direction. Time between insertions is 20 ps such that the nominal flux totals $4x10^{25}m^{-2}s^{-1}$. The procedure for helium insertion is as follows: first all the atoms in the system are frozen by setting their forces equal to zero, a helium atoms is placed at the desired coordinates and minimized, the rest of the atoms are unfrozen, and the simulation is then run for 20 ps. The atoms are initially frozen and only the helium allowed to move during the minimization in order to prevent overlap when inserting the helium which can lead to the introduction of large forces. The simulation is kept at 933 K using a Nose-Hoover thermostat. In

addition, the bottom layer of atoms are kept frozen in order to prevent the entire tungsten cell from moving in the z direction. This is done by fixing the center of mass of the bottom layer of tungsten atoms. This simulation was run for a total of 1 microsecond.

3.4.2 Results

The grain boundary simulation was run up to 1 μs. Snapshots are shown in figure 3.19 at times of 0.1, 0.5, and 1 μs. Only the helium atoms are shown in in order to better see exactly where the helium diffuses to. Within the implantation zone, there is a distribution of helium bubbles that is comparable to the observations from defect-free tungsten simulations. The middle region, where a majority of the atoms are being implanted, involves an essentially saturated layer of helium and large bubbles. Closer to the grain boundary, the amount of helium present quickly decreases and there actually seems to be less helium in the region next to the grain boundary compared to the grain boundary itself. At the grain boundary, there is some limited amount of helium that has mostly formed into small helium clusters. However, on the other side of either grain boundary, there is virtually no helium present, with only two helium atoms diffusing across the boundary during the entire microsecond run. This indicates the trapping strength of a grain boundary in that once the helium reaches the boundary, it does not diffuse further and remains there for the rest of the simulation.

The large bubbles below the surface create roughening at the surface and figure 3.20 displays a top-down view of this. The magenta adatoms represent the tungsten adatoms while the blue atoms represent helium. Within the implantation z one, there are a lot of displaced tungsten atoms and for this region, the snapshots are comparable to a simulation without pre-existing extended defects. Outside of the implantation zone, there are very few adatoms and most of the single magenta atoms shown are most likely due to thermal vibrations and not any sort of dislocation loop punching process. For a surface orientation of (111), the adatom shape on the surface have been previously shown to be a dome or cap above the exapnding bubbles[28]. This is also true in this simulation, there are a few domes above the array of bubbles and tungsten atoms have been displaced up to 1.3 nm above the surface. In addition, there are two holes on the surface indicating that over-pressurized bubbles were once underneath these holes and the pressure was high enough to expand and burst, leading to surface rupture and a large release of helium. Again, this has also been observed for simulations without defects[27] indicating that the behavior in the implantation zone is consistent with these defect-free simulations.

The next set of analysis investigates the helium concentration, depth distribution, and bubble distribution at different layers from the grain boundary. A small region

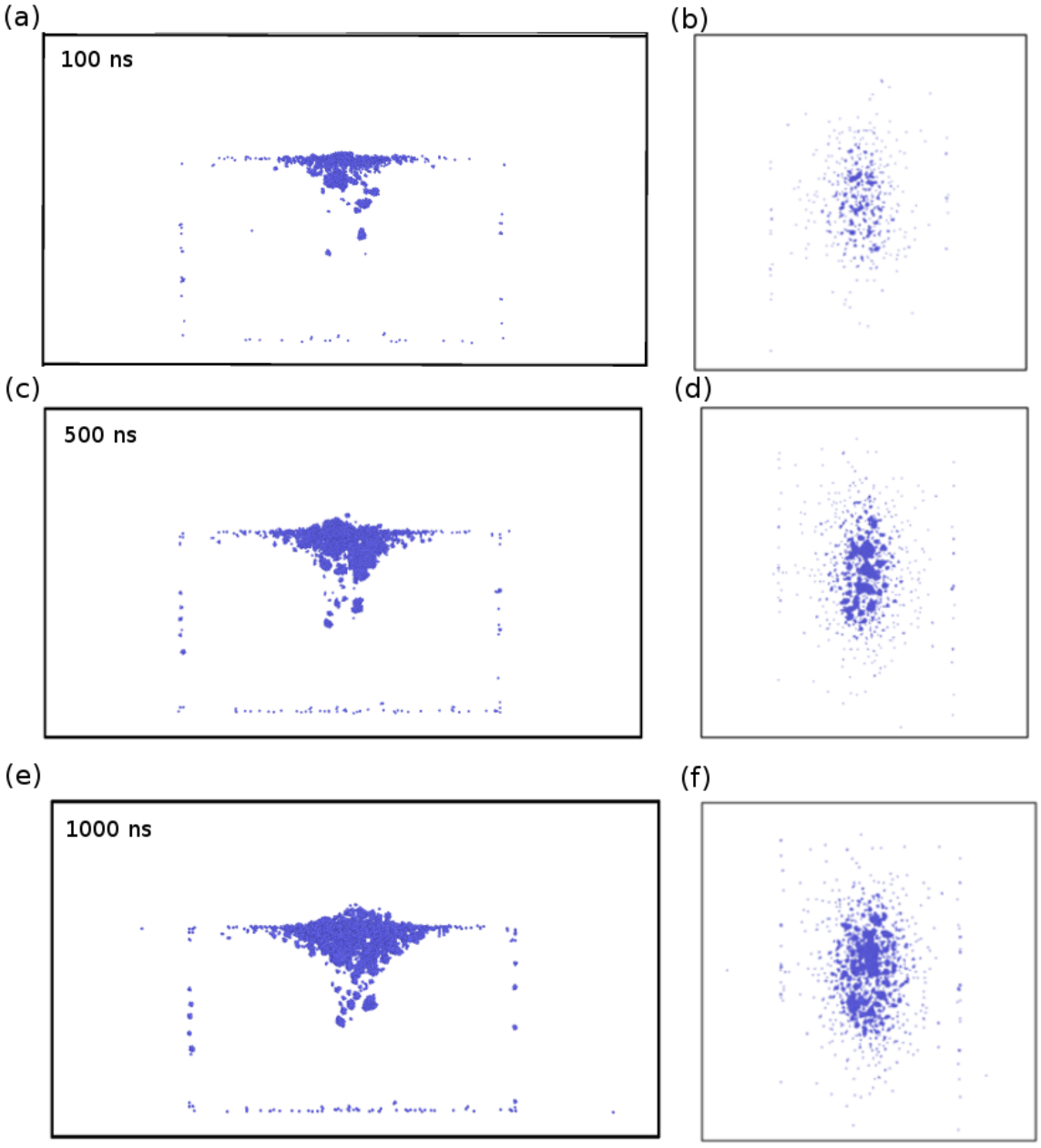

Figure 3.19: Snapshots for helium implantation near a grain boundary at 100 ns from a (a) side view and (b) top-down view, at 500 ns from a (c) side view and (d) top-down view, and at 1000 ns from a (e) side view and (f) top-down view.

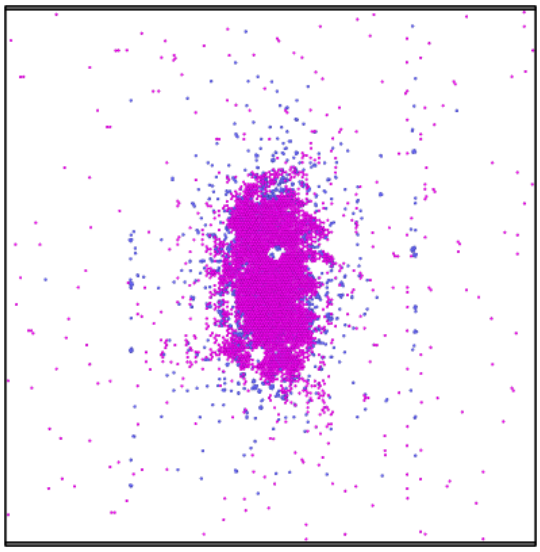

Figure 3.20: Tungsten surface deformation from helium implantation near a grain boundary from a top down view. The blue and magenta atoms represent helium and tungsten adatoms respectively.

of about 1.5 nm on either side of the grain boundary in the x-y plane is considered for the grain boundary region. The implantation area in between the grain boundaries is divided into 5 nm sections along the x axis and each 5 nm x 25 nm section in the x-y plane is analyzed for various quantities. This way, each quantity can be calculated for different distances from the grain boundary separately and compared. For the following plots, the right grain boundary is at an x position of 12 nm and the left grain boundary is at a position of 37 nm. The implantation zone is broken up into sections centered at 15, 20, 25, 30, and 35 nm.

The concentration is first calculated and plotted in figure 3.21. The results corroborate the visual snapshots, namely that the helium concentration is much higher in the middle of the implantation zone. At 25 nm, at the center of the implantation zone, the He/nm^2 is 23.7 while it is only 0.3 or 0.5 at the grain boundary at 12 nm and 37 nm respectively. The concentration quickly falls off as the distance from the grain boundary decreases. However, the concentration at the the first section next to the grain boundaries, at 15 nm and 35 nm, actually has a lower concentration than the grain boundary itself. Although it is hard to tell from the scale on the plot, the concentration at these sections is about 3 times lower than at the grain boundary, being only 0.1 at both 15 nm and 35 nm. This implies that there is a denuded zone around the grain boundary.

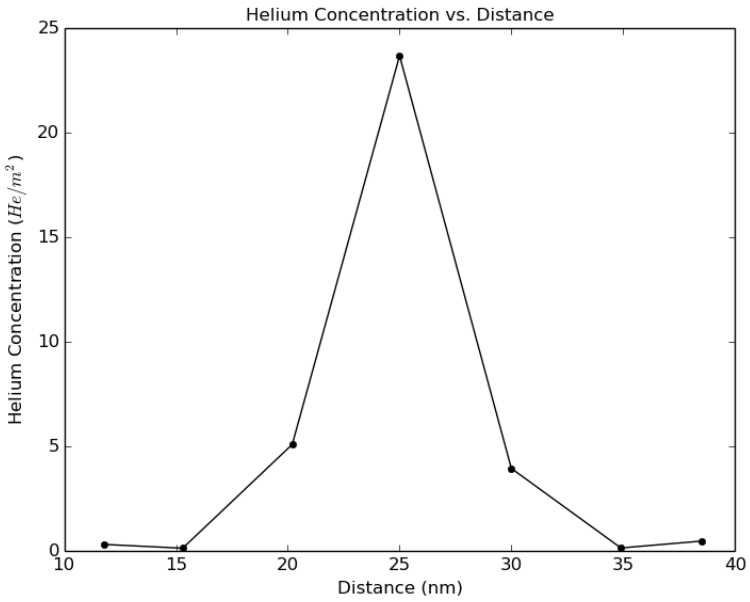

Figure 3.21: Concentration of helium in He/nm^2 at different distances from the grain boundary into the implantation zone. The concentration at each grain boundary at 12 nm and 37 nm is quantified. The implantation zone is sectioned into 5 nm slices and the concentraion is calculated at each point of 15 nm, 20 nm, 25 nm, 30 nm, and 35 nm.

The depth distribution for each section was quantified next. A plot for the spatially-dependent depth distributions is shown in figure 3.22 and does not include the helium that has diffused to the bottom of the simulation cell. The black, purple, green, cyan, magenta, orange, and blue lines represents the sections at 11 nm (GB), 15 nm, 20 nm, 25 nm (center), 30 nm, 35 nm, and 37 nm (GB). The depth distributions for the sections in the implantation zone are comparable for sections at the same distance from the grain boundary i.e. 15 nm and 35 nm which are right next to the grain boundary. Helium tends to diffuse deeper as the distance towards the center of the implantation zone decreases. For the section at the center of the implantation zone, there is a large portion, about 70% of the helium, within the first 2 nm but the rest of the helium has reached deeper depths of up to 8 nm compared to the more shallow depth distributions as the helium moves away from the center. As for the grain boundaries, the helium diffuses deep into the material as well, over 10 nm, and the depth distribution is fairly uniform past a depth of 2 nm. The curves are more jagged at the grain boundaries because there is less helium and the helium tends to form small clusters at the grain boundary which creates the jump in the cummulative helium depth distribution.

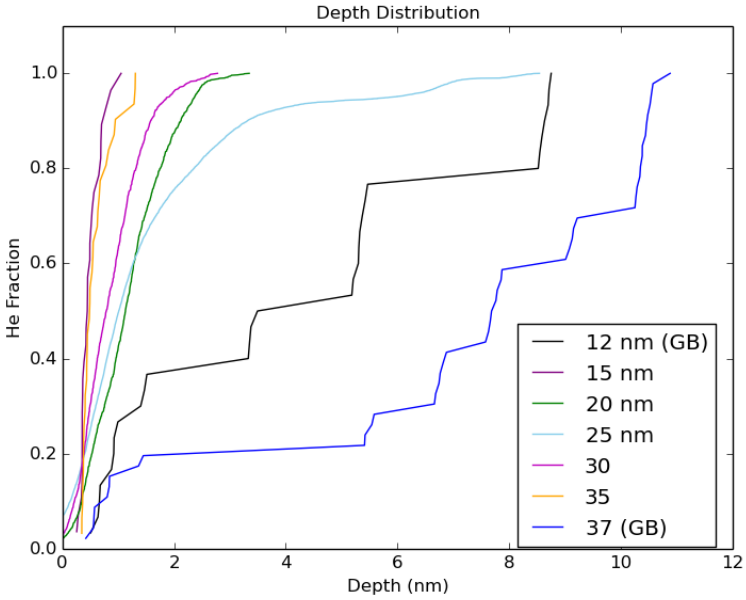

Figure 3.22: Depth distribution of helium at different distances from the grain boundary into the implantation zone. The distribution at each grain boundary at 12 nm and 37 nm is quantified and represented by the black and blue lines respectively. The implantation zone is sectioned into 5 nm slices and the depth distribution is calculated at each point of 15 nm, 20 nm, 25 nm, 30 nm, and 35 nm which are represented by the purple, green, light blue, magenta and orange lines .

The distribution of helium bubbles is also quantified for each spatially resolved region. Figure 3.23 shows the perecent of the helium in clusters of size 1, 2-9, 10-19, 20-49, 50-599, and 100+, which are represented by purple, blue, light blue, green, light green, and yellow, respectively, within each spatial region. As expected, the center of the implantation zone has a majority of the helium bubbles in large clusters of over 100 atoms in size. An array of small to medium sized clusters is also observed within the middle of the implantation zone. At the grain boundaries, most of the helium has formed small clusters with dominant size in the range of 2-9 helium atoms, along with a few clusters of size 10-19. Typically less than 20% of the helium at the grain boundary is in the form of a single helium atom. In contrast, the spatial regions next to the grain boundary have most of the helium as single interstitial atoms with a minority of helium in clusters of size 2-9.

The helium concentration, depth distribution, and bubble distribution in the implanted zone are fairly consistent to results without a pre-existing defect. However, this behavior differs at the grain boundary itself and the region outside of the implantation zone on the other side of the grain boundaries. Clearly the grain boundary has essentially blocked the helium that have reached the grain boundary

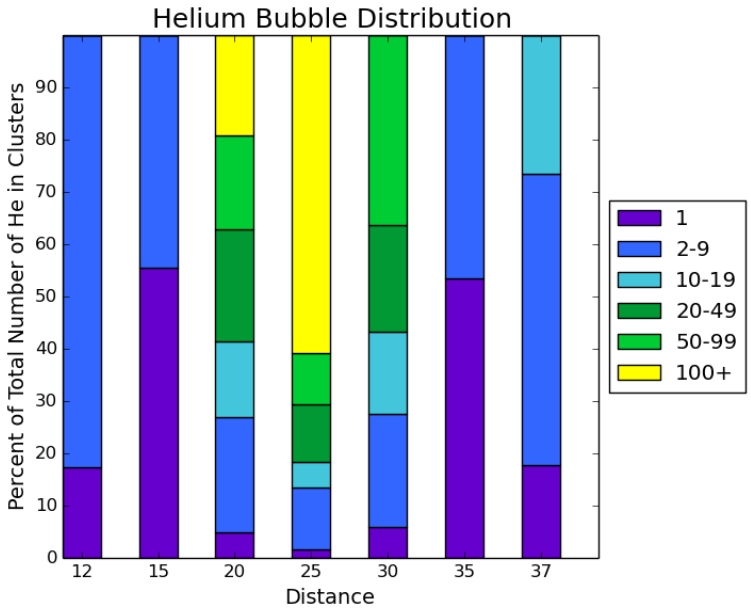

Figure 3.23: Distribution of helium bubbles at different distances from the grain boundary into the implantation zone. The distribution at each grain boundary at 12 nm and 37 nm is quantified while the implantation zone is sectioned into 5 nm slices centered at 15 nm, 20 nm, 25 nm, 30 nm, and 35 nm. Cluster sizes of 1, 2-9, 10-19, 20-49, 50-99, and 100+ are represented by purple, blue, light blue, green, light green, and yellow.

from crossing over to the other side of the boundary where no helium was being implanted. However, the amount of heluim that has diffused to the grain boundary is fairly limited, as indicated by the low concetration at either grain boundary. Therefore, the flux of helium to the grain boundary is quantified as shown in figure 3.24. The blue and red lines represent the grain boundary at 12.5 nm and 37.5 nm respectively. Initially, the flux is about $2x10^{24}m^{-2}s^{-1}$, which is about an order of magnitude lower than the implantation flux. However, the flux steadily decreases throughout the simulation and eventually falls off to about $3x10^{23}m^{-2}s^{-1}$. This indicates that the helium diffuses towards the grain boundary at the beginning of the simulation, when the fluence is still low and helium bubbles have not yet started accumulating in the implantation zone. Once a distribution of bubbles has formed, they also act as a sink for helium and can block diffusion. The sink strengths for a grain boundary and helium bubble was calculated using sink strengths from cluster dynamics. The sink strength for a grain boundary is defined as:

$$S_{GB} = \frac{60}{d^2} \tag{3.1}$$

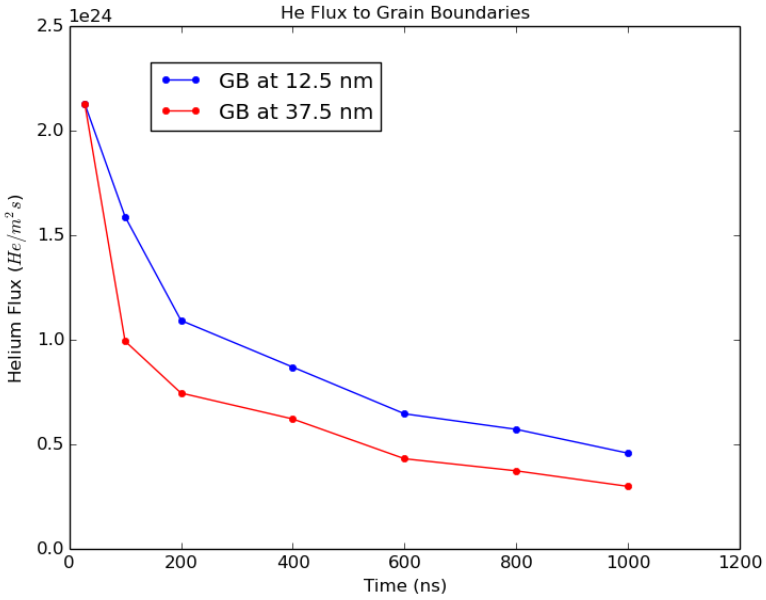

Figure 3.24: Flux to the grain boundary as a function of time for the grain boundary at 12 nm and 37 nm, represented by blue and red respectively.

where d is the diameter of the grain boundary. The sink strength for a cavity is defined as:

$$S_{cavity} = 4\pi r_c N_{cav} \tag{3.2}$$

where r_c is the capture radius and N_{cav} is the number density of the cavities. With a value of 25 nm for d, the grain boundary sink strength is 0.096 nm^{-2}. With a value of 0.0532 nm for r_c and a value of 0.013 $cavities/nm^3$ for N_{cav} at the end of the simulation, the bubble sink strength is 0.089 nm^{-2}. The values between S_{GB} and S_{cavity} are very similar indicating that by the end of the simulation, the sink strengths are essentially equal between the two defects. However, at the beginning of the simulation before bubbles start to form, the cavity sink strength will be much smaller than the grain boundary sink strength and therefore the grain boundary will be a greater sink early in the simulation. As bubbles start to nucleate, the importance of the grain boundary as a sink will start to decrease.

3.4.3 Conclusions

A simulation with a $\Sigma 3 < 111 > 121$ grain boundary where helium was implanted in an area that did not include the grain boundary itself was performed. The observed behavior away from the grain boundaries, including helium bubble formation and retention, evolved similarly to previous MD simulations of helium implantation in

large-scale simulations without a grain boundary. There is some limited helium diffusion to the grain boundary where the helium is trapped. However the concentration is much lower on the boundaries, with only 0.3 or 0.5 He/nm^2 as opposed to 23 He/nm^2 at the center of the implantation zone. The depth and bubble distributions in the implantation zone are also comparable to simulations without grain boundaries. At the grain boundary, the helium tended to diffuse deeper and mostly consisted of helium clusters of size 2-9.

The helium flux to the grain boundary was also evaluated. Initially, the value is about $2x10^{24}m^{-2}s^{-1}$ but quickly decreases to a value of $3x10^{23}m^{-2}s^{-1}$ over time and the trend appears to decrease towards a saturation value less than$0.5x10^{24}m^{-2}s^{-1}$. Clearly the helium mainly diffuses to the grain boundary at the beginning of the simulation when the grain boundary sink strength dominates the cavity sink strength before helium bubbles have formed. By the end of the simulation, the cavity sink strength is on par with the grain boundary sink strength, being 0.089 and 0.096 nm^{-2} respectively.

The data accumulated from this simulation will be useful in benchmarking the continuum reaction-diffusion cluster dynamics code Xolotl, especially in regards to the 2D diffusion of helium near defects. A similar simulation will need to be performed in Xolotl and the same properties calculated here can be peformed for the results from Xolotl. Comparing the results between MD and Xolotl will provide confidence in the newer code in extrapolating the results to experimentally relevant time and length scales.

Chapter 4

Modeling of Low-Energy Hydrogen and Mixed Hydrogen-Helium Implantation into Tungsten

4.1 Motivation

Previous chapters have focused on describing the results of MD simulations of pure helium implantation in tungsten. However, a divertor will be subject to high level implantation fluxes (on the order of $10^{24} m^{-2} s^{-1}$) during steady state operation of both hydrogen and helium atoms at concentrations of approximately 90% and 10%, respectively. Therefore, in this chapter, the results of MD simulatios of the implantation of mixed hydrogen-helium implantation into tungsten to investigate behavior more consistent of expected conditions in the ITER tungsten divertor. In experiments, it has been shown that the presence of helium modifies the surface response of tungsten compared to cases where just hydrogen is present[17]. In the case of pure hydrogen plasmas, micron sized blisters tend to form on the tungsten surface indicating that there could be a large inventory of hydrogen beneath the surface[59][17]. This rasises concerns for hydrogen retention within the divertor. However, in mixed hydrogen-helium plasmas the typical hydrogen blisters are supressed even at helium concentrations as low as 0.5%[17]. This indicates that there is some interaction or modification based on inclusion of helium in the plasma. The experiments were conducted in a plasma regime where the typcial helium bubble layer below the surface will form. It is possible that the helium bubbles just below the tungsten surface alters the diffusion path of hydrogen by blocking the hydrogen from migrating deeper into the bulk to form the large bubbles that lead to blistering.

However, the details of the interaction between hydrogen and helium responsible for the modified depth distribution is still unknown.

Molecular dynamics is well suited to study such interactions between the two different gas atom species. In this chapter both small and large scale simulation results are described for both pure hydrogen and mixed hydrogen-helium plasmas. The first section describes a series of simulations on small mixed hydrogen-helium subsurface bubbles. Subequent sections involve larger simulation cells used to model the implantation behavior of pure hydrogen and mixed hydrogen-helium below initially flat tungsten surfaces as well as hydorgen implantation below a tungsten surface that had been pre-implanted with helium to develop a helium bubble layers and corresponding durface roughness. These simulations seek to understand the synergestic behavior of hydrogen and helium and to provide a mechanism to explain the observed experimental behavior.

4.2 Modeling of Mixed Hydrogen-Helium Subsurface Bubbles

The simulations described involve small subsurface bubbles initially populated with various concentrations of both hydrogen and helium atoms evoloved by MD for times from 100 ps to 10 ns to asses hydrogen diffusion and partitioning around the helium bubble. Previous simulations by Juslin and Wirth [71] in bulk showed that after 100 ps at 900 K, the hydrogen in the bubble segregated to the bubble periphery after it was initially placed randomly within the the helium bubble. If hydrogen does segregate to the bubble periphery, it will be important to confirm this behavior and quantify the binding energy of hydrogen to the bubble to better understand the impact on hydrogen retention within the divertor. The simulations in this section seek to expand the results found in Juslin's work by including the presence of a free surface, to oberve if the hydrogen remains in the helium bubble periphery.

4.2.1 Methods

The molecular dynamics code LAMMPS was used for this set of simulations. A different set of potentials from the pure helium cases was used to accomadate for the more complex tungsten-hydrogen interactions. The W-H Tersoff [87] potential developed by Juslin[88] et al and modified by Guterl[92] et al was used. For W-He and He-He, the same potentials from previous chapters were used, namely the Juslin and Wirth [82] and Beck potential[83] modified by Morishita et al. [84] respectively.

A simple Lennard-Jones potential developed by Delashenko[86] was used for the He-H interactions.

For this set of simulations, a tungsten box that is 6 nm x 6 nm x 6 nm in size was used with periodic boundary conditions in the x and y directions and a free surface in the z direction. In order to preserve the free surface conditions in the z direction, it is necessary to include vacuum space both above and below the tungsten cell. For this set of simulations, about 3 nm of void space was used. With the inclusion of this free space, it is necessary to fix the bottom few layers in order to prevent the tungsten slab from shifting within the simulation cell. This was done by fixing the center of mass of the bottom layer of atoms, which allows the atoms to move but constrains the layer itself from shifting. The tungsten was first equilibrated to the appropriate temperature by selecting velocities from a Maxwell-Boltzmann distribution and run for 10 ps with both veclocity rescaling every 100 time steps and an NVE thermostat with a time step of 1 fs. The simulation then evolved for 10 ps with no velocity rescaling. This procedure was performed at the beginning of each simulation to make sure the tungsten was at the appropriate temperature before inserting gas atoms.

To create the subsurface bubble, a spherical void was carved out of the tungsten. The center of the sphere was 3 nm below the free surface and centered in the box in the x and y directions with a radius of 1 nm. A bubble depth of 3 nm was chosen to prevent surface rupture after implanting the high gas concentrations that will be studied in the work. Since the bubbles were placed a few layers underneath the surface instead of right at the surface, the bubble should expand through loop punching, which is a much less destructive interaction with the surface. The void was then randomly populated with hydrogen concentrations of either 0.5 or 1 H/V and helium concentrations of 3, 3.5, or 4 He/V. An example of the initial geometry of the simulation is shown in figure 4.1 with the blue, green, and gray atoms representing helium, hydrogen, and tungsten at the top and bottom surfaces respectively. An inset image seen in the box shows a slice through the middle of the bubble and emphasizes the initial random distribution of the hydrogen and helium within the helium bubble. The energy was first minimized to ensure that there were no overlapping gas atoms, which would introduce unrelastically large forces at the start of the simulation which can lead to unphysical behavior. Simulations were then run for 100 ps with a time step of 0.1 fs to assess hydrogen diffusion and final positions as well as bubble evolution. Temperatures of 1200, 1500, 1800, and 2000 K were modeled and the temperature was kept constant using an NVT thermostat during the 100 ps run. Two different surface orientations, (110) and (111), were modeled. For each combination of parameters, five independent simulations were performed with different random numbers to provide statistics. The set of simulations presented here will be denoted as the nominal cases in further discussion in the results section.

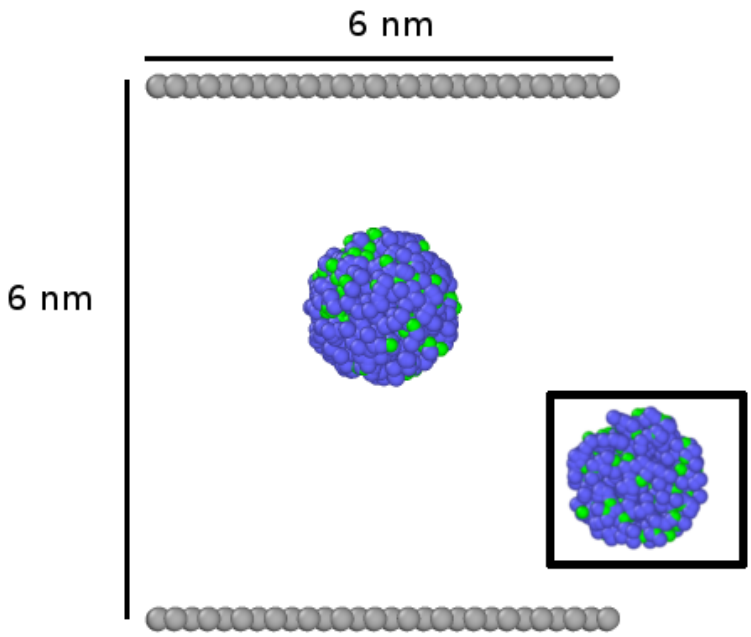

Figure 4.1: Atomistic snapshot of the typical initial configuration for the mixed hydrogen-helium bubble simulations. Blue, green, and gray atoms represent the helium, hydrogen and tungsten atoms at the top and bottom surfaces respectively. The inset image in the box is a slice through the middle of the bubble.

Additional parameter variations were performed to assess the impact of the initial simulation setup on the final results obtained. The first perturbation was to modify the intial placement of the hydrogen to see if diffusion in the vincinity of the helium bubble was biased by initially placing all the hydrogen within the bubble. In this modified simulation, hydrogen was instead initially placed throughout the entire simulation cell. Another parameter that was additionally modifed was the geometry in order to study the effect of system size on the results obtained with the nominal case. The directions in the x and y directions was first doubled from 6 nm to 12 nm while the bubble was still centered in the box and at the same depth of 3 nm. Because of the periodic boundary conditions, the length in the x and y directions will affect the strain field interactions due to the distance to the corresponding bubble in the periodic image. Modifiying the length in these directions effectively changes the distance between the bubbles across the periodic boundaries. The length in the z direction was also increased from 6 nm to 12 nm in a seperate simulation. Due to the deeper box, the bubble was also moved from 3 nm to 6 nm below the surface. This modification will help to better understand the effect of the surface on the bubble evolution. Finally, select simulations were extended past 100 ps to understand how the initially short simulation time may affect the results.

4.2.2 Results

First, the general bubble evolution is described. As discussed in section 1.4, helium bubbles, when overpressurized, typically expand through dislocation loop punching. This is also true for the simulation results described in this section. With the high initial gas concentrations in the bubble, it is observed that the bubble expands and creates adatoms at the surface, indicating that the bubbles are expanding through trap mutation and loop punching. Since the bubble is initially 3 nm below the surface, the punched out loops eventually annihilate at the surface to form adatom islands. A few examples of this are shown in figure 4.2, with the magenta adatoms denoting the adatom structures that form at the surface. This is consistent with previous MD simulations that also observed loop punching bubble expansion process for pure helium bubbles [28]. The behavior between the (111) and (110) surface is also consistent with previous MD results. For the (111) surface, the adatoms tend to form a dome or hemisphere directly above the bubble. The bubble will also preferentially expand towards the surface. Since the preferred loop punching direction is $< 111 >$, the dislocation loops move directly towards the surface forming the caps shown in figure 4.2 (c) and (d). On the other hand, since the $< 111 >$ direction is at an angle from the bubble for the (110) surface cases, the adatoms instead form platelets on the surface that are at angle from the bubble and the bubble will expand in a more lateral direction, as seen in figure 4.2 (a) and (b). The general results for each surface are consistent regardless of the temperature or bubble concentration. However, at higher temperatures and higher helium concentrations, the loop punching will occur more swiftly and will lead to greater surface deformation. Interestingly, the hydrogen concentration has virtually no effect on the loop punching process indicating that it is the helium pressure within the cavity (bubble) that is driving the bubble expansion.

Figure 4.2 shows that after 100 ps, the positions of the hydrogen atoms have changed significantly. The hydrogen is all initially placed inside the bubble at random positions, but following the 100 ps a significant portion of the hydrogen has segregated to the periphery of the helium bubble. This is observed for all simulations, regardless of the initial parameters or temperature. Figure 4.2 has inset images of a slice through the middle of the bubble that clearly display the hydrogen segregation to the bubble periphery, especially when compared to the inset in Fig. 4.1 that shows the initial random distribution. The hydrogen tends to prefer the void region between the helium bubble and the tungsten matrix. The repulsive nature of the helium-tungsten interatomic potential results in a standoff region which is the area the hydrogen now occupies. This seems consistent with previous DFT results discussed in chapter 1, notably that hydrogen prefers vacancy-like regions because of the low electron density. This stand-off region between the helium and tungsten is a good site for trapping hydrogen. With the large expected concentration of near-surface helium bubbles that will be present in a tungsten divertor, it is possible that a large concentration of hydrogen could become trapped at these bubble sites.

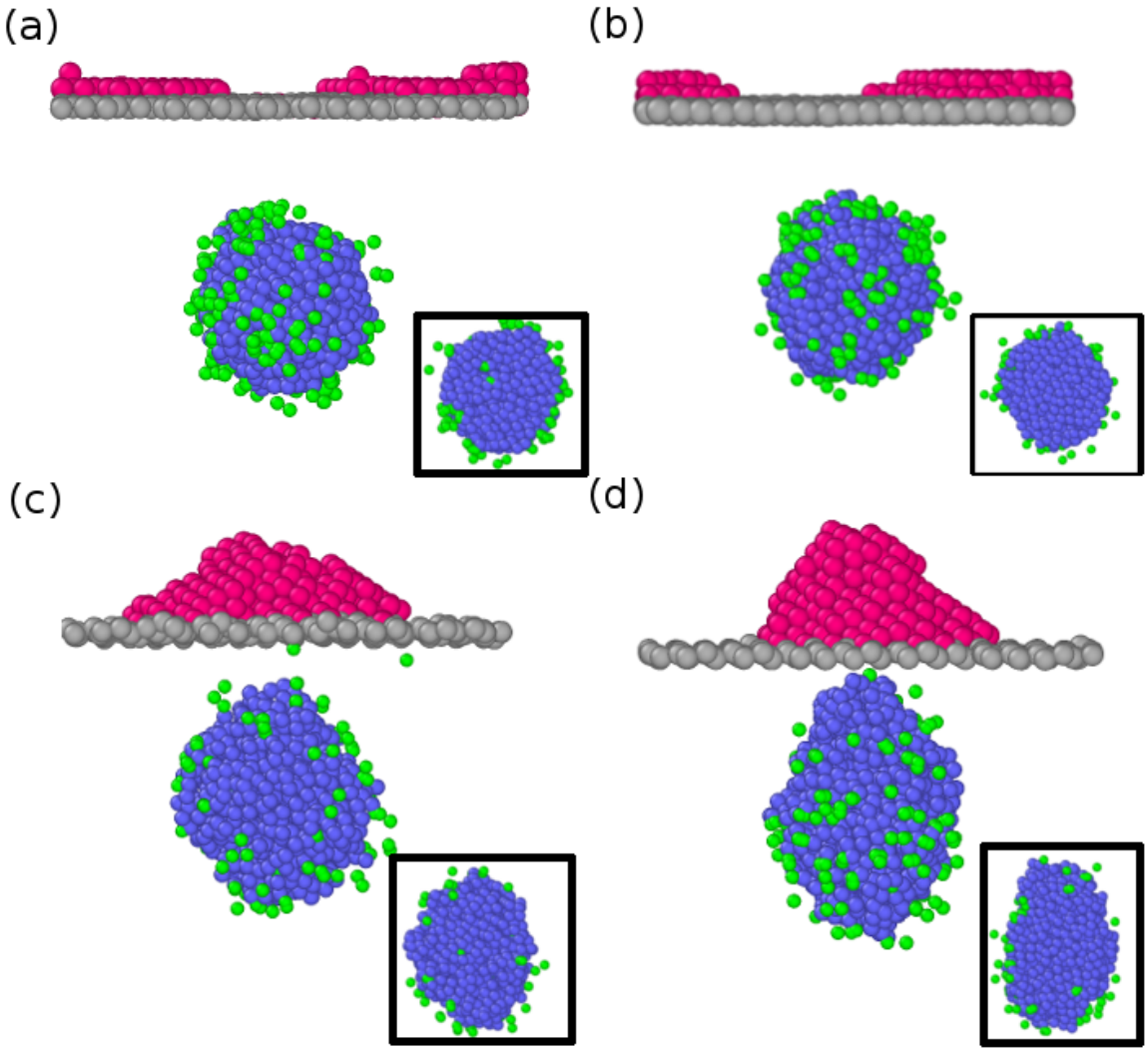

Figure 4.2: Atomistic snapshots of the nominal mixed hydrogen-helium bubbles for parameters of (a) (110) surface orientation, 1200 K, and concentrations of 3.5 He/V and 1 H/V, (b) (110) surface orientation, 1200 K, and concentrations of 4 He/V and 1 H/V, (c) (111) surface orientation, 2000 K and concentrations of 3.5 He/V and 0.5 H/V, and (d) (111) surface orientation, 1200 K, and concentrations of 4 He/V and 0.5 H/V. Blue, green, gray, and magenta atoms represent helium, hydrogen, tungsten, and tungsten adatoms respectively. The images in the boxes for each part are slices of the bubble that depict how most of the hydrogen has left the inner part of the bubble and has migrated to the periphery region.

A few hydrogen atoms remain in the bubble, but most of the hydrogen segregates to the bubble periphery. The hydrogen in these different regions has been quantified. In order to do this, it is necessary to determine what exactly is the radius of the bubble, which is difficult due to non-isotropic expansion of the helium bubble. For this quantification, an average radius was calculated by sampling 150 cords intersecting the bubble from one side of the bubble to another. The radius tends to be between 1 nm and 2 nm with a standard deviation of 0.1 nm to 0.3 nm depending on the temperature and initial helium concentration. However, this method will ultimately lead to an overestimation of the bubble radius and therefore an underestimation of the hydrogen gas density within the bubble. An alternative method of quantifying the hydrogen at the bubble periphery is to perform a nearest neighbor analysis between the hydrogen and tungsten. Because of the stand-off distance between the helium bubble and the tungsten matrix, a hydrogen atom that has at least 1 tungsten nearest neighbor but less than 8 within a cutoff of 3.2 Angstroms would be considered at the bubble periphery. A hydrogen atom with no tungsten nearest neighbors would be considered to be inside the bubble while a hydrogen atom with 8 or more tungsten nearest neighbors would be considered completely within the tungsten matrix and no longer in the periphery region itself. For this analysis, the "bubble periphery" will be defined to include the thin-shell region that surrounds the bubble with an innner radius from just inside the bubble and an outer radius that is one to two lattice units into the surrounding tungsten lattice. This method was ultimately chosen to calculate the cumulative radial distribution of hydrogen at the end of the MD simulation.

For each simulation, the partitioning of hydrogen to the periphery region was quantified. The plots in figure 4.3 display the cumulative fraction of hydrogen as a function of radial distance from the bubble center for a select few cases that correspond with the snapshots in figure **??**. While results from only a few simulations are presented here, the general trend from these plots is consistent with the data from more than 260 MD simulations. In these plots, the black line represents the initial random distribution within the bubble while the green dotted line denotes the positions after 100 ps. For each plot, hydrogen identified to be at the inner and outer radius of the thin shell of the periphery region based on the nearest neighbor analysis was denoted by the circle and star respectively. The grey region represents the range of bubble radii due to non-isotropic expansion based on the coord length analysis. From these plots, it is clear that there is a large amount of hydrogen located in the periphery region, indicated by the steep slope in the hydrogen fraction between the two points that denote the periphery radii. For all cases, the percent of hydrogen that is located at the periphery is between 75% and 95% (17.7-22.4 $\frac{H}{nm^3}$). On the other hand, only a small amount of hydrogen, typically less than 20% (4.5 $\frac{H}{nm^3}$), remains within the helium bubble. The hydrogen in the bubble tends to take the form of molecular hydrogen (H_2). Regardless of the temperature, initial gas atom concentration, and surface orientation, the same trend is observed. For all cases, the partitioning occurs rapidly, typically within a 1 to 2 picoseconds and more or less

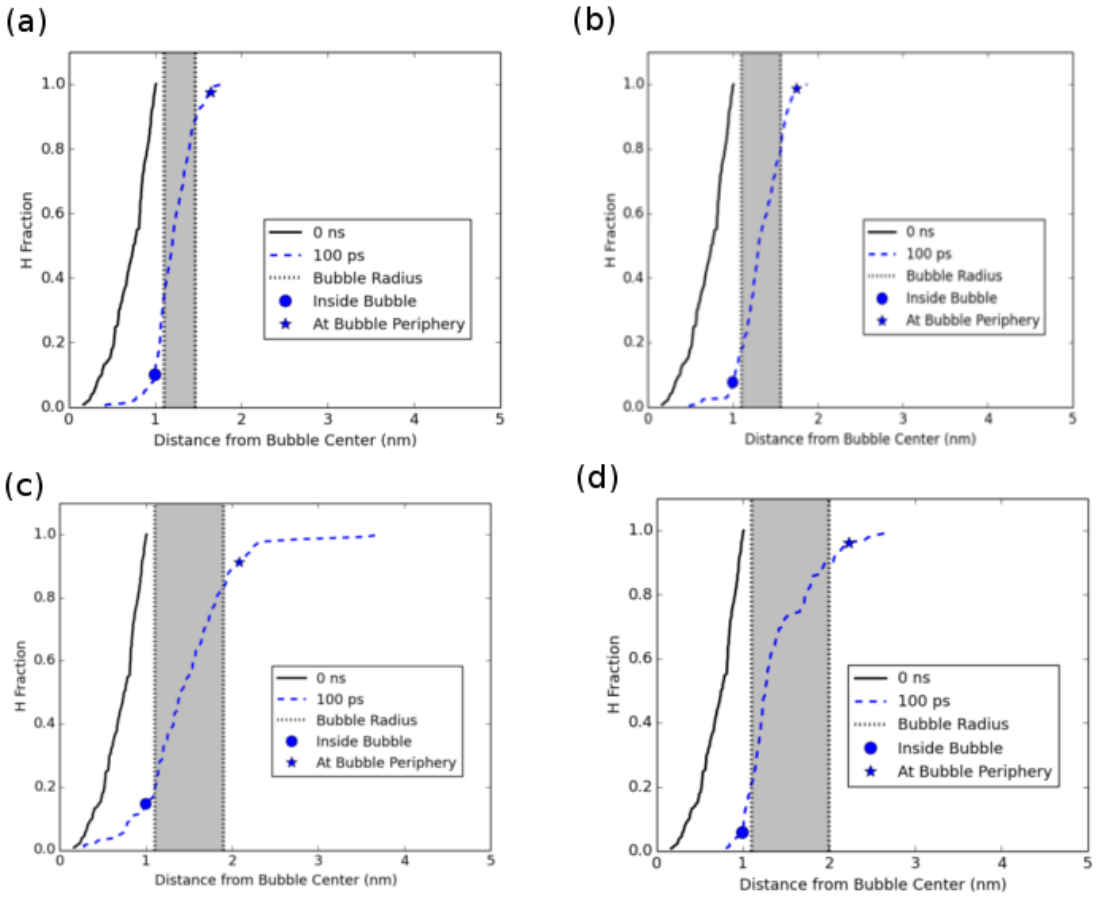

Figure 4.3: Plots of the hydrogen cumulative radial distribution for the (a) (110) surface orientation, 1200 K, and concentrations of 3.5 He/V and 1 H/V, (b) (110) surface orientation, 1200 K, and concentrations of 4 He/V and 1 H/V, (c) (111) surface orientation, 2000 K and concentrations of 3.5 He/V and 0.5 H/V, and (d) (111) surface orientation, 1200 K, and concentrations of 4 He/V and 0.5 H/V. Black lines represent the initial distribution while green lines represent the distribution after 100 ps. The dotted lines and gray area show the range of radii for the non-isotropic growth of the helium bubbles. The dots and stars represent the hydrogen within the bubble and at the periphery respectively.

remains consistent for the remainder of the simulation. However, a few hydrogen atoms in each have indeed migrated out into the tungsten matrix. These simulations are very short, only 100 ps, and therefore it is difficult to assess whether the hydrogen will continue to remain trapped at the bubble periphery or will diffuse out into the lattice region.

While the general trend of the hydrogen radial distribution is consistent across the simulations, there are a few variations that depend on the initial simulation parameters. At higher temperatures, the bubble expands more, typically by a few tenths of a nanometer. This causes the hydrogen to diffuse further into the tungsten matrix compared to the lower temperature simulations. A similar trend is also seen for higher helium concentrations. In addition, increasing the initial helium concentration actually decreases the hydrogen concentration ($\frac{H}{nm^3}$) at the bubble periphery. However, this is not due to a lower absolute quantity of hydrogen at the periphery but depends on the higher initial bubble pressure and greater bubble expansion that leads to a periphery shell that has a larger volume instead. In reality, the absolute value of hydrogen at the periphery seems to be independent of intial helium concentration but is instead influenced more by the intial hydrogen concentration. At higher H/V values, there tends to be more hydrogen that diffuses into the periphery region as well as a larger hydrogen concentration. The amount of hydrogen remaining within the bubble is dependent upon the temperature. At 1200 K, the hydrogen fraction within the bubble is typically only a few perecent ($\sim$0.7 $\frac{H}{nm^3}$) while at 2000 K this value rises to about $\sim$25% (6.0 $\frac{H}{nm^3}$). Molecular hydrogen forms more frequently and in higher quantities at 2000 K as well.

Next, the results from the modified cases will be discussed. The first results that will be presented are those from the simulations with a different initial distribution of hydrogen. For the nominal cases, the hydrogen was first randomly placed within the bubble and after 100 ps, the hydrogen then migrated to the bubble periphery. It is possible that the results could be biased based on the initial hydrogen being placed directly in the bubble so in order to test this, a set of simulations were performed such that the same amount of hydrogen was placed throughout the entire tungsten cell. This was performed for simulations at temperatures of 1200 K, 1800 K, and 2000 K and for gas atom concentrations of 3 He/V and 1 H/V for both surface orientations of (110) and (111). It was necessary to extend these simulations to 10 ns in order to allow enough time for the hydrogen to diffuse throughout the box. Atomistic snapshots and a plot of the cumulative radial distribution of hydrogen at 0 ns, 1 ns, 5 ns, and 10 ns for the case at 1800 K can be seen in figure 4.4. The results of this perturbation show that although the hydrogen was placed throughout the box, by the time 10 ns had passed the hydrogen had still diffused to the bubble periphery. The amount of hydrogen at the bubble edges was about 30-40%, or 13.4 to 21.2 H/nm^3, depending on the temperture.

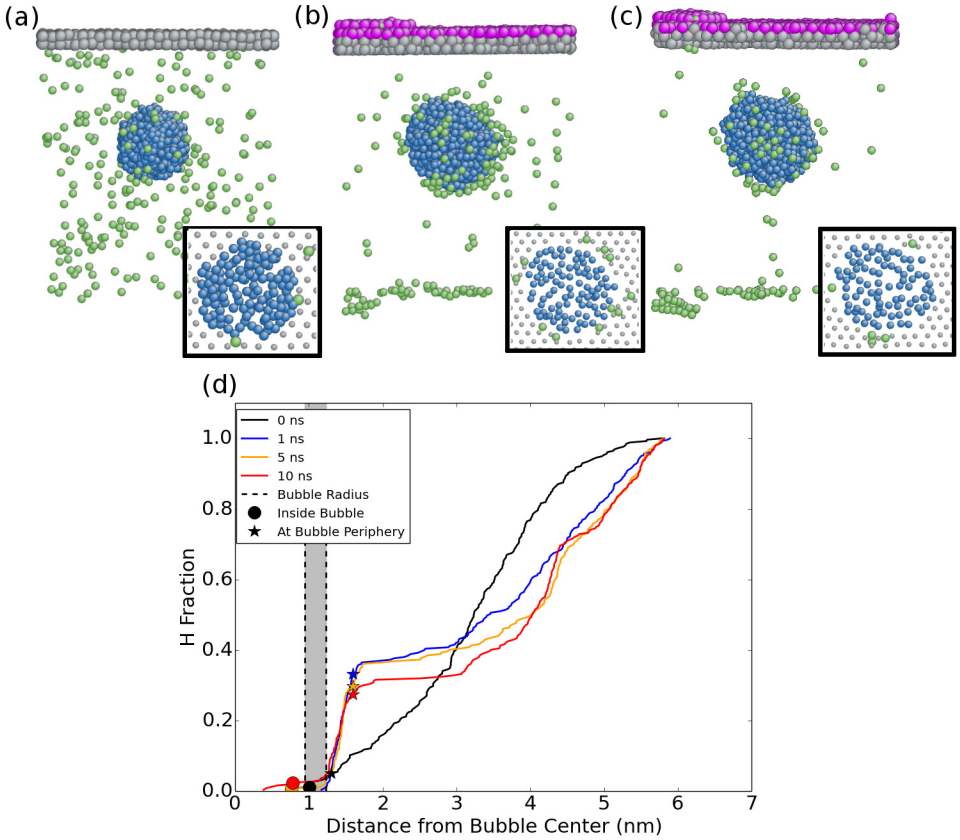

Figure 4.4: MD snapshots of hydrogen diffusion in the presence of a helium bubble at 1800 K for a surface orientation of (110) and gas atom concentrations of 3 He/V and 1 H/V with the hydrogen initially placed throughout the simulation cell. Snapshots are taken at (a) 0 ps, (b) 1 ns, and (c) 10 ns. A plot of the radial distribution of hydrogen from the center of the bubble is shown in (d). Green, blue, gray, and magenta atoms represent hydrogen, helium, tungsten and tungsten adatoms respectively. The inset images depict slices through the middle of the bubble. Note that hydrogen quickly segregates to the bubble periphery as well as the top and bottom surfaces. Ref. [97]

A substantial amount of hydrogen has still migrated to the bubble periphery in this case, indicating that the initial results from the nominal cases still hold true although perhaps with a slightly reduced segregation. The 1800 K snapshots, which are respresentative of all the cases modeled, clearly depict a large amount of hydrogen at the bubble-tungsten interface. In fact, the hydrogen fairly quickly migrates to this region and more or less remains there at a steady-state value until the end of the 10 ns. Therefore, the hydrogen still has not de-trapped from the periphery region even after 10 ns at 1800 K. Although the distribution does slightly decrease between 5 ns and 10 ns, the amount is fairly small and most of the hydrogen still remains at the periphery. This is still a relatively short period of time but even so, there is no indication that the hydrogen will leave the bubble periphery. Another interesting observation from the snapshots is that most of the hydrogen not located at the bubble edge is located at either the top or bottom surface. Again, this further affirms the idea that hydrogen is draw to vacancy-like defects and surfaces in order to minimize the local electron density, at both the void-like standoff distance between the helium bubble and tungsten matrix as well as the void region at the top and bottom surfaces of the tungsten cell. This is further established from the cumulative radial distribution plots, which have large increases in the hydrogen fraction at the radial distances of 4.3 nm and 6.1 nm where the top and bottom surfaces are located at. However, the amount of hydrogen per surface area is still larger at the bubble interface compared to the free surfaces, with an average of 4.5 H/nm^2 versus 1.5 H/nm^2. In fact, none of the hydrogen has left the simulation cell indicating the trapping strength of both the bubble periphery and the free surfaces on hydrogen.

These additional sets of simulations indicate that the initial hydrogen distribution did not affect the segregation of hydrogen atoms to the helium bubble periphery. To further investigate this dependence, a simulation with a void containing no helium was performed to assess the strength that the presence of helium in the void affects the results. The hydrogen was again distributed throughout the simulation cell but there was no helium placed in the 2 nm void. Again, the hydrogen tended to diffuse to the bubble periphery as well as the two free surfaces. However, the degree to which the hydrogen migrates to the bubble periphery is somewhat less than for the case when there is helium present within the void. At 1 ns there is about 10% (1.3 H/nm^3), of the hydrogen at the bubble periphery and this values increases to about 25% (5.3H/nm^3) at the end of the 10 ns. This is slightly smaller than for the case with helium in the void but neverthless, it still represents a large portion of the hydrogen. The hydrogen in this case also, for the most part, migrates to the bubble periphery early in the simulation and remains there throughout the entire run. In addition to hydrogen at the periphery, a small amount of hydrogen has entered the void itself. The total amount of hydrogen inside the void is ∼3% (1.3 H/nm^3). The remainder of the hydrogen mostly resided at the free surfaces while some of the hydrogen formed clusters within the bulk.

While there was no biasing of the results based on the initial distribution of hydrogen atoms, the length of the simulations, as well as the size of the simulation cell, is relatively small. A time of 100 ps is fairly short even for MD and makes it hard to extract the simulations to experimentally relevant scales. In addition, having a 6 nm x 6 nm box with periodic boundary conditions leads to a very large areal density of helium bubbles created in the periodic images. The bubble areal density for this case is $3x10^{16}$ bubbles/m^2 which corresponds to a bubble density of $5x10^{24}$ bubbles/m^3. Lastly, the bubble depth in the z direction will change the proximity to the surface, which can modify the strength of the surface sink. The time and geometry parameters were therefore varied as well and the results are discussed next.

As stated earlier, 100 ps is a short time which makes it challenging to determine whether the hydrogen will remain at the periphery or eventually migrate to the surface. Therefore, a few select simulations were extended past 100 ps to evaluate further hydrogen diffusion. By the end of the 100 ps, the hydrogen quickly diffuses to the bubble edge and more or less remains there for the rest of the simulation. However, for the simulations that were run past 100 ps, some of the hydrogen atoms did start to diffuse away from the bubble and towards the surface. Figure 4.5 depicts an example of this for the 1800 K simulation with initial gas atom concentrations of 3 He/V and 0.5 H/V for the (111) surface at 0 ps, 100 ps, and 1 ns in parts (a), (b), and (c), respectively. It is readily apparent that some of the hydrogen has started to migrate away from the bubble periphery and further into the bulk tungsten, with a couple of hydrogen atoms even migrating to the surface itself. The bubble expansion tends to be biased toward the surface which apparently provides an easy pathway for the hydrogen to diffuse up towards the surface, especially for the (111) case. By 5 ns, ~4-8% of the hydrogen initially in the bubble has diffused to the free surface. This results in hydrogen surface concentrations of about 0.14 to 0.28 H/nm^2 for the 0.5 H/V simulations and 0.28 to 0.57 H/nm^2 for the 1 H/V simulations. The radial distributions are shown in figure 4.6(a) where the black, green, and blue lines represent the distribution at 0 ps, 100 ps, and 1 ns respectively. It is important to note that even after 1 ns, the distribution does not signficantly change. While some of the hydrogen does begin to diffuse away, the majority of the hydrogen still remains in the bubble periphery. In addition, the surface deformation from the loop punching processes remains the same even after a few nanoseconds, indicating that the bubble expansion occurs relatively quickly and remains in a steady state for the rest of the simulation.

Next, the results from extending the simulation in the lateral dimensions will be discussed. The orginal x and y lengths were both extended from 6 nm to 12 nm while the z direction was kept the same. This changes the areal density and volumetric density to $7x10^{15}$ bubbles/m^2 and $1x10^{24}$ bubbles/m^3 respectively. The bubble spacing in the nominal case would have resulted in high strain fields in the tungsten matrix due to the close proximity of many highly pressurized helium

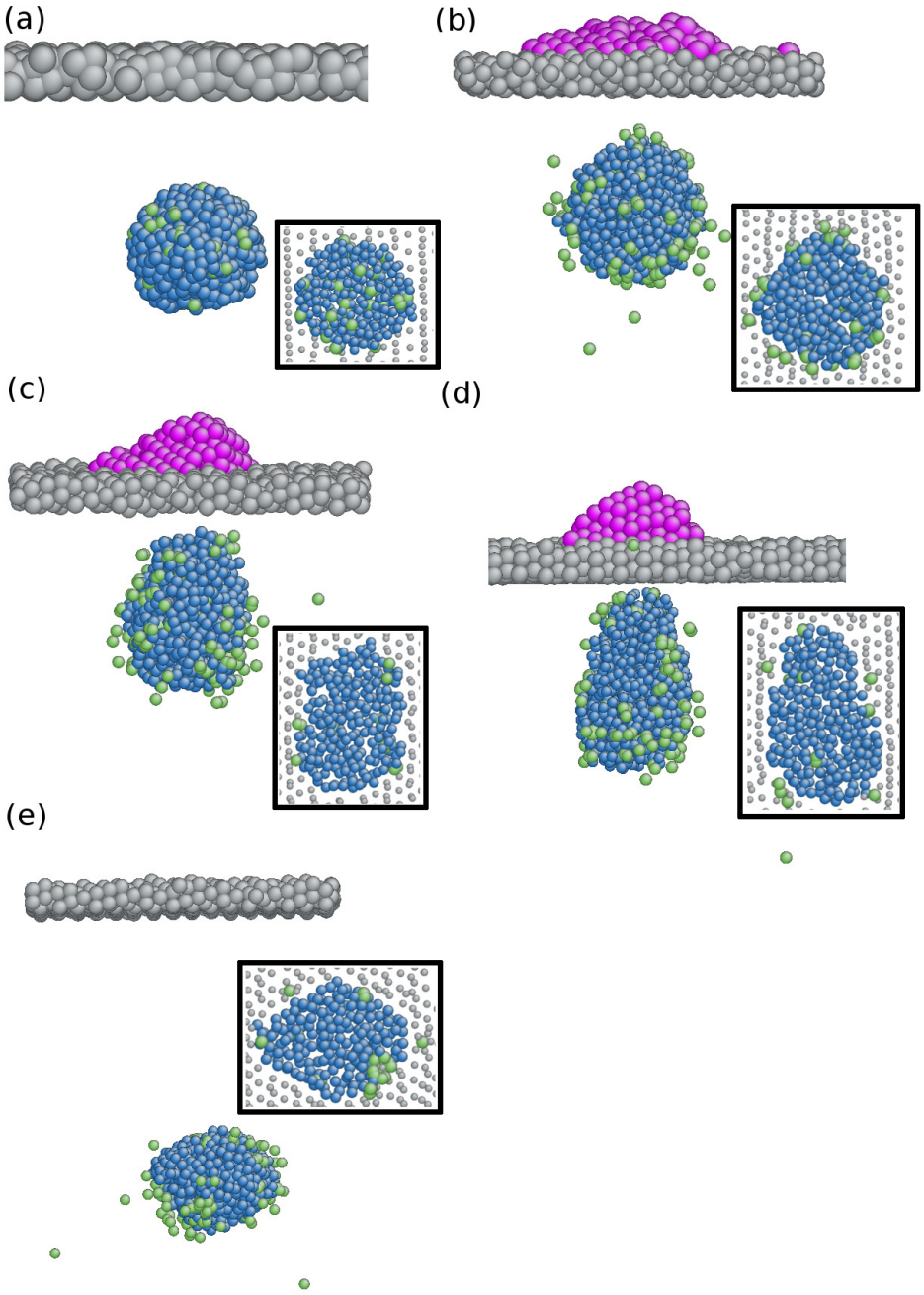

Figure 4.5: MD snapshots of hydrogen diffusion in the presence of a helium bubble at 1800 K for a surface orientation of (110) and gas atom concentrations of 3 He/V and 1 H/V where the hydrogen is initially placed randomly within the helium bubble for (a) the initial distribution at 0 ps, for the 6 nm x 6 nm x 6nm box (b) at 100 ps, and (c) at 1 ns, for the (d) 12 nm x 12 nm x 12 nm box at 1 ns, and for the (e) 6 nm x 6 nm x 12 nm box. Blue, green, gray, and magenta atoms represent helium, hydrogen, surface tungsten atoms, and tungsten adatoms respectively. Ref. **??**

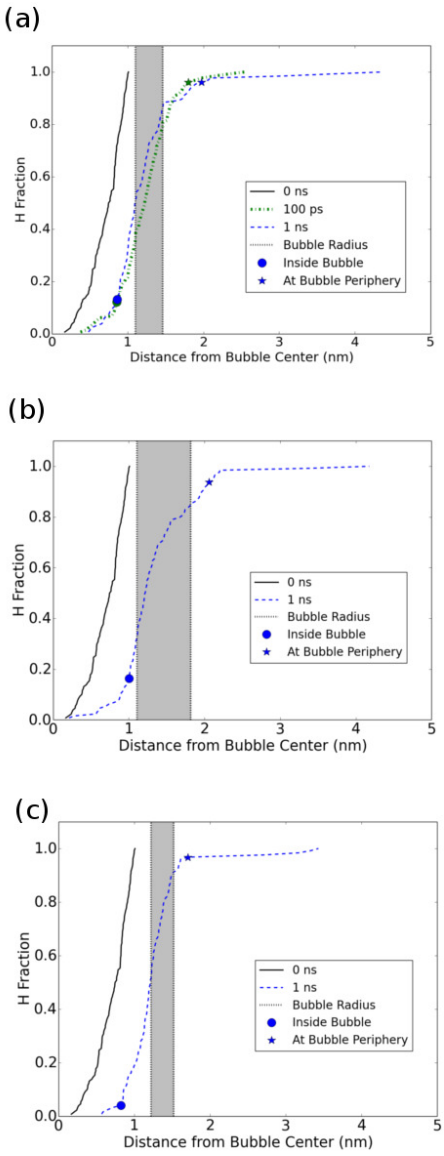

Figure 4.6: Cumulative radial distribution plots for hydrogen for extended simulations for a surface orientation of (110) at 1800 K and gas atom concentrations of 3 He/V and 1 H/V for geometries of (a) 6 nm x 6 nm x 6 nm, (b) 12 nm x 12 nm x 12 nm box, and (c) 6 nm x 6 nm x 12 nm. Black, green and blue lines represent 0 ps, 100 ps, and 1 ns. The gray area marks the range of the radii for the helium bubble after expansion. The dot and star denote the hydrogen in the bubble and at the periphery respectively. Ref. [97]

bubbles across the periodic images which may affect the results initially obtained. Figure 4.5(d) depicts the atomistic snapshots for this simulation, showing the larger radii of the bubble after the 100 ps for this perturbation. With the large lateral dimenstions, the resulting surface deformation from the loop punching process has increased, especially for the (110) surface orientation and higher gas concentrations. In fact, for some helium concentrations, the gas pressure inside the bubble was enough for the bubble to actually rupture, creating a crater on the surface. Subsequently, all of the gas atoms were relased from the tungsten. Rupturing occured at 4 He/V for both surface orientations while increased surface deformation occured at lower concentrations of 3 He/V for the (110) surface. This behavior may be linked to the lower areal density since the lateral dimensions were increased. When the initial areal density was very high, there is much more compressive strain in the x and y directions which causes the bubble to expand more towards the surface. When the lateral distance between bubbles was increased, it allowed for the bubbles to expand more in the x and y direction because of the lowered compressive strain. This resulted in greater bubble expansion and therefore greater surface deformation. This was confirmed by comparing the average radii between the nominal and laterally expanded cases, which was 1.2 to 1.6 nm for the nominal case and 2.0 to 2.4 nm for the expanded case. The cumulative distribution plot in figure 4.6 (b) shows this as indicated by the increase in the gray bar that depicts the range of the bubble radii.

The hydrogen in the simulation with the double x and y lengths behaved in a similar way to the nominal case, as shown in figure 4.6. Again, the hydrogen diffused to the bubble periphery in large quantities. About 70% or so of the hydrogen ended up at the bubble-tungsten interface, however, because of the larger bubble radius, and hence larger periphery volume, the hydrogen density actually decreased from $\sim$20 H/nm^3 to $\sim$ 5 H/nm^3. While expanding the lateral dimension did not change the observation of hydrogen partitioning to the bubble periphery, the bubble evolution did change and affected the hydrogen density at the periphery. This implies that the lateral spacing between the bubbles will alter the results and therefore the value for this parameter should be kept in mind in further simulations of this type.

The second geometry variation was to double the depth in the z direction from 6 nm to 12 nm while also doubling the bubble depth from 3 nm to 6 nm below the surface but keeping the x and y lengths the same. This keeps the areal density the same but the volumetric density is decreased from $5x10^{24}$ to $2x10^{24}$ bubbles/m^2. The initial bubble evolution is similar to the nominal case, where the bubble is initially overpressurized and expands by dislocation loop punching. However, due to the greater depth of the bubble, the typical surface deformation in the nominal case is much less pronounced. This makes sense since the distance to the surface from the bubble is larger in this case and therefore the adatom islands will not be as large. This is clearly seen in the atomistic snapshots in figure 4.5 for this simulation, where there are virtually no adatoms depicted in the image here. However, the greater

bubble depth does not significantly affect the the hydrogen partitioning to the bubble periphery, as seen in the resulting cumulative radial distribution plot in figure 4.6(c). The amount of hydrogen at the bubble periphery after 100 ps is fairly comparable to that for the nominal cases. In addition, there are also a few hydrogen that remain within the bubble region as previously described for the nominal cases.

The geometry variations were also extended to simulations where the hydrogen was placed throughout the tungsten cell for both the extended lateral and depth cases. This was done just for a temperature of 1800 K and gas atom concentrations of 3 He/V and 1 H/V. For both cases, the simulation results are similar to the nominal cases where hydrogen is placed throughout the simulation cell. Hydrogen quickly diffuses to the bubble periphery and the amount of hydrogen here remains more or less at a constant value until the end of the 10 ps simulation. However, the extent to which the hydrogen diffuses to the bubble periphery is somewhat less for the laterally extended box, with a value of only about 9.4%. This is especially true when looking at the volumetric density which is only 7.3 H/nm^3. For the double depth simulation, about 35% (17.4 H/nm^3) of the hydrogen is at the bubble periphery at 10 ns, which is comparable to the nominal case. Again, a large portion of the hydrogen diffuses to the top and bottom surfaces for both cases while a small amount of hydrogen does remain within the helium bubble, about 1.5% or 0.77 H/nm^3.

In addition, a simulation with a 2 nm void that contained no helium was also performed for the case where the z length was doubled. The snapshots from this simulation are shown in figure 4.7. Again, the hydrogen perferentially segregates to the cavity periphery and free surfaces. For this case, as shown in the cumulative radial distribution plot in figure 4.7(d), about 30% of the hydrogen ends up at the periphery after 10 ns, which is again slightly lower than the case when there is helium in the simulation. In this simulation, there is roughly an equal amount of hydrogen that diffuses to the top and bottom surfaces. However, the areal density is also lower at the free surfaces compared to the cavity surface, which is 2.0 H/nm^2 and 4.7 H/nm^2. There is also a small amount of hydrogen in the void itself, effectively mkaing it a small hydrogen bubble. The results from this simulation also indicate that the length in the z direction does not greatly affect the partitioning of hydrogen to the periphery region for either the helium bubble or void case.

All of the previously shown radial distribution plots for the cases where hydrogen is initially placed throughout the simulation cell indicate that the hydrogen density rapidly increases near the bubble periphery within about 1 ns and then slighly decreases to an approximately constant value by 10 ns. Therefore, the hydrogen density in the periphery region as a function of time has been tracked and plotted in figure 4.8 for a variety of cases. The data included from this figure is from the nominal 6 nm x 6 nm x 6 nm case, the laterally extended 12 nm x 12 nm x 6 nm case, the double z depth 6 nm x 6 nm x 12 m case, and the double z depth 6 nm x 6 nm x 12

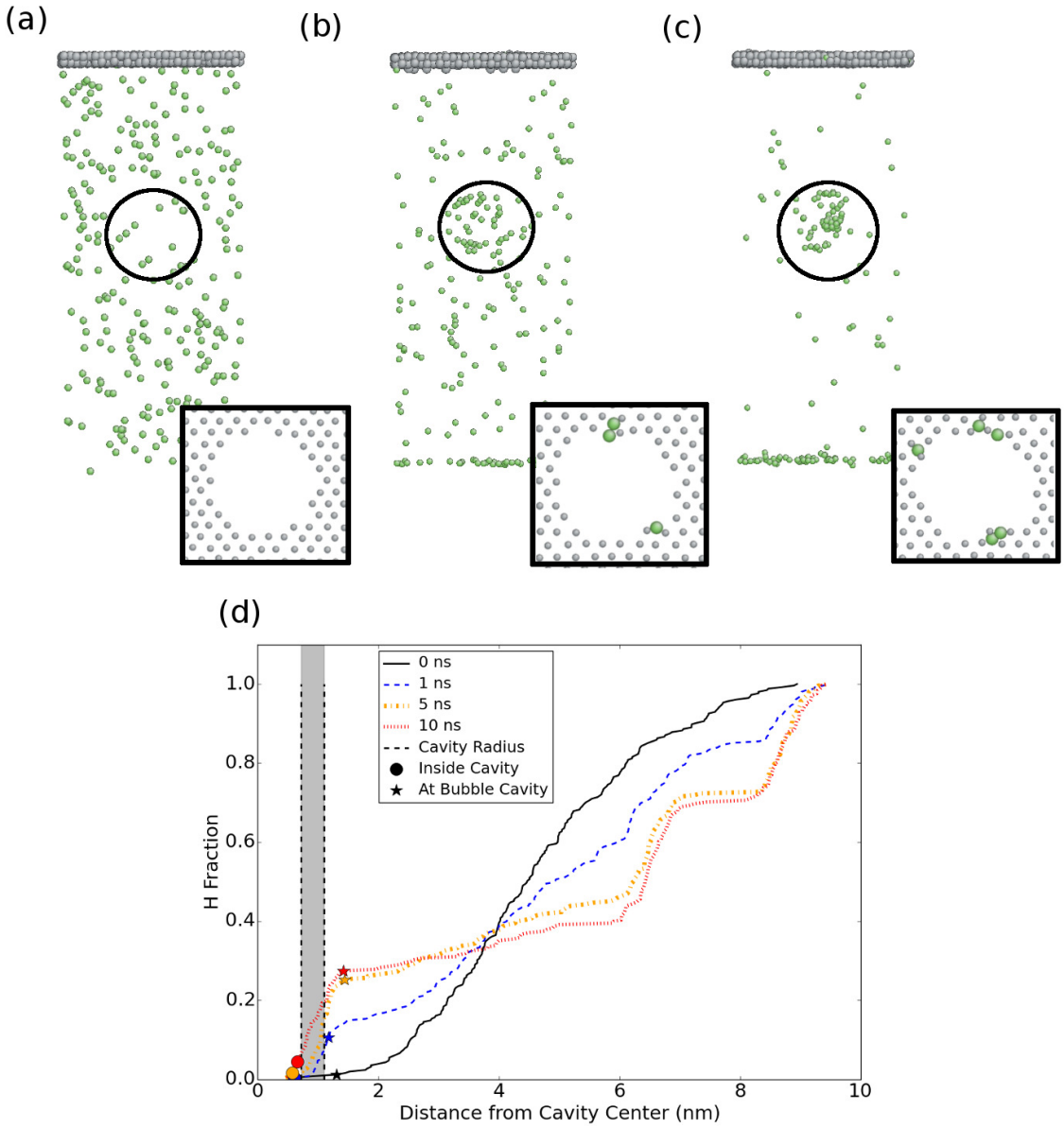

Figure 4.7: Atomistic snapshots for the cavity simulation and no helium with a (110) surface orientation at 1800 K and a hydrogen cocentration of 1 H/V randomly distributed throughout the 6 nm x 6 nm x 12 nm box at (a) 0 ns, (b) 1 ns, and (c) 10 ns. The green and gray atoms represent hydrogen and surface tungsten respectively. The cumulative radial distribution plot is show in (d). The black, blue, orange, and red lines represent the distribution at 0 ns, 1 ns, 5 ns, and 10 ns. The gray area marks the range of the radii for the helium bubble after expansion. The dot and star denote the hydrogen in the bubble and at the periphery respectively. A black circle is drawn to denote where the void is. Ref. [97]

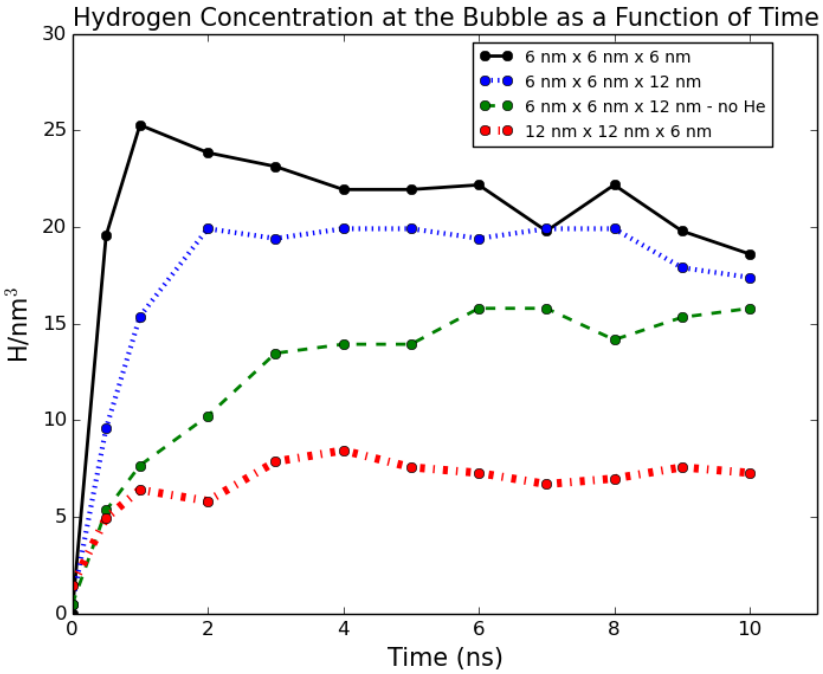

Figure 4.8: Plot of the hydrogen density near the bubble as function of time for the (110) surface at 1800 K and gas atom concentrations of 3 He/V and 1 H/V where the H is randomly distributed throughout the box with geometries of 6 nm x 6 nm x 6 nm, 6 nm x 6 nm x 12 nm, 6 nm x 6 nm x 12 nm with no helium, and 12 nm x 12 nm x 6 nm. Ref. [97]

nm with no helium case. The plot confirms that the hydrogen does rapidly segregated to the periphery within the first 3 ns and then reaches an approximately constant value for the remainder of the simulation. The simulation with the nominal geometry and double z length end up at a fairly similar hydrogen density of about 17.4 H/nm^3 while the simulation with just the void ended up at a lower value of 15.8 H/nm^3. However, the simulation with double the length in the lateral dimensions is much lower, about 7.3 H/nm^3 after 10 ns. This is likely due to both the lower strain in the matrix due to the lower bubble areal density as well as the larger diffusional distance to the bubble due to the larger volume within the cell. At the temperature of 1800 K that these simulations were performed, figure 4.8 does not provide any indication that that the hydrogen will diffuse away from the bubble periphery. However, these are still relatively short simulations, reaching only 10 ns, and it is possible that given sufficient time the hydrogen will de-trap and diffuse away.

The results discussed here indicate that there could be large quantities of hydrogen, and therefore tritium, trapped at subsurface helium bubbles. This could potentially become a radiological concern if large amounts of tritium can segregate

to the helium bubble layer. The large amount of hydrogen that remains near the bubble periphery motivates the assessment of the potential energy landscape near the helium bubble to better understand the trapping, or binding, energy of hydrogen. It is likely that the strain field and subsequent void-like standoff distance between the helium bubble and tungsten matrix creates a minimum energy site for the hydrogen. To better understand the strength of the trapping, the binding energy between a hydrogen atom and the helium bubble was calculated through a series of molecular statics calculations. This was performed by first quenching the simulation to 0 K. Next, a hydrogen atom in the bubble periphery was chosen and moved both towards and away from the center of the bubble in 0.1 nm steps, minimizing the energy at each step and recording the potential energy. The potential energy values were then normalized to the value far away from the bubble to achieve an estimate of the binding energy of the hydrogen atom. We have used a sign convention in this analysis such that a negative binding energy represents a bound configuration. For this analysis, 106 individual hydrogen atoms from 21 different simulations were chosen and their binding energies were calculated.

The molecular statics results are shown in figure 4.9 where (a) includes all the data and (b) plots just the average energy at each distance from the bubble with accompanying error bars. Figure 4.9 indicates that there is indeed an energy well near the helium bubble for all cases, regardless of initial parameters. The binding energy ranges from about 1 eV to about 3 eV. The star on 4.9(a) denotes the minimum energy for each case. As the hydrogen atom is moved away from the bubble, the binding energy inceases and eventually results in a constant value that represents the typical hydrogen solution energy at interstital sites in bulk tungsten. This value is what the potential energy was normalized to. However, when the hydrogen atom is moved in the opposite direction towards the bubble center, the potential energy becomes very positive (repulsive) and reaches a local maximum of about 1.5 eV for all cases. This indicates that the helium bubble itself is a very high energy configuration and will ultimately drive the hydrogen to the periphery where the energy landscape is much more favorable. This potential well is about 2 lattice units thick, which corresponds very well with the typical width of the bubble periphery. This low energy region most likely explains the segregation of the hydrogen atoms to the bubble periphery. The average values are very consistent in the bubble itself and out in the bulk. The error bars are a bit larger in the periphery region due to the range of binding energies calculated and the variety of simulations and location of hydrogen atoms chosen.

While all the data is plotted here together, an analysis of the binding energy based on the initial simulation parameters indicates that there is virtually no correlation between binding energy and temperature, gas atom concentration, or geometry. Tentatively, the average binding energy of the hydrogen to the bubble is 1.99 ± 0.59 eV. However, there is typically a larger activation energy for these types of traps that must be overcome for the hydrogen atom to detach from the bubble periphery and diffuse

away into the tungsten matrix. This de-trapping activation energy is the sum of the binding energy of the hydrogen at the bubble periphery and the migration energy of a single hydrogen atom in bulk, defect-free tungsten. The hydrogen migration energy is experimentally calculated to be ∼0.3-0.4 eV [63] [24]. With this additional activation energy, the average detrapping energy could be as high as 2.3-2.4 eV. This is a high detrapping energy even at temperatures around 1000°C and experimental time periods outside the realm of MD. This implies that even at the high temperatures seen at the divertor surface, hydrogen will remain trapped at these helium bubble sites.

4.2.3 Conclusions

In this section, MD simulations of mixed hydrogen-helium subsurface bubbles have been performed for a variety of temperatures, surfaces, gas atom concentrations, inital hydrogen placement, and geometries in order to understand the hydrogen segregation and trapping near a high pressure helium bubble. Observations first note that the helium bubble expands through dislocation loop punching which leads to tungsten surface deformation in the form of tungsten adatoms similar to previous MD simulations[28] that have investigated this phenomena. The surface deformation depends on the surface orientation and the helium concentration, but not the hydrogen concentration, initially within the bubble. For simulations with larger dimensions in the x and y directions, the surface deformation was much more pronounced including cases were the bubble ruptured and created a crater on the surface.

A clear trend is observed for all simulations, regardless of initial parameters, for the hydrogen to segregate to the bubble periphery region. The amount of hydrogen in this region ranges from ∼75-95% of the total hydrogen in the MD simulation, corresponding to 17.7-22.4 H/nm^3 depending on the initial parameters of the MD simulation. The bubble periphery is defined to be about a 1-3 nm thick shell that surrounds the helium bubble due to the stand-off distance between the helium and tungsten caused by the repulsive interatomic potential. Even when the hydrogen was initially placed throughout the entire simulation cell as opposed to just within the bubble, a large portion of hydrogen ∼25-40% still segregated to the bubble periphery, while the rest of the hydrgen diffuses to either the top or bottom surfaces after 10 ns of simulation time.

The binding energy between the hydrogen and helium bubble was assessed by a series of molecular statics calculations in order quantify the strength of the interaction. It was found that there is a significant binding energy at the bubble periphery of about 1.99 ± 0.59 eV, which implies a de-trapping activation energy of 2.3 ± 0.6 eV. This indicates that the helium bubbles in a tungsten divertor could become potential

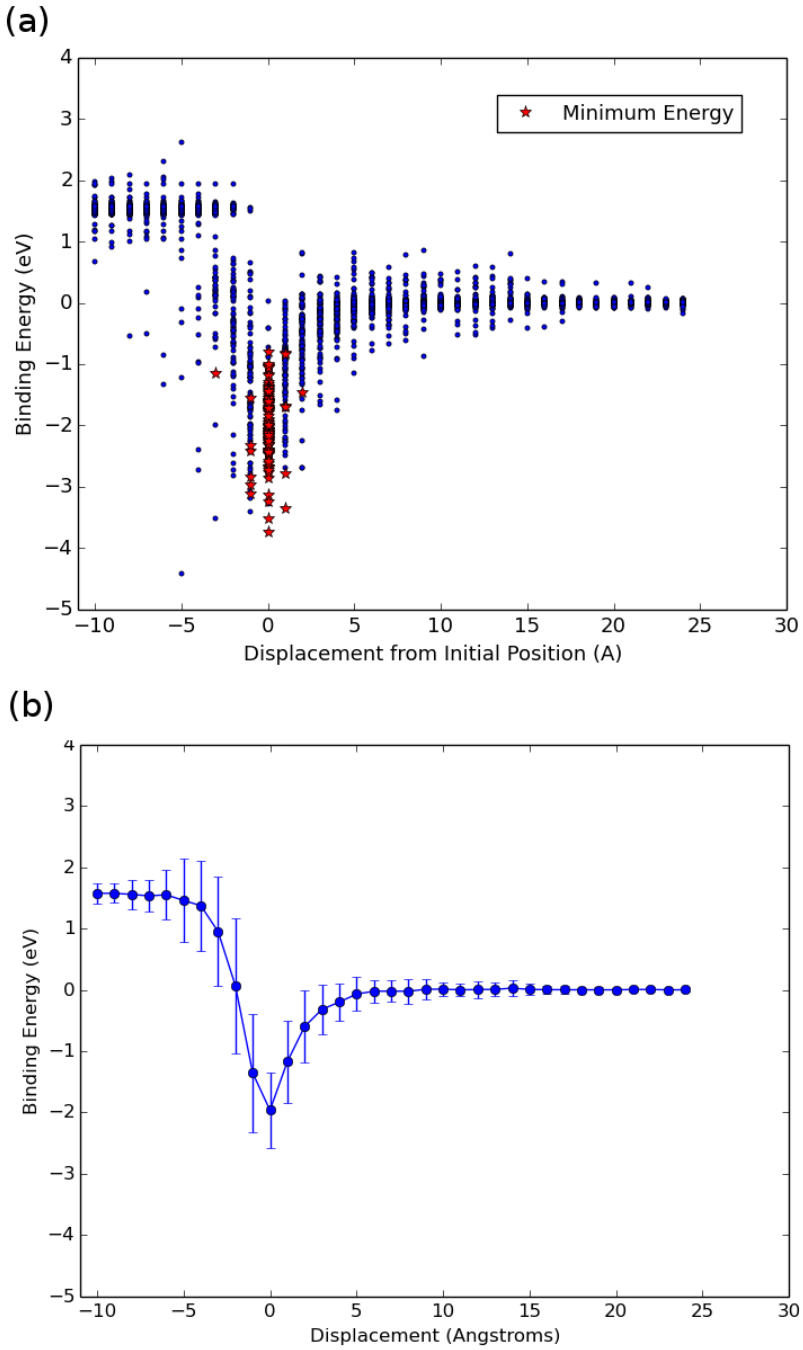

Figure 4.9: Plots of the binding energy as a function of (a) distance from the bubble center and (b) displacement from the atom's position at the end of the simulation. The red star denotes the lowest energy point in a given simulation.

trapping sites for hydrogen, and therefore tritium. The binding energy calculated here is sufficiently large enough to be of concern even at the high temperatures seen at the divertor surface. Further modeling will be needed to better understand the potential implications of this work and verify the results obtained.

4.3 Large Scale Modeling of Hydrogen in Pure Tungsten and Helium Pre-Implanted Tungsten

The results of the previous section indicate a synergistic interaction between hydrogen and helium gas atom species in tungsten. As noted previously, the segregation of hydrogen to the helium bubble periphery could have an impact on the overall tritium retention in the divertor. However, these were very small simulations for the specific case where hydrogen is already present in the material. To further study this behavior another set of large-scale simulations have been performed where hydrogen is implanted into the material. This will provide information on hydrogen behavior with more realistic simulation parameters. Cases where hydrogen is implanted in both pure tungsten and helium pre-irradiated tungsten have been performed. This will allow for comparison between cases with and without helium to see if there is any modification in the hydrogen distribution in the presence of helium bubbles.

4.3.1 Methods

Simulations involving both hydrogen implantation in either pure tungsten or helium pre-irradiated tungsten were performed. Although helium is present in these simulations, the focus is on the hydrogen behavior in tungsten or near helium bubbles in tungsten. Larger simulations were used in order to reduce the typically large fluxes seen in the smaller sized MD simulations. The tungsten cell was 50 nm x 50 nm x 25 nm which amounted to approximately 4 million tungsten. Periodic boundary conditions were used in the x and y directions and a free surface with a (100) surface orientation was used in the z direction. Because of the free surface, it was necessary to include about 3 nm of void both above and below the top and bottom surfaces in order to preserve the fee surface boundary condition. For both cases, it was necessary to use the Juslin[88] W-H Tersoff bond order order potential as modified by Guterl [92] to describe the W-W, W-H, and H-H interactions. The simulations that involved helium also used the Juslin and Wirth potential[82] for W-He, the Beck potential modifiedy by Morishita et al. [84] for He-He, and a Lennard-Jones potential developed by Delashchenko[86] for He-He. There is a second potential W-H potential recently

developed by Wang et al. [98], which is an embedded atom (EAM) style potential. This potential has been used for comparison in siumulations that involve the helium pre-implanted tungsten.

For simulations invlolving pure hydrogen, the tungsten was first equilibrated to a temperature of either 1200 K or 2000 K. Tungsten atoms were initially given a velocity based on a Maxwell-Boltzmann distribution and then velocity rescaling was performed every 100 timestep for 5 ps and then turned off for 15 ps using a time step of 1 fs. Following the initial equilibration, hydrogen was implanted every 10 ps based on the 60 eV depth distribution calculated by SRIM. For each insertion, the tungsten was frozen and then the hydrogen atom was placed at the appropriate position and minimized. This allows the hydrogen atom to move to the lowest energy position and prevent the hydrogen from being placed too close to the tungsten and introduce unrealistically large forces into the system. After the minimization, the tungsten was then unfrozen and the simulation was allowed to run for 10 ps with an NVT thermostat to maintain the temperature at the appropriate value. The timestep used for the W-H potential is 0.1 fs which amounts to 100,000 timestep per insertion. To prevent the tungsten slab from unrealistic movement during the simulation, the bottom layer of atoms were fixed by preventing the center of mass of that layer from moving. Since the W-H Tersoff potential is about 30 times slower than the W-W Finnis-Sinclair potential, it was necessary to use high performance computing. The GPUs on the Titan super computer at Oak Ridge were used in order to speed up the calculations even further. There is a built in package with LAMMPS that allows the force calculations for the Tersoff potential to be done on the gpu called the USER-CUDA package[77]. This was used and provided significant speedup compared to running on just the CPU.

For the case where helium was already present in the simulation, the final state of a purely tungsten-helium simulation performed by Hammond and described in [96] was used. This simulation was performed at 933 K up to a helium fluence of $4x10^{19}m^{-2}$ at a flux of $4x10^{25}m^{-2}s^{-1}$. The size of the simulation cell was 50 nm x 50 nm x 25 nm and the helium was implanted using the same method as the hydrogen. However, since this simulation initially just included tungsten and helium, the tungsten potential that was used was the Finnis-Sinclair potential [79] as modified by Ackland and Thetford [80] and further modified at short distance by Juslin and Wirth[71]. Therefore, when the potential was switched between the W-H Tersoff and EAM potential, some of the helium atoms desorped from the near surface region and had to be removed from the void space above. The reason for this is due to the difference in surface energy and Frenkel pair formation energies between the two tungsten potentials. While the helium were trapped just below the surface from the Finnis-Sinclair potential, they were able to desorb with the Tersoff potential. Two different types of simulations were performed using the helium pre-implanted tungsten. The first involves implanting hydrogen into the material in the same manner as for the pure tungsten case. The

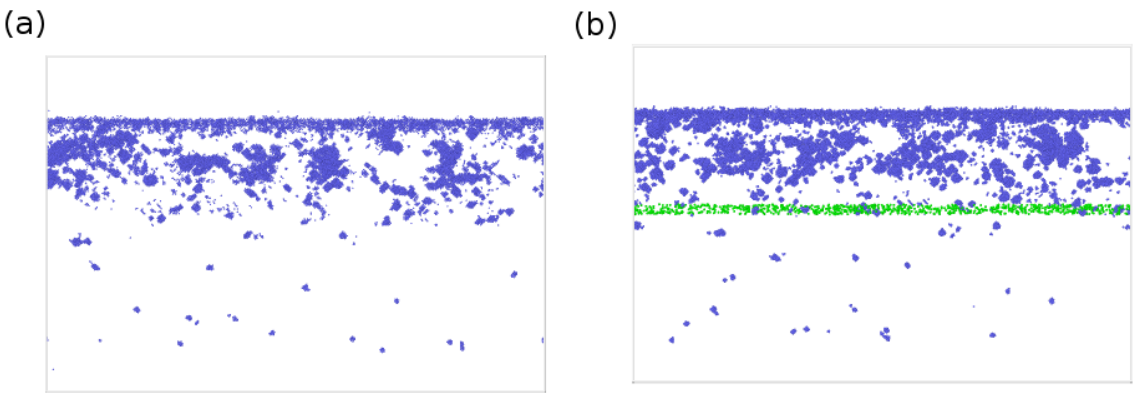

Figure 4.10: Atomistic snapshots of the helium distribution used as the initial state for the case where (a) hydrogen is implanted every 10 ps and (b) an initial layer of hydrogen is implanted below the layer of helium atoms.

second simulation involves implanting a layer of hydrogen below the layer of helium bubbles. About 1,000 hydrogen atoms were implanted between 9 and 10 nm below the surface and dynamics were subsequently performed. For both cases, the diffusion of hydrogen near helium bubbles for two different types of implantation is of interest. Figure 4.10(a) shows the initial distribution of helium atoms where hydrogen will be implanted for the first case and (b) shows the helium distribution with the layer of hydrogen that was initially implanted at the start of the simulation. For each of these cases, simulations using both the Tersoff and EAM potential were performed and compared.

4.3.2 Results

The results for the hydrogen-tungsten simulations will be discussed first. Hydrogen was implanted to a fluence of $1.2x10^{19}m^{-2}$ which amounts to a total of 3,000 hydrogen implantations. Figure 4.11 depicts the sequence of events from atomistic snapshots for the hydrogen implantion at fluences of $4x10^{17}m^{-2}$, $8x10^{17}m^{-2}$, and $1.5x10^{18}m^{-2}$ for both 1200 K and 2000 K. Initial visual observations indicate that a large portion of the hydrogen atoms remain near the top surface for both cases. However, many atoms diffuse deeper into the bulk, in contrast with previous large-scale helium simulations, like the one shown in figure 4.10, where the helium remains within 10 nm of the surface to cluster and form very large helium bubbles. At a temperature of 2000 K, some of the hydrogen even diffuses entirely through the 25 nm slab to reach the bottom of the simulation cell. This is due to the higher hydrogen solubility, combined with the diffusion, that is responsible for increased permeation relative to helium. For hydrogen, there seems to be very little clustering and most of the hydrogen resides as monomers within the bulk. There are a few hydrogen atoms that form groups of two

or three at the surface. At the top surface, the hydrogen is also observed to desorb as H_2 molecules, which is consistent with theory and the modification to the potential. However, at the begining of the simulation, hydrogen initially desorbs as single atoms but once the hydrogen surface coverage increased it desorbs as molecular hydrogen.

The depth distribution of the hydrogen has been quantified and is shown in figure 4.12 for a fluence of $1.5x10^{18}m^{-2}$. The plot clearly shown that for both temperatures, a majority of the hydrogen is at the surface. This amounts to about 85% of the hydrogen for 1200 K and 75% of the hydrogen for 2000 K. Further discussion of the hydrogen behavior at the surface will be presented in the following paragraphs. While many atoms remain near the surface, the hydrogen distribution throughout the rest of the box is fairly uniform. Unlike helium, where large bubbles form within a few nanometers of the surface, hydrogen has a much higher solubililty and diffusivity and will therefore migrate much further into the material. In fact, a few atoms travel to the bottom surface. This is especially evident at 2000 K, where there is a large jump in the hydrogen retention, about 10% or so, at 25 nm, corresponding to the bottom surface, in Fig. 4.12. The hydrogen flux past a depth of 20 nm is $2.0x10^{23}m^{-2}s^{-1}$ at 1200 K and $4.5x10^{24}m^{-2}s^{-1}$ The increased mobility at 2000 K allowed a larger portion of hydrogen to diffuse further into the material, indicating that for future simulations, the box depth should be increased.

The lower amount of hydrogen at the surface at 2000 K is partially due to the deeper hydrogen diffusion but also due to the increased rate of desorption at the surface. The hydrogen percent retention at this fluence is roughly 99% and 95% at 1200 K and 2000 K, respectively. As the number of implanted hydrogen atoms increases, the surface coverage also increases which allows for more molecular desorption, which can be seen by the increased amounts of hydrogen in the void region above the surface in figure 4.11 (f). For the fluence of $8x10^{17}m^{-2}$ shown in figure 4.11 (b) and (e), the amount of hydrogen at the surface is about 80% for both 1200 K and 2000 K, indicating that as the simulation progressed, more hydrogen both desorbed from the surface as well as diffused deeper into the bulk.

Taking a closer look at the depth distribution, there is a difference between the 1200 K and 2000 K cases. At 1200 K, most of the hydrogen are just below the original surface, within the first 2 $\mathring{A}$ or so. However, at 2000 K, most of the atoms near the surface are actually above the original surface. This can be seen in figure 4.13 where (a) depicts the hydrogen depth distribution at the surface, (b) and (c) depict the hydrogen from 1 nm above the original surface to the position of the original surface for 1200 K and 2000 K resepectively, while (d) and (e) depict the hydrogen within 0.2 nm depth below the original surface location for 1200 K and 2000 K, respectively, at a fluence of $1.5x10^{18}m^{-2}$. Green and magenta atoms represent hydrogen and tungsten adatoms respectively. Fig. 4.13a clearly delineates where exactly the majority of the atoms at the surface are actually located. While about 75% of the atoms in the 2000

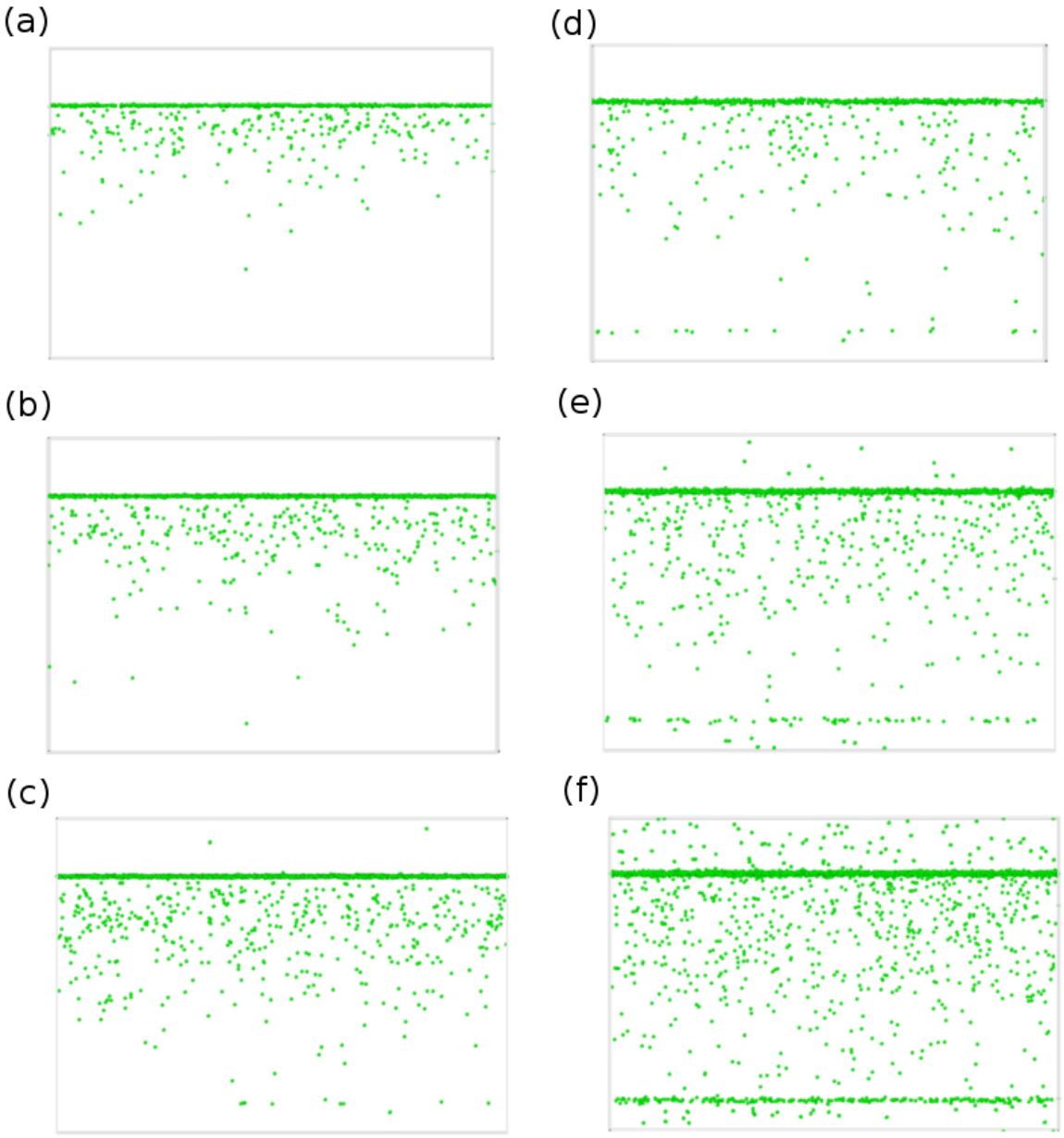

Figure 4.11: Atomistic snapshots of the hydrogen evolution as a function of fluence following implantation into tungsten simulations at 1200 K and an energy of 60 eV at fluences of (a) $4x10^{17}m^{-2}$, (b) $8x10^{17}m^{-2}$, and (c) $1.5x10^{18}m^{-2}$ and at 2000 K and 50 eV at fluences of (d) $4x10^{17}m^{-2}$, (e) $8x10^{17}m^{-2}$, and (f) $1.5x10^{18}m^{-2}$.

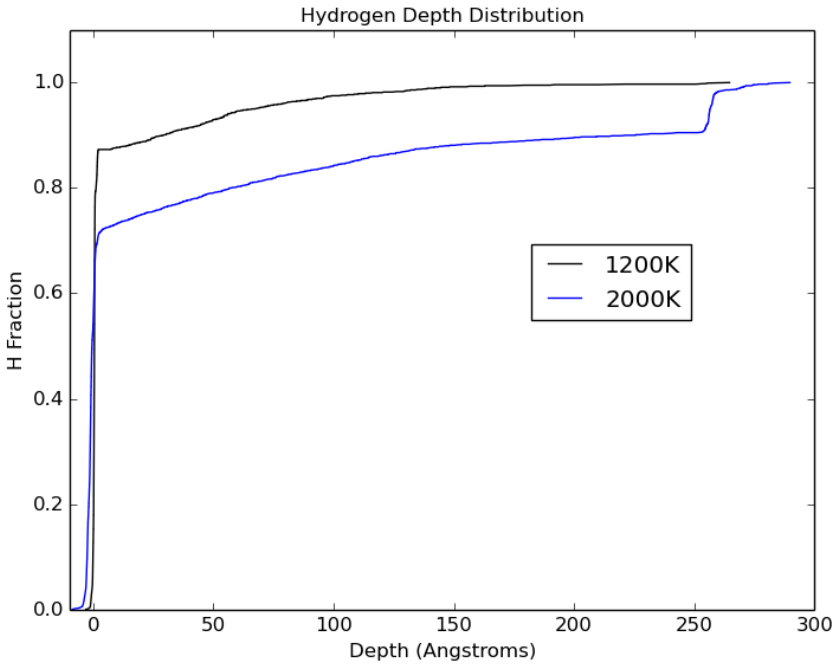

Figure 4.12: Hydrogen depth distribution at a fluence of $1.5x10^{18}m^{-2}$ for 1200 K versus 2000 K, respectively.

K case are located near the surface, almost 60% of the hydrogen sit above the original surface, in a layer that is a mixture of hydrogen and tungsten adatoms as depicted in 4.13(c). On the other hand, less than 20% of the atoms at 1200 K are above the original surface and about 70% are within the first 0.2 nm of the surface. This is further shown in the atomistic snapshots. Another item to note is the increased surface rougness at 2000 K, depicted by the greater number of magenta adatoms, about 78 times more, in the visualization shown in Fig. 4.13(c) compared to Fig. 4.13(b). The number of atoms between images (b)-(e) was quantifed. Above the original surface, there are 268 hydrogen atoms at 1200 K and 1873 hydrogen atoms at 2000 K. Between the surface and a depth of 0.2 nm, there are 2737 hydrogen atom at 1200 K and 122 atoms at 2000 K.

Next, the results for the helium pre-implanted case are discussed. The atomistic snapshots at a fluence of $2.8x10^{17}m^{-2}$ are shown in figure 4.14 where (a) is a reference case without helium, (b) is the case with helium and the Tersoff potential and (c) is the case with helium and the EAM potential. Fig. 4.14(d) depicts the cummulative depth distribution plot where the green, blue, red, and black lines represent the Tersoff helium case, the EAM helium case, the case with no helium, and the initial hydrogen depth distribution. Forthe helium case, the hydrogen atoms still remain near the surface but the distribution, as seen in Fig. 4.14(a) and (b) is slightly

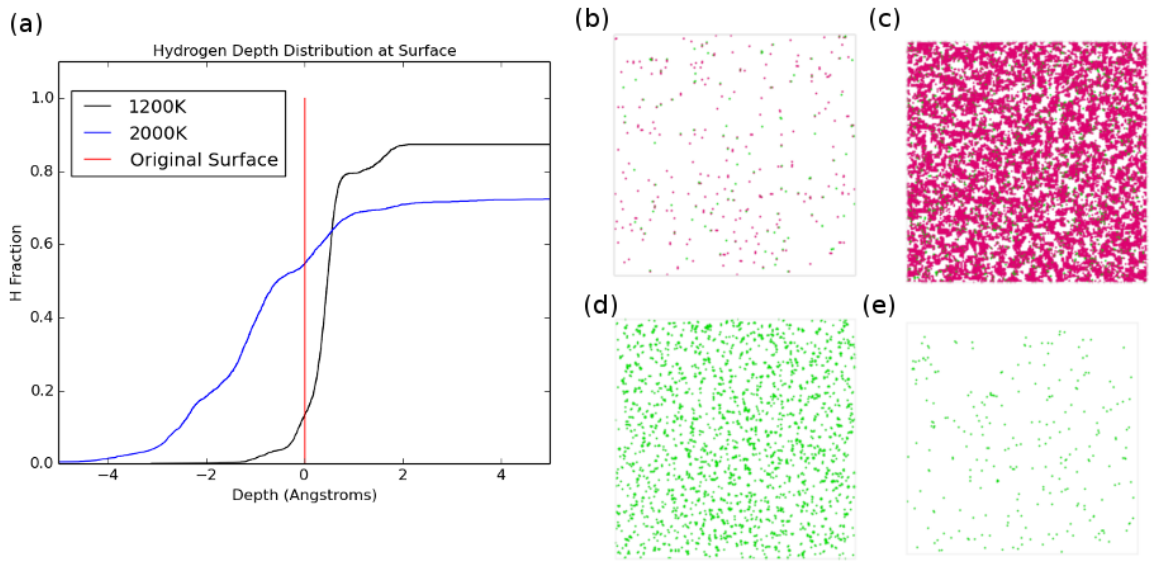

Figure 4.13: Snapshots of the hydrogen near the surface for both 1200 K and 2000 K at $1.5x10^{18}m^{-2}$ where (a) depicts a plot of the depth distribution for 1200 K and 2000 K as well as a line indicating the original surface. Atomistic snapshots just above the original surface for 1200 K and 2000 K are shown in (b) and (c) while snapshots between the surface and a depth of 2Åis shown in (d) and (e) for 1200 K and 2000 K respectively. Green and magenta atoms depict hydrogen and tungsten adatoms respectively.

modified from the pure tungsten case shown in Fig. 4.14(c). For the pure tungsten case, the hydrogen mostly remains near the surface with the remaing hydrogen more or less evenly distributed below the surface, as discussed previously. When helium is present, the hydrogen appears to diffuse bit further below the surface in a thicker layer which corresponds with the helium bubble layer just below the surface. The hydrogen appears to be segregating to the helium bubbles, as previously observed in section 4.2 for small sub-surface mixed hydrogen-helium bubbles. In addition, this behavior is consistent for both of the W-H potentials used, indicating that the synergestic behavior between hydrogen and helium is not an artifact of any single interatomic potential.

These qualitative observations are further confirmed by the cummulative hydrogen depth distribution. A strong tendency for hydrogen surface saturation had previously been observed in which the implanted hydrogen diffuses back to the incident surface. That behavior is also observed with helium pre-implantation, although depending on the interatomic potential, the surface segregation behavior is quantitatively different. In the pure tungsten case, about 80% of the hydrogen is located within 5 $\mathring{A}$ of the surface and the rest of the hydrogen atoms are more or less evenly distributed up to 60 $\mathring{A}$. For the helium pre-implanted case, there are a few hydrogen at the surface but a large portion, about 60% for the Tersoff case and 80% of the EAM case, are located between about 5 and 20 $\mathring{A}$. In addition, virtually no hydrogen atoms are observed to diffuse deeper into the material compared to the pure tungsten case where 20% of the atoms diffuse deeper. In fact, only about 5 hydrogen atoms have diffused past the helium bubble layer with the Tersoff potential while 11 atoms have diffused beyond the helium cluster/bubble latyer using the EAM potential. The depth distribution between the Tersoff and EAM track each other but the depth distribution seems to be shifted to a slightly deeper depth with the EAM potential and there appears to be a portion of hydrogen directly at the surface for the Tersoff potential. In either case, there is clearly a modified hydrogen depth distribution in the presence of helium below the tungsten surface.

A cluster analysis was performed to assess the amount of hydrogen that associates with helium as well as the type of H-He-V complexes that form. Atomistic snapshots of select H-He-V figures are shown in figure 4.15, in which (a), (b), (c), and (d) consist of $He_1 3H_1 V_1 0$, $He_4 H_3 V_2$, $He_6 H_1 V_0$, and $He_1 4H_1 V_5$, respectively. This analysis used a cutoff distance of 3 Å, such that any atoms that are within this distance are considered to be in the same cluster. It was found that 37.5% of the hydrogen atoms with the Tersoff potential at a fluence of $2.8x10^{17} m^{-2}$ were clustered with helium atoms, while the remainder of the hydrogen consisting predominately of individual hydrogen atoms within the material and a few dimers. For the EAM potential, an even larger portion of the hydrogen, about 60%, was clustered with helium. In contrast, only about 15% of the hydrogen atoms in the pure tungsten case were clustered with other hydrogen atoms and 85% remained as isolated hydrogen atoms within the material. Most of the

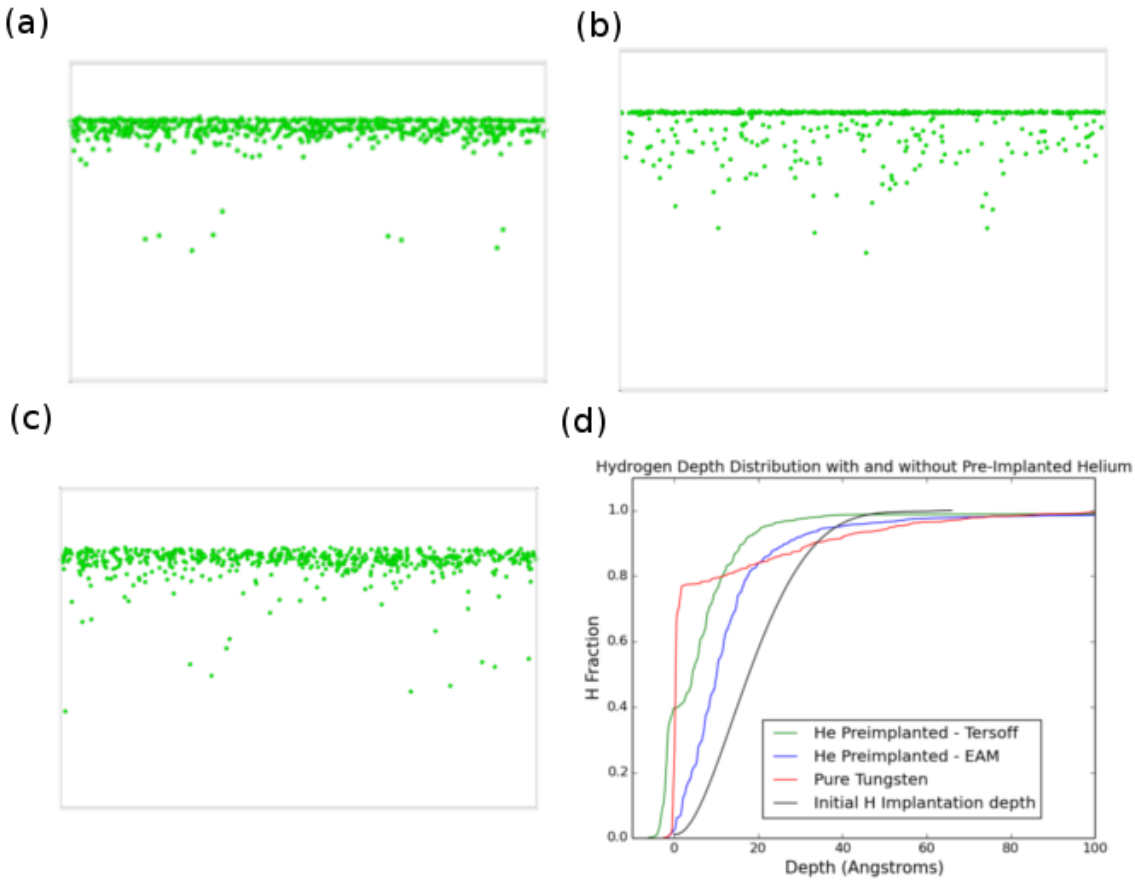

Figure 4.14: Atomistic snapshots of the hydrogen depth distributions at a fluence of $2.8x10^{17}m^{-2}$ for (a) helium pre-irradiated tungsten and the Tersoff potential, (b) pure tungsten and the Tersoff potential, and (c) helium pre-irradiated tungsten and the EAM potential. Part (d) depicts the hydrogen depth distribution for all three cases as well as the initial hydrogen implantation profile calculated by SRIM.

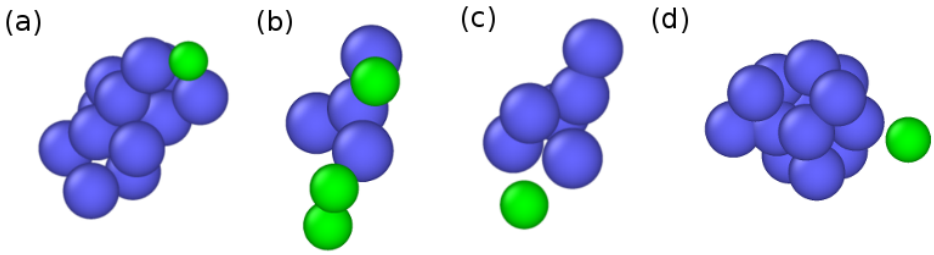

Figure 4.15: Atomistic snapshots of a few of the hydrogen-helium clusters present in the helium pre-implanted simulations. Each complex is described as: (a) $He_1 3 H_1 V_1 0$, (b) $He_4 H_3 V_2$, (c) $He_6 H_1 V_0$, and (d) $He_1 4 H_1 V_5$,

clusters had 2 or 3 hydrogen atoms and were fairly close to the surface. This indicates that again, a large portion of the hydrogen atoms are attracted to the helium bubbles and that hydrogen will cluster with other gas atoms more frequently when there is helium present. For both cases, most of the hydrogen atoms are at the edge of the helium bubbles, quite similarly to the results discussed in section 4.2. This is fairly consistent with the previous simulations where hydrogen was initially placed throughout the matrix. In those cases, about 25-45% of the hydrogen segregated to the bubble periphery while the remaining hydrogen diffused to the top and bottom surfaces. In these large-scale simulation, the percentage of hydrogen observed to cluster around helium bubbles are consistent with the earlier simulation while the rest of the hydrogen is located at the top surface. In the large-scale case, none of the hydrogen has yet diffused to the bottom surface but this most likely due to the greater distance to the bottom surface as well as the layer of helium bubbles, in addition to the limited simulation time accumulated to date.

Selected molecular statics calculations have been performed to assess the binding energy for some of the He-H-V complexes observed in this MD simulation. The results are presented in table 4.1. To perform this quantification, the cluster positions from the large-scale simulations were extracted and the cluster is placed in a clean tungsten cell. The energy is then calculated for the hydrogen near the complex and far away from the complex. The binding energy is then just the difference between the two values, with a positive binding energy indicated a bound configuration. For this analysis, four clusters observed from simulations performed with the Tersoff and EAM potentials were identified and their respective binding energies are tabulated here for both of the interatomic potentials. For the cases shown here, there are both strongly and weakly bound clusters with binding energies from 0.25 to 1.71 eV. Some of the binding energies are consistent with those calculated in the previous section on mixed subsurface He-H bubbles while most are much lower, less than 1 eV. In general, the Tersoff potential has a higher binding energy than then EAM potential for similar clusters, especially for clusters identified using the Tersoff potential. All the binding energies for the EAM potential calculated here are less than 1 eV. Within

Table 4.1: Table of binding energies for hydrogen at small H-He-V clusters observed in the simulation results presented in 4.15, with the binding energey identified using each interatomic potential.

Hydrogen Binding Energies to Small Clusters		
Cluster Identified Using Tersoff		
Configuration	Tersoff Binding Energy (eV)	EAM Binding Energy (eV)
$He_{40}H_2V_{23}$	0.26	0.25
$He_{16}H_1V_3$	1.71	0.32
$He_{11}H_1V_1$	1.11	0.82
$He_4H_1V_1$	1.48	0.79
Clusters Identified Using EAM		
Configuration	Tersoff Binding Energy (eV)	EAM Binding Energy (eV)
$He_{145}H_1V_{23}$	0.31	0.86
$He_{20}H_1V_4$	1.12	0.93
$He_{19}H_1V_3$	0.63	0.94
$He_9H_1V_1$	0.67	0.28

this analysis, no clear trend has been identified with respect to the dependence of the helium content on binding energy. Overall, the binding energies calculated using implanted hydrogen are much lower than for the subsurface bubble simulations which likely indicate that the helium-vacancy cluster or bubble configuration influences the binding energy, especially since the size of the helium bubbles are much smaller here.

A second case where a layer of hydrogen was implanted below the pre-implanted helium cluster/bubble layer was also simulated and the results are discussed here. Figure 4.16 shows snapshots 1 ns after implanting the initial hydrogen concentration where (a) shows the initial configuration, (b) shows the results with the Tersoff potential, and (c) shows the results with the EAM potential. It is clear that there is a much larger diffusional spreading of the hydrogen layer in the simulation using the EAM potential, indicating that there is much greater hydrogen diffusion predicted by EAM. The hydrogen in the Tersoff case does exhibit diffusional spreading but with a lower effective diffusion coefficient with the hydrogen largely remaining near the initial implantation region. After 1 ns, the spread of the hydrogen in the Tersoff case is between 7.4 nm and 12.6 nm while it is between 4.7 and 15 nm with the EAM potential which further confirms the difference in diffusion. Limited hydrogen clustering with helium has been observed mainly since the hydrogen has not fully reached the helium layer yet. In either case, none of the hydrogen diffuses through the helium bubble layer or reaches the top or bottom surface. However, the simulation time is very short, only 1 ns, and extending the results to larger time steps will allow more time for hydrogen to diffuse further.

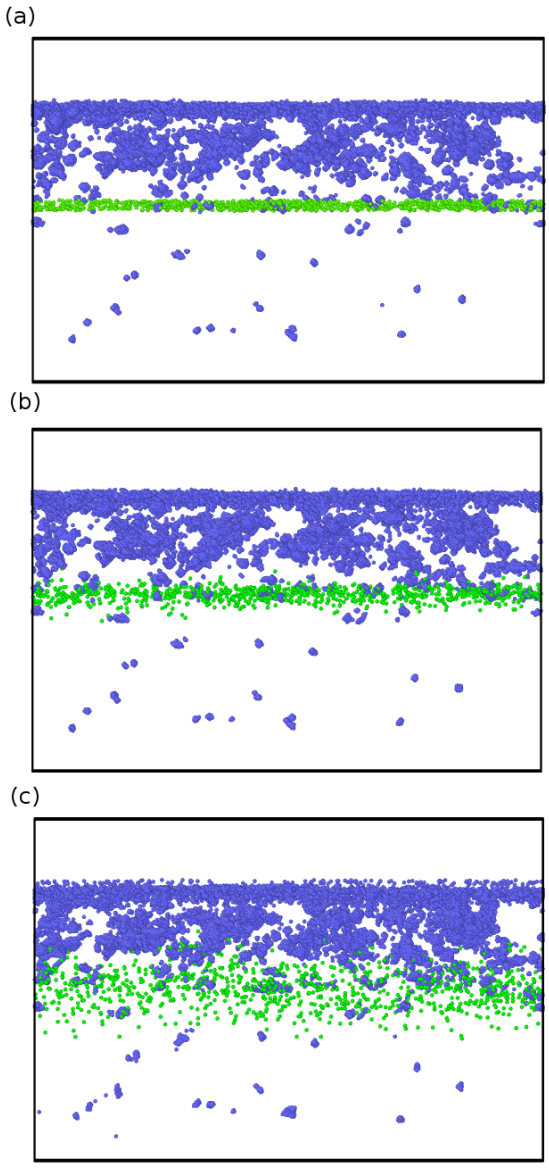

Figure 4.16: Atomistic snapshots from the second case in helium pre-implanted tungsten where an initial layer of hydrogen is implanted under the layer of helium bubbles, as shown in (a). Images at 1 ns for (b) Tersoff and (c) EAM potential are shown. Blue and green atoms represent helium and hydrogen respectively.

The diffusion as a function of distance and time has been quantified and is shown in Fig. 4.17 for both the (a) Tersoff and (b) EAM potential. The hydrogen spread was divided into 1 nm slices of up to 6 nm in the positive and negative z direction from the initial implantation layer. The concentration in H/m^3 was calculated for each 1 nm slice as a function of time from 0 ns to 1 nm in 0.1 ns increments. Figure 4.17 corroborates the visual observations, namely that there is much greater diffusion with the EAM potential then the Tersoff potential. The concentration in the implantation region only decreases from the initial concentration of $4x10^{26}H/m^3$ by about $1x10^{26}H/nm3$ for the Tersoff potential with a larger decrease of $3x10^{26}H/m^3$ observed using the EAM potential. The shape of the concentration profile mostly remains the same with the Tersoff potential with just a bit wider spread. For the EAM potential, the initially sharp concentration profile peak greatly decreases and spreads such that there is no longer a distinct peak.

Another method to quantify the diffusion was to calculate the average mean square displacement of hydrogen in the z direction. Figure 4.18 shows the average mean squared displacement of hydrogen calculated from the MD simulations using the Tersoff and EAM potentials from 0 ns to 1 ns at 0.1 ns increments. Again, the results here indicate that there is much greater diffusion with the EAM potential. After 1 ns, the mean squared displacement for the EAM potential is 3.8 nm^2 while it is only 0.5 nm^2 for the Tersoff potential. A linear fit to the MSD data are also shown in figure 4.18 and indicate that the mean squared displacement increases much more rapidly with the EAM than with the Tersoff potential.

The diffusion coefficient can be quantified from both the concentration and mean squared displacement analysis. From the concentration profiles, a 1D diffusion approximation for a slab geometry can be used to solve for the diffusion coefficient. This yields a diffusion coefficient of $9.8x10^{-7}m^2s^{-1}$ for the Tersoff potential and $4.9x10^{-6}m^2s^{-1}$ for the EAM potential. From the mean squared displacment data, the slope of the plot of mean squre displacement as a function of time yields the diffusion coefficient. This analysis results in a diffusion coefficeint of $4.0x10^{-9}m^2s^{-1}$ for the Tersoff potential and $4.0x10^{-7}m^2s^{-1}$ for the EAM potential. This can be compared with the Arrhenius relationship using the activation energy and pre-factor calculated using the potential itself. The activation energy for hydrogen diffusion predicted by the Tersoff and EAM potential is 0.35 eV and 0.23 eV, respectively, and the pre-factor is $3.9x10^{-8}m^2s^{-1}$ and $5.3x10^{-8}m^2s^{-1}$, respectively. This results in a diffusion coefficient of $5.7x10^{-10}m^2s^{-1}$ for the Tersoff potential and $3.0x10^{-9}m^2s^{-1}$ for the EAM potential. While the diffusion coefficients vary depending on the method, each assessment agrees that a higher diffusion coefficient with the EAM potential that differs by about an order of magnitude or two. In fact, the the lower activation energy for the EAM potential, which is about 30% lower than the Tersoff potential, explains the much greater diffusion observed with this potential.

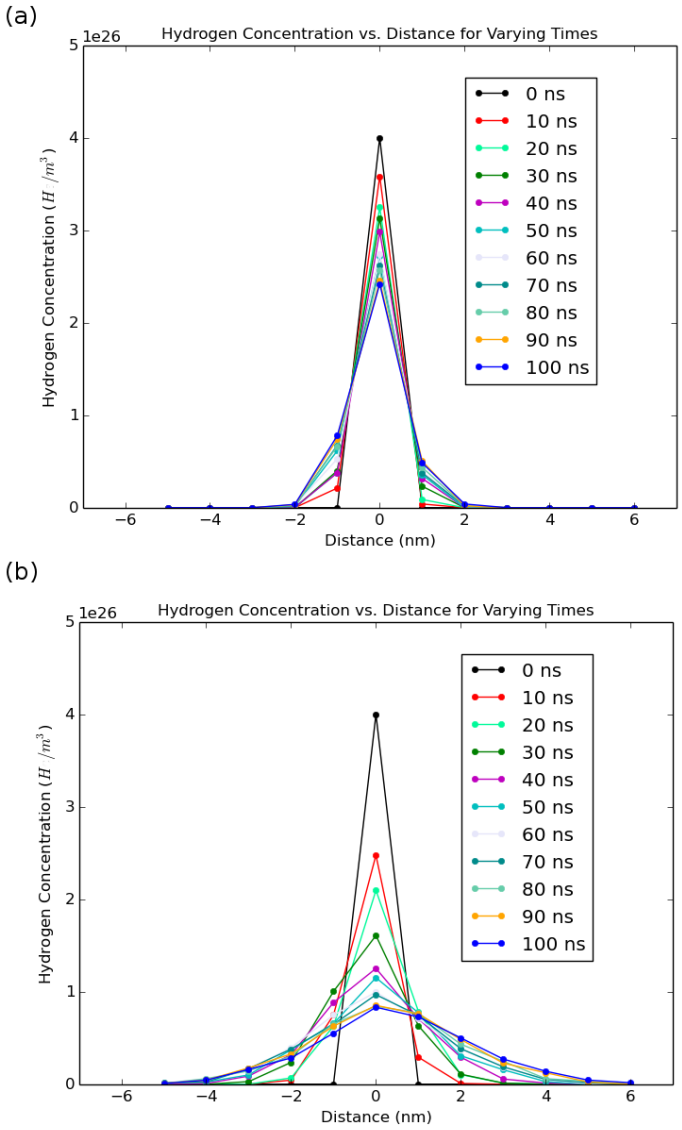

Figure 4.17: Concentration as a function of distance from the implantation layer in the z direction for various times. Results from the (a) Tersoff and (b) EAM potential are shown.

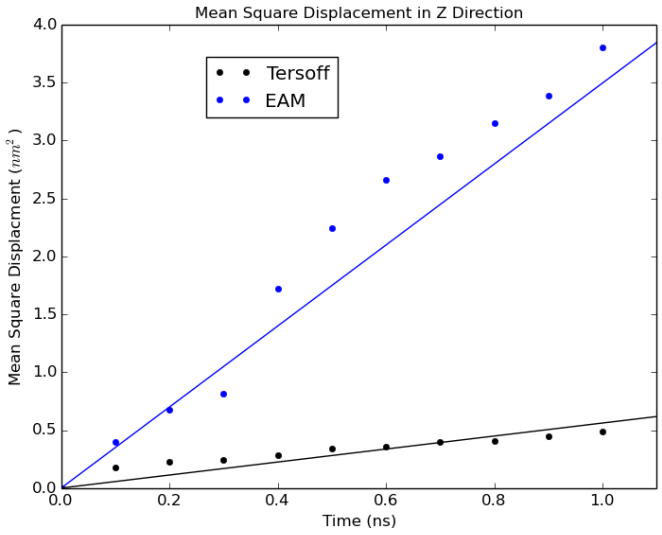

Figure 4.18: Mean squared displacment plotted as a function of time including a line of best fit. The black and blue lines represent the Tersoff and EAM potential respectively.

A cluster analysis has also been performed from this set of simulations. The same method previously described for the hydrogen implantation cases has been used here. As just noted, the relatively short simulated time of 1 ns results in limited hydrogen diffusion without the hydrogen fully reaching the region containing the largest helium bubbles. Thus, the amount of hydrogen that clusters with helium is much less, with only about 3.7% and 12.6% of the hydrogen inventory has formed cluster complexes with helium using the Tersoff and EAM potentials, respectively. However, the same trend of more clustering with the EAM potenial is found here. This may be influenced by the higher hydrogen diffusivity using the EAM potential which will expose those hydrogen atoms to more helium bubbles. Figure 4.19 depicts a few specific clusters where (a), (b), (c), and (d) depects $He_3H_1V_0$, $He_7H_1V_1$, $He_8H_1V_2$, and $He_7H_4V_1$, respectively. The binding energies are also quantified using the same method previously described for the hydrogen implantation simulations. Table 4.2 shows the binding energy for a variety of clusters and each complex is calculated using both potentials. Again, the clusters observed from the MD simulations with the Tersoff potential exhibit generally higher hydrogen binding energies than the ones found and calculated with the EAM potential. The binding energies are fairly comparable and maybe a bit lower than those calculated for the implantation case.

Hydrogen has been observed to cluster with helium clusters, or bubbles, using three distinct MD simulation methods that involved modeling sub-surface mixed H-He bubble, implanting a flux of hydrogen into a simulation with pre-existing helium bubbles, or implanting a layer of hydrogen beneath a layer of pre-existing helium

bubbles. This behavior also appears to be independent of potential as indicated by the consistent results for the latter two methods. This could potentially have a significant impact on hydrogen, and therefore tritium, retention in tungsten especially since helium bubbles will be present in the divertor of a fusion reactor.

4.3.3 Conclusions

Large-scale simulations of hydrogen implantation in pure tungsten and helium pre-implanted tungsten have been performed. For the case of pure tungsten, the hydrogen behaves much differently than helium implanted below tungsten surfaces. A large portion, roughly 80% of the hydrogen inventory resides at the surface. Depending on temperature, the hydrogen is either directly at the surface or slightly above the original surface for 1200 K and 2000 K respectively. The rest of the hydrogen diffuses deeper into the material, with a significant amount of hydrogen reaching the bottom of the simulation cell at 2000 K. Unlike helium, the hydrogen does not cluster, with 85% of the hydrogen remaining as isolated monomers within the material. The remaining hydrogen consisted of hydrogen molecules and were mostly located at or near the surface.

Two cases involving helium pre-implanted tungsten were performed using both a Tersoff and EAM style W-H potential. The first case involved hydrogen implantation at a flux of $4x10^{25}m^{-2}s^{-1}$. When helium was included in the simulation, the hydrogen depth distribution and clustering were modified. With an initial distribution of helium-vacancy clusters, in addition to larger helium bubbles present, the hydrogen tends to diffuse to and segregate around the helium bubble layer. Roughly 60% and 80% of the hydrogen was located near the helium bubble layer for the Tersoff and EAM potentials, respectively. Similar behavior for two different styles of potentials suggests that this is not an artifact of the potential itelf. Performing a cluster analysis on the two different simulations indicates that about 37% and 60% of the hydrogen in the Tersoff and EAM simulations were clustered with helium. This is a significant amount, especially in the EAM case, and may indicate that the preference for hydrogen to be clustered with other helium atoms could indeed be an important mechanism associated with the role of helium in hydrogen blister suppression. A large portion of the hydrogen atoms were located less than 2 nm from the surface, and very few hydrogen atoms had migrated past the bubble layer, further suggesting that the helium bubble layer may indeed block diffusion of hydrogen deeper into the material. Although it is important to note that these simulations have only accumulated 6 ns.

The second set of simulations involved implanting a layer of hydrogen beneath the helium bubble layer and allowing the hydrogen to diffuse without any further implantation. This simulation also compared the two different W-H potentials. Simulations reached a time of 1 ns and at this point in time, there is rather limited

Table 4.2: Table of binding energies for hydrogen at small H-He-V clusters

Hydrogen Binding Energies to Small Clusters		
Cluster Identified Using Tersoff		
Configuration	Tersoff Binding Energy (eV)	EAM Binding Energy (eV)
$He_3H_1V_0$	0.67	0.83
$He_7H_1V_1$	1.09	0.92
Clusters Identified Using EAM		
Configuration	Tersoff Binding Energy (eV)	EAM Binding Energy (eV)
$He_8H_1V_2$	0.16	0.42
$He_7H_4V_1$	0.13	0.09

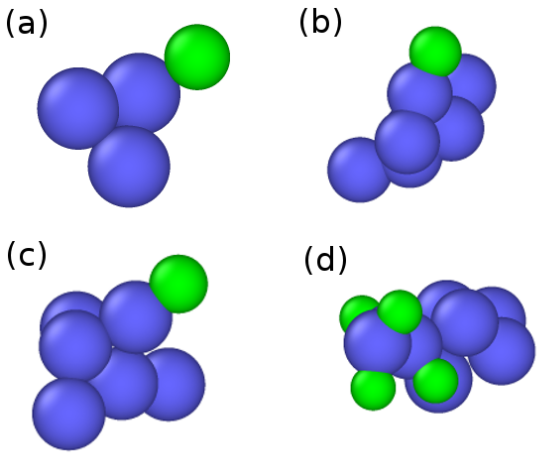

Figure 4.19: Atomistic snapshots of H-He clusters for the second case where hydrogen is implanted in a layer below the pre-implanted helium players. Different complexes of $He_3H_1V_0$, $He_7H_1V_1$, $He_8H_1V_2$, and $He_7H_4V_1$ are shown in (a), (b), (c), and (d).

diffusion of hydrogen away from the implanted layer. The diffusion is much more pronounced in the EAM case, where the mean squared displacement in the z direction is about 3.8 nm^2 for the EAM potential but only 0.5 nm^2 for the Tersoff potential. The hydrogen diffusion coefficient was calculated using the concentration profile, the mean squared displacment, and an Arrhenius analysis from the parameters directly calculated by the potential. While the diffusion coefficient varies depending on the method, a common trend is that the diffusion coefficient using the EAM potential is at least an order of magnitude higher than for the Tersoff potential. This is most likely due to the lower hydrogen migration energy for the EAM potential.

The hydrogen binding energy for select helium-vacancy clusters from both cases were calculated. The binding energies tend to be between 0.1 and 1.7 eV, which is slightly lower than the 2 eV binding energy calculated in the mixed hydrogen-helium sub-surface bubble simulations. In general, the binding energies calculated using the Tersoff potential tend to be slighly higher than those calculated with the EAM potential. The variety of binding energies calculated for the different complexes indicates that the hydrogen binding energy may depend on number of helium atoms and vacancies in the complex itself.

While these results present interesting behavior for hydrogen implantation near helium bubbles, these simulations were only run to very low fluences and very short times due to the limitations in computational power and slow performance of the hydrogen potentials. Additional work will be needed to see if this behavior continues for longer periods of time or if, for example, the hydrogen trapping at helium bubbles saturates or the hydrogen detraps from the helium bubbles. The faster run times for the new EAM potential may help in extending these simulations for a longer period of time. Lastly, while the two different potentials provided similar results, it will be important to develop potentials that have been fit to additional DFT data for both hydrogen behavior at surfaces and near other helium atoms. Many of the binding energies calculated for the small clusters can be calculated and compared with DFT in order to validate the values obtained in this work.

Chapter 5

Summary and Conclusions

The study of plasma material interactions is a challenging but critically important area of fusion research that is necessary to create a sustainable fusion reactor in the future. With the complex material damage that will affect reactor performance and material lifetime, it is important to include modeling, such as MD, that can provide information on physical mechanisms that can be used in designing materials that mitigate damage and enhance performance under fusion relevant conditions. Experiments have shown us the various types of damage, such as bubbles, blisters, and nanofuzz, while MD has provided insight into the physical processes that can lead to this damage, such as trap mutation, dislocation loop punching, and adatom formations on the surface. This work has begun to expand our knowledge of hydrogen and helium interactions in tungsten by addressing key unknowns in the experimental work using molecular dynamics simulations. The objectives of this thesis was to understand the diffusion behavior of helium near defects like nanotendrils and grain boundaries as well as investigating the interaction between hydrogen and helium in tungsten.

The first half of this work described helium behavior near defects. Experiments have shown nanotendrils form on the surface of tungsten under helium irradiation in plasma-like conditions. Therefore, MD simulations were designed to investigate helium diffusional behavior and evolution upon implantation into a tendril-like geometry. The MD simulations revealed that that the tendril structures are stable at temperatures between 1200 K and 2000 K. Large bubbles form within the tendril close to the implantation depth, consistent with previous MD simulations of helium implantation on planar surface. The simulations also reveal very limited surface deformation or evolution within the tendril and that the helium bubbles continually release helium without significant bubble rupture and crater formation. The helium retention eventually reached an approximately constant value where as much helium was being released from the tendril as was being implanted. A modified helium release

mechanism was identified where helium bubbles release excess pressure through small pinhole ruptures on the surface that rapidly self-heal. This is presumably due to the large surface to volume ratio of the tendrils as opposed to a planar surface. An inverse relationship that follows a power law was found between helium retention and the surface to volume ratio. In addition, an increase in temperature led to lower retention, larger bubble size before helium release, He/V ratio within the bubbles, and total number of bubbles within the tendril.

Observations at higher temperatures indicated that only a few helium atoms diffused more than 6 nm to reach the bottom of the tendril. Initially introducing helium bubbles near the bottom of the tendril resulted in increased diffusion of helium to the bottom of the tendril. Simulations with pre-existing helium bubbles near the top of the tendril did not greatly affect the deeper diffusion of helium since the helium bubbles act as a sink for helium that block deeper diffusion. Further studies were performed through large-scale modeling of long parallelepiped geometry with free surfaces and a distribution of heliums bubble initially present at one end of the parallelepiped. In this simulation, helium diffused much deeper into the material, up to 10 nm, which is most likely due to the lower flux that allows helium time to diffuse before helium self-trapping leads to significant helium-vacancy clustering and the formation of larger bubbles that block diffusion. However, in the large parallelepiped geometry the presence of pre-existing bubbles does not appears to significantly influence the diffusion or retention of helium. The flux of helium diffusing deeper into the parallelepiped geometry was quantified and extrapolated to longer times. The extrapolation suggests that very limited to non-existent helium diffusion past 7 nm to form new bubbles and drive tendril growth, much less to depths of 100-1000 nm.

The results of this work lead to the conclusion that helium diffusion is not significantly enough to explain the growth of tendrils up to microns in length. Further work in extrapolating the results obtained for small tendrils is needed. While studying helium implantation in small tendrils can lead to information on mechanisms and early stage tendril growth, ultimately information on experimentally relevant scales will be needed. One extrapolation that will be important to qunatify is the effect of flux. The high flux used in the small tendril simulation will make it difficult for helium to diffuse into the material because the helium is being implanted so quickly that helium bubbles form and trap the implanted helium before significant diffusion into the material. Studying the effects of implantation flux on diffusion and retention will therefore be important. Further studying the influence of surface to volume ratio on helium retention will also be of interest.

Additional simulations of helium implantation near defects were performed by modeling helium implantation near a $\sigma 3 < 111 > 121$ grain boundary but not directly on the grain boundary itself. The helium evolution in the implantation region, in

between the two grain boundaries, is comparable with previous simulations of helium implantation in defect-free tungsten. Large helium bubbles form in this region and typical surface deformation is observed due to bubble expansion. There is some diffusion of helium to the grain boundary but the concentration there is much lower than in the implantotion zone. The helium along the grain boundary form small clusters that are mostly less than 10 atoms in size. However, only two helium atoms have diffused across the grain boundary, indicating the significant trapping strength of this particular grain boundary. The flux of the helium to the grain boundary has been analyzed and indicates that the helium diffuses to the grain boundary early in the simulation before helium bubbles begin to form in the implantation region and blocks subsequent diffusion of helium. The trapping strengths were quantified and confirm that the sink strength of the grain boundary is very similar to the trapping strength of the bubbles that form in the implantation zone. Early in the simulation, the grain boundary sink strength is higher and therefore plays a more significant role. However, as helium bubbles begin to form, the bubble sink strength increases and dominates at later times. These results will be used in benchmarking the continuum reaction-diffusion cluster dynamics code Xolotl. Similar simulations and analysis will be performed in Xolotl and compared with the MD results.

The second half of this work addressed the synergestic behavior of hydrogen and helium in tungsten. Small sub-surface mixed hydrogen-helium bubbles were modeled and it was discovered that hydrogen segregated to the periphery of high pressure bubbles following the initial distributions of various concentrations of helium and hydrogen throughout a sub-surface cavity 1 nm in radius and 3 nm below. Roughly 75-90% of the hydrogen was located near the bubble periphery while typically less than 20% remained within the bubble. This was observed for all simulations independent of initial gas atom concentrations, surface orientation, temperature, or initial placement of hydrogen within the simulation cell. The potential energy landscape of the hydrogen in proximity to the helium bubbles was evaluated via molecular statics, resulting in a calculated binding energy of 2 ± 0.6 eV. This indicates that even at high temperatures, hydrogen atoms could still remain bound at helium bubbles, which is a concern in regards to tritium retention.

Further investigation of this W-He-H synergy was performed using large-scale simulations of hydrogen implantation in slabs of both pure tungsten and helium pre-implanted tungsten. Two different cases were performed for helium pre-implanted tungsten, one in which 60 eV hydrogen was implanted into the He pre-implanted tungsten slab every 10 ps and one where a layer of hydrogen with a concentration of $4x10^{26} H/m^3$ was introduced below the helium bubble layer. In the pure tungsten simulation, about 80% of the hydrogen remains at the surface while the rest of the hydrogen diffuses deep into the bulk, unlike helium which self-traps and therefore remains near its implantation depth. In the MD simulation of hydrogen implantation into helium pre-implanted tungsten, the hydrogen was observed to cluster around the

near-surface layer of helium bubbles as opposed to the surface itself. In addition, only a few hydrogen atoms have migrated past the bubble layer. This observation was common to both of the interatomic potentials tested, which further indicates the concern about hydrogen trapping at sub-surface helium bubbles. These results also indicate that the helium-hydrogen synergies that lead to hydrogen segregation and trapping at the bubble periphery can explain the reduced deuterium permeation and suppressed blister formation due to mixed helium-deuterium implantation observed in experiments. A large portion of the hydrogen, either 37.5% or 60% depending on the potential used, clusters with helium clusters or bubbles. The binding energies range from about 0.2 eV to 1.5 eV depending on the content of gas atoms in the cluster. This indicates that the hydrogen binding energy will depend on the size and configuration of the helium-vacancy cluster.

The second case involves an initial hydrogen layer simulated for a time of up to 1 ns to assess hydrogen diffusion with both the Tersoff and EAM potential. Visual inspection suggests that the hydrogen diffuses much more with the EAM potential. This is confirmed by analzying the concentration profile over time as well as the mean squared displacement, which confirm that hydrogen is much more mobile with the EAM potential. This is likely due to the lower migration energy of 0.23 eV for the EAM potential compared to 0.35 eV for the Tersoff potential. The resulting hdyrogen-helium clusters were also assessed from this set of simulations and, while a much lower amount of clustering was found, only about 3.7% or 12.6% of the total hydrogen depending on the potential; it is important to note the relatively short time simulated and the fact that the hydrogen has not yet reached the region containing larger helium bubbles. Similar hydrogen binding energies were obtained for H-He clusters observed with both potentials.

The results from the H-He modeling indicate that heluium bubbles can potentially trap a significant amount of hydrogen. This raises a huge concern for tritium retention and PFC performance. However, additional work needs to be performed to verify and further quantify these observations. A series of DFT calculations that quantify the binding energy for some of the clusters observed in the MD results would be beneficial in confirming the results obtained in this dissertation. Quantifying the volume the hydrogen occupies at the periphery as well as investigating the relationship between helium bubble size/pressure and hydrogen binding energy is also needed. Finally, simulations to achieve longer times will be needed in order to study whether this behavior continues over long periods of time or if the hydrogen evetually desorbs or the hydrogen trapping at the helium bubble layer saturates.

Overall this work has demonstrated the role of molecular dynamics simulations in understanding the synergestic interactions between helium and hydrogen below tungsten surfaces necessary to predict the performance of tungsten under plasma irradiation. Creating simulations with inital geometry and microstructures that are

closer to experiments can help to build databases for continuum codes and bridge the gap between the modeling and experimental work. The study of helium behavior in tendrils and interaction between hydrogen and helium in tungsten provide a foundation to build an understanding of the complex processes that will occur in the divertor region of future fusion reactors.

Bibliography

[1] NASA, "Global climate change: Vital signs of the planet." https://climate.nasa.gov/, 2017. Accessed: 23 May 2017.

[2] G. Federici, C. Skinner, J. Brooks, J. Coad, C. Grisolia, A. Hassz, A. Hassanein, V. Philipps, C. Pitcher, J. Roth, W. Wampler, and D. Whyte, "Plasma-material interactions in current tokamaks and their implications for the next step fusion reactors," *Nuclear Fusion*, vol. 41, no. 12, pp. 1967–2137, 2001.

[3] D. of Energy Office of Fusion Sciences, "Fusion energy science program: A ten-year perspective," 2015," 2015.

[4] R. A. Pitts, S. Carpenter, F. Escourbiac, T. Hirai, V. Komarov, S. Lisgo, A. S. Kukushkin, A. Loarte, M. Merola, A. S. Naik, R. Mitteau, M. Sugihara, B. Bazylev, and P. C. Stangeby, "A full tungsten divertor for iter: Physics issues and design status," *Journal of Nuclear Materials*, vol. 438, pp. S48–S56, 2013.

[5] T. J. Team, "Results of jet operation with beryllium," *Journal of Nuclear Materials*, vol. 176-177, pp. 3–13, 1990.

[6] W. R. Wampler, B. LamBombard, B. Lipschultz, G. M. McCracken, D. A. Pappas, and C. S. Pitcher, "Molybdenum erosion measurements in alcator c-mod," *Journal of Nuclear Materials*, vol. 266-269, pp. 217–221, 1999.

[7] K. Krieger, H. Maier, R. Neu, and A. U. Team, "Conclusions about the use of tungsten in the divertor of asdex upgrade," *Journal of Nuclear Materials*, vol. 266-269, p. 207, 1999.

[8] H. Iwakiri, K. Yasunaga, K. Morishita, and N. Yoshida, "Microsturcture evolution in tungsten during low-energy helium ion irradiation," *Journal of Nuclear Materials*, vol. 238-287, pp. 1134–1138, 2000.

[9] S. Kajita, W. Sakaguchi, N. Ohno, N. Yoshida, and T. Saeki, "Formation process of tungsten nanostructure by the exposure of helium plasma under fusion relevant plasma conditions," *Nuclear Fusion*, vol. 49, p. 095005, 2009.

[10] D. Nishijima, M. Y. Ye, N. Ohno, and S. Takamura, "Formation mechanism of bubbles and holes on tungsten surface with low-energy and high-flux helium plasma irradiation in nagdis-ii," *Journal of Nuclear Materials*, vol. 329-333, pp. 1029–1033, 2004.

[11] M. J. Baldwin, T. C. Lynch, R. P. Doerner, and J. H. Yu, "Nanostructure formation on tungsten exposed to low-pressure rf helium plasmas: A study of ion energy thereshold and early stage growth," *Journal of Nuclear Materials*, vol. 415, pp. S104–S107, 2011.

[12] M. J. Baldwin and R. P. Doerner, "Helium induced nanoscopic morphology on tugnsten under fusion relevant plasma conditions," *Nuclear Fusion*, vol. 48, pp. 1–5, 2008.

[13] S. Takamura, N. Ohno, D. Nishijima, and S. Kajita, "Formation of nanostructured tungsten with arborescent shape due to helium plasma irradiation," *Plasma and Fusion Research*, vol. 1, p. 51, 2006.

[14] G. M. Wright, D. Brunner, M. J. Baldwin, R. P. Doerner, B. Labombard, B. Lipschultz, J. L. Terry, and D. G. Whyte, "Tungsten nano-tendril growth in the alcator c-mod divertor," *Nuclear Fusion*, vol. 52, no. 4, p. 042003, 2012.

[15] A. Haasz, M. Poon, and J. Davies, "The effect of ion damage on deuterium trapping in tungsten," *Journal of Nuclear Materials*, vol. 266-269, pp. 520–525, 1999.

[16] R. Causey, "Hydrogen isotope retention and recycling in fusion reactor plasma-facing components," *Journal of Nuclear Materials*, vol. 300, pp. 91–117, 2002.

[17] Y. Ueda, M. Fukumoto, J. Yoshida, Y. Ohtsuka, R. Akiyoshi, H. Iwakiri, and N. Yoshida, "Simultaneous irradiation effects of hydrogen and helium ions on tungsten," *Journal of Nuclear Materials*, vol. 386-388, pp. 725–728, 2009.

[18] O. V. Ogorodnikova, T. Schwarz-Selinger, K. Sugiyama, and V. K. Alimov, "Deuterium retention in tungsten exposed to low-energy pure and helium-seeded deuterium plasmas," *Journal of Applied Physics*, vol. 109, p. 013309, 2011.

[19] B. D. Wirth, K. Nordlund, D. G. Whyte, and D. Xu, "Fusion materials modeling: challenges and opportunities," *MRS Bulletin*, vol. 36, p. 216, 2011.

[20] F. Maury, M. Biget, P. Vajda, A. Lucasson, and P. Lucasson, "Frenkel pair creation and stage i recovery in w crystals irradated near threshold," *Radiation Effects and Defects in Solids*, vol. 1-2, pp. 53–65, 1978.

[21] G. Was, *Fundamentals of Radiation Materials Science*. Berlin Heidelberg: Springer, 2007.

[22] W. Eckstein and J. Laszlo, "Sputtering of tungsten and moybdenum," *Journal of Nuclear Materials*, vol. 183, pp. 19–24, 1991.

[23] D. Perez, T. Vogel, and B. Uberuaga, "Diffusion and transformation kinetics of small helium clusters in bulk tungsten," *Physical Review B*, vol. 90, p. 014102, 2014.

[24] R. Frauenfelder, "Solution and diffusion of hydrogen in tungsten," *Journal of Vacuum Science Technology*, vol. 6, p. 388, 1969.

[25] W. Wolfer, "The pressure for dislocation loop punching by a single buble," *Philosophical Magazine A*, vol. 58, pp. 285–297, 1988.

[26] A. M. Ito, Y. Yoshimoto, S. Saito, A. Takayama, and H. Nakamura, "Molecular dynamics simulation of a helium bubble bursting on tungsten surfaces," *Physica Scripta*, vol. T159, p. 014062, 2014.

[27] F. Sefta, K. D. Hammond, N. Juslin, and B. D. Wirth, "Tungsten surface evolution by helium bubble nucleation, growth, and rupture," *Nuclear Fusion*, vol. 53, pp. 1–7, 2013.

[28] F. Sefta, N. Juslin, and B. D. Wirth, "Helium bubble bursting in tungsten," *Journal of Applied Physics*, vol. 113, p. 243518, 2013.

[29] H. Bolt, V. Barabash, S. Krauss, J. Linke, R. Neu, S. Suzuki, N. Yoshida, and A. U. Team, "Materials for the plasma-facing components of fusion reactors," *Journal of Nuclear Materials*, vol. 329-333, pp. 66–73, 2004.

[30] H. Wurz, B. Bazylev, I. Landman, S. Pestchanyi, and V. Safronov, "Macroscopic erosion of divertor and first wall armour in future tokamaks," *Journal of Nuclear Materials*, vol. 307-311, pp. 60–68, 2002.

[31] D. Nishijima, M. Miyamoto, H. Iwakiri, M. Ye, N. Ohono, K. Tokunaga, N. Yoshida, and S. Takamura, "Micron-bubble formation on polycrystal tungsten due to low-energy and high-flux helium plasma exposure," *Materials Transactions*, vol. 46, p. 561, 2005.

[32] V. Philipps, "Tungsten as material for plasma-facing components in fusion devices," *Journal of Nuclear Materials*, vol. 415, pp. S2–S9, 2011.

[33] J. Roth and K. Schmid, "Hydrogen in tungsten as plasma-facing material," *Physuca Scripta*, vol. T145, p. 014031, 2011.

[34] A. Kallenbach, R. Neu, R. Dux, H. U. Fahrbach, J. C. Fuchs, L. Diannone, O. Gruber, A. Herrmann, B. Lipschults, P. T. Lang, C. F. Maggi, J. Neuhauser, V. Philipps, T. Putterich, V. Rohde, J. Roth, G. Sergienko, and A. Sips, "Tokamoa operation with high-z plasma facing components," *Plasma Physics and Controlled Fusion*, vol. 47, pp. B207–B222, 2005.

[35] B. Lipschultz, D. A. Pappas, B. Lambombard, J. E. Rice, D. Smith, and S. J. Wukitch, "A study of molybdenum influxes and transport in alcator c-mod," *Nuclear Fusion*, vol. 41, pp. 585–596, 2001.

[36] V. Borovikov, A. F. Voter, and X. Z. Tang, "Reflection and implantation of low energy helium with tungsten surfaces," *Journal of Nuclear Materials*, vol. 447, pp. 254–270, 2014.

[37] K. D. Hammond and B. D. Wirth, "Crystal orientation effects on helium ion depth distributions and adatom formation processes in plasma-facing tungsten," *Journal of Applied Physics*, vol. 114, p. 143301, 2014.

[38] L. Hu, K. D. Hammond, B. D. Wirth, and D. Maroudas, "Molecular-dynamics analysis of mobile helium cluster reactons near surfaces of plasma-exposed tungsten," *Journal of Applied Physics*, vol. 118, p. 163301, 2015.

[39] S. Kajita, S. Takamura, N. Ohno, D. Nishijima, H. Iwakiri, and N. Yoshida, "Sub-ms laser pulse irradiation on tungsten target damaged by exposure to helium plasma," *Nuclear Fusion*, vol. 47, pp. 1358–1366, 2007.

[40] A. Lasa, S. Tahtinen, and K. Nordlund, "Loop punching and bubble rupture causing surface roughening-a model for w fuzz growth," *Europhysics Letters*, vol. 105, p. 25002, 2014.

[41] T. J. Petty, M. J. Baldwin, M. I. Hasan, R. P. Doerner, and J. W. Bradley, "Tungsten "fuzz" growth re-examined: the dependence on ion fluence in non-erosive and erosive helium plasma," *Nuclear Fusion*, vol. 55, p. 093033, 2015.

[42] S. Kajita, N. Yoshida, R. Yoshihara, N. Ohno, and M. Yamagiwa, "Tem observation of growth process of helium nanobubbles on tungsten: Nanostructure formation mechanism," *Journal of Nuclear Materials*, vol. 418, pp. 152–158, 2015.

[43] M. J. Baldwin, R. P. Doerner, D. Nishijima, K. Tokunaga, and Y. Ueda, "The effects of high fluence mixed-species (deuterium, helium, beryllium) plasma interactions with tungsten," *Journal of Nuclear Materials*, vol. 390-391, pp. 886–890, 2009.

[44] C. M. Parish, H. Hijazi, H. M. Meyer, and F. W. Meyer, "Effect of tungsten crystallographic orientation on he-ion-induced surface morphology changes," *Acta Materialia*, vol. 62, pp. 173–181, 2014.

[45] J. Cui, M. Li, J. Wang, and Q. Hou, "Molecular dynamics study of helium bubble pressure in tungsten," *Nuclear Instruments and Methods in Physics Research Section B: Beam Interactions with Materials and Atoms*, vol. 352, pp. 104–106, 2015.

[46] H. B. Zhou, Y. Li, and G. H. Lu, "Modeling and simulation of helium behavior in tungsten: a first principles investigation," *Computational Materials Science*, vol. 112, pp. 487–491, 2016.

[47] X. C. Li, X. Shu, P. Tao, Y. Yu, G. J. Niu, Y. Xu, F. Gao, and G. N. Luo, "Molecular dynamics simulation of helium cluster diffusion and bubble formatio in bulk tungsten," *Journal of Nuclear Materials*, vol. 455, pp. 544–548, 2014.

[48] K. Umstadter, R. P. Doerner, and G. Tynan, "Enhanced erostion of tungsten plasma-facing components subject to simultaneous heat pulses and deuterium plasma," *Journal of Nuclear Materials*, vol. 386, pp. 751–755, 2009.

[49] K. W. Hill, M. Bitter, D. Eames, S. von Goeler, N. R. Sauthoff, and E. Silver, "Low energy x-ray emission from magnetic fusion plasmas," *AIP Conference Proceedings*, vol. 75, p. 8, 1982.

[50] S. Krasheninnikov, "Viscoelastic model of tungsten "fuzz" growth," *Physica Scripta*, vol. T145, p. 014040, 2011.

[51] Y. Martynenkov and M. Nagel, "Model of fuzz formation on a tungsten surface," *Plasma Physics Reports*, vol. 38, no. 12, pp. 996–999, 2012.

[52] ITER Organization, "Fueling the fusion reactor." www.iter.org/sci/fusionfuels, 2016. Accessed: 23 March 2016.

[53] K. O. E. Henriksson, K. Nordlund, A. Krasheninnikov, and J. Keinonen, "The depths of hydrogen and helium bubbles in tungsten: a comparison," *Fusion Science and Technology*, vol. 50, pp. 43–57, 2005.

[54] Y. L. Liu, Y. Zhang, H. B. Zhou, G. H. Lu, F. Li, and G. N. Luo, "Vacancy trapping mechanism for hydrogen bubble formation in metal," *Physical Review B*, vol. 79, p. 172103, 2009.

[55] D. Johnson and E. Carter, "Hydrogen in tungsten: Absorption, diffusion, vacancy trapping, and decohesion," *Journal of Materials Research*, vol. 25, no. 2, pp. 315–327, 2010.

[56] P. Franzen, C. Garcia-Rosales, H. Plank, and V. K. Alimov, "Hydrogen trapping in and release from tungsten: Modeling and comparison with graphite with regard to its use as fusion reactor material," *Journal of Nuclear Materials*, vol. 241-243, pp. 1082–1086, 1997.

[57] F. Sze, R. P. Doerner, and S. Luckhardt, "Investigation of plasma exposed W1% La2O3 tungsten in a high ion flux, low ion energy, low carbon impurity plasma environment for the international thermonuclear experimental reactor," *Journal of Nuclear Materials*, vol. 264, pp. 89–98, 1999.

[58] T. Venhaus, R. Causey, R. P. Doerner, and T. Abeln, "Behavior of tungsten exposed to high fluences of low energy hydrogen isotopes," *Journal of Nuclear Materials*, vol. 290-293, pp. 505–508, 2001.

[59] W. Shu, E. Wakai, and T. Yamanishi, "Blister bursting and deuterium bursting release from tungsten exposed tohigh fluences of high flux and low energy deuterium plasma," *Nuclear Fusion*, vol. 47, pp. 201–209, 2007.

[60] M. Y. Ye, H. Kanehara, S. Fukuta, N. Ohno, and S. Takamura, "Blister formation on tungsten surface under low energy and high flux hydrogen plasma irradiation in nagdis-1," *Journal of Nuclear Materials*, vol. 313-316, pp. 72–76, 2003.

[61] W. Shu, G. Luo, and T. Yamanishi, "Mechanisms of retention and blistering in near-surface region of tungsten exposed to high flux deuterium plasmas of tens of ev," *Journal of Nuclear Materials*, vol. 367-370, pp. 1463–1467, 2007.

[62] H. B. Zhou, Y. L. Liu, S. Jin, Y. Zhang, G. N. Luo, and G. H. Lu, "Towards supressing H blistering by investigating the physical origin of the H-He interaction in W," *Nuclear Fusion*, vol. 50, p. 115010, 2010.

[63] K. Heinola and T. Ahlgren, "Diffusion of hydrogen in bcc tungsten studied with first principle calculations," *Journal of Applied Physics*, vol. 107, p. 113531, 2010.

[64] L. Sun, S. Jin, X. C. Li, Y. Zhang, and G. H. Lu, "Hydrogen behaviors in molybdenum and tungsten and a generic vacancy trapping mechanism for h bubble formation," *Journal of Nuclear Materials*, vol. 434, pp. 395–401, 2013.

[65] K. Ohsawa, J. Goto, M. Yamakami, M. Yamahuchi, and M. Yagi, "Trapping of multiple hydrogen atoms in tungsten monovacancy from first principles," *Physical Review B*, vol. 82, p. 184117, 2010.

[66] G. H. Lu, H. B. Zhou, and C. S. Becquart, "A review of modeling and simulation of hydrogen behavior in tungsten at different scales," *Nuclear Fusion*, vol. 54, p. 086001, 2014.

[67] R. Causey and T. Venhaus, "The use of tungsten in fusion reactors: a review of the hydrogen retention and migration properties," *Physica Scripta*, vol. T94, pp. 9–15, 2000.

[68] H. Iwakiri, K. Morishita, and N. Yoshida, "Effects of helium bombardment on dueterium behavior in tungsten," *Journal of Nuclear Materials*, vol. 307-311, pp. 135–138, 2002.

[69] H. T. Lee, A. A. Haasz, J. W. Davis, R. G. Macaulay-Newcombe, D. G. Whyte, and G. M. Wright, "Hydrogen and helium trapping in tungsten under simultaneous irradiations," *Journal of Nuclear Materials*, vol. 363-365, pp. 898–903, 2007.

[70] M. Miyamoto, D. Nishijima, Y. Ueda, R. P. Doerner, H. Kurishita, M. J. Baldwin, S. Morito, K. Ono, and J. Hanna, "Observations of suppressed retention and blistering for tungsten exposed to deuterium-helium mixture plasmas," *Nuclear Fusion*, vol. 49, p. 065035, 2009.

[71] N. Juslin and B. D. Wirth, "Molecular dynamics simulation of the effect of subsurface helium bubbles on hydrogen retention in tungsten," *Journal of Nuclear Materials*, vol. 438, pp. S1221–S1223, 2013.

[72] P. Grigorev, D. Terentyev, G. Bonny, E. E. Zhurkin, G. van Oost, and J. M. Noterdaeme, "Mobility of hydrogen-helium clusters in tungsten studied by molecular dynamics," *Journal of Nuclear Materials*, vol. 474, pp. 143–149, 2016.

[73] L. Sandoval, D. Perez, B. P. Uberuaga, and A. F. Voter, "Competing kinetics and he bubble morphonogy in w," *Physical Review Letters*, vol. 114, p. 105502, 2015.

[74] F. Sefta, *Surface Response of Tungsten to Helium and Hydrogen Plasma Flux as a Function of Temperature and Incident Kinetic Energy*. PhD thesis, 2010.

[75] B. D. Wirth, K. D. Hammond, S. I. Krasheninnikov, and D. Maroudas, "Challenges and opportunities of modeling plasma-surface interactions in tungsten using high-performance computing," *Journal of Nuclear Materials*, vol. 463, pp. 30–38, 2015.

[76] K. Nordlund, "Class lecture notes," 2013. University of Helsinki, Department of Physics, Finland.

[77] S. Plimpton, "Fast parallel algorithms for short-range molecular algorithms," *Journal of Computational Physics*, vol. 117, pp. 1–19, 1995.

[78] J. Ziegler, J. Biersack, and M. Ziegler, *The Stopping and Range of Ions in Solids*. 2008.

[79] M. Finnis and J. Sinclair, "A simple empirical n-body potential for transition metals," *Philosophical Magazine A*, vol. 50, pp. 45–55, 1984.

[80] G. J. Ackland and R. Thetford, "An improved n-body semi-empirical model for body-centred cubic transition metals," *Philosophical Magazine A*, vol. 56, pp. 15–30, 1987.

[81] J. F. Ziegler, J. P. Biersack, and U. Littmark, *The Stopping and Range of Ions in Matter*. 1985.

[82] N. Juslin and B. D. Wirth, "Interatomic potentials for simulation of he bubble formation in w," *Journal of Nuclear Materials*, vol. 432, pp. 61–66, 2013.

[83] D. Beck, "A new interatomic potential function for helium," *Molecular Physics*, vol. 14, pp. 311–315, 1968.

[84] K. Morishita, R. Sugano, B. D. Wirth, and T. D. de la Rubia, "Thermal stability of helium-vacancy clusters in iron," *Nuclear Instruments and Methods in Physics Research Section B*, vol. 202, pp. 76–81, 2003.

[85] J. E. Lennard-Jones, "Determination of molecular fields ii. from the equation of state of a gas," *Proceedings of the Royal Society of London A*, vol. 106, pp. 463–477, 1924.

[86] D. K. Delashchenko, "The simulation of metallic hydrogen-helium solutions under the conditions of internal jupiter regions," *Russian Journal of Physical Chemistry*, vol. 80, pp. S31–S39, 2003.

[87] J. Tersoff, "New empirical approach for the structure and energy of covalent systems," *Physical Review B*, vol. 37, pp. 6991–7000, 1988.

[88] N. Juslin, P. Erhart, P. Traskelin, J. Nord, K. Henriksson, K. Nordlund, E. Salonen, and K. Albe, "Analytical interatomic potential for modeling nonequilibrium processes in the w-c-h system," *Journal of Applied Physics*, vol. 98, p. 123520, 2005.

[89] D. W. Brenner, "Empirical potential for hydrocarbons for use in simulating the chemical vapor deposition of diamond films," *Physical Review B*, vol. 42, p. 9458, 1990.

[90] X. C. Li, X. Shu, Y. N. Liu, F. Gao, and G. H. Lu, "Modified analytical interatomic potential for w-h system with defects," *Journal of Nuclear Materials*, vol. 408, pp. 12–17, 2011.

[91] M. A. Cusentino, K. Hammond, F. Sefta, N. Juslin, and B. D. Wirth, "A comparison of interatomic potentials for modeling tungstne-hydrogen-helium plasma-surface interactions," *Journal of Nuclear Materials*, vol. 463, pp. 347–350, 2015.

[92] J. Guterl, R. Smirnov, S. Krasheninnikov, B. Uberuaga, A. Voter, and D. Perez, "Modeling of hydrogen desorption from tungsten surface," *Journal of Nuclear Materials*, vol. 463, pp. 263–267, 2015.

[93] J. Li, "Atomeye: and efficient atomistic configuration viewer," *Modelling and Simulation in Materials Science and Engineering*, vol. 11, pp. 173–177, 2003.

[94] A. Sturkowski, "Visualization and analysis of atomistic simulation data with ovitothe open visualization tool," *Modelling and Simulation in Materials Science and Engineering*, vol. 18, p. 015012, 2010.

[95] L. Hu, K. D. Hammond, B. D. Wirth, and D. Maroudas, "Dynamics of small mobile helium clusters near a symmetric tilt grain boundary of plasma exposed tungsten," *Fusion Science and Technology*, vol. 71, pp. 336–51, 2017.

[96] K. Hammond, S. Blondel, L. Hu, D. Maroudas, and B. Wirth, "Large-scale atomistic simulations of low-energy helium implantation into tungsten single crystals," *Acta Materiala*, vol. 144, pp. 561–578, 2018.

[97] Z. J. Bergstrom, M. A. Cusentino, and B. D. Wirth, "A molecular dynamics study of subsurface hydrogen-helium bubbles in tungsten," *Fusion Science and Technology*, vol. 71, pp. 122–135, 2017.

[98] L. Wang, X. Shu, G. Lu, and F. Gao, "Embedded-atom method potential for modeling hydrogen and hydrogen-defect interaction in tungsten," *Journal of Physics: Condensed Matter*, vol. 29, p. 435401, 2017.

Vita

Mary Alice Cusentino is originally from Arlington Heights, Illinois. She graduated from Rolling Meadows High School in 2008 and went on to attend the University of Wisconsin-Madison. In 2013, she graduated with a Bachelors of Science in Nuclear Engineering and Mathematics as well as a Masters of Science in Nuclear Engineering and Engineering Physics. Mary Alice went on to join the Bredesen Center for Interdisciplinary Research and Graduate Education at the University of Tennessee. During in PhD studies, she worked on modeling plasma material interactions for fusion energy applications, focusing on using molecular dynamics simulations to investigate the behavior of tungsten under hydrogen and helium irradiation. She had the opportunity to attend multiple international conferences to present her work and published multiple peer-reviewed journal articles during her graduate career.